Modeling of Thermal Transport Properties in Metallic and Oxide Fuels

Weiming Chen

Dissertation submitted to the faculty of the Virginia Polytechnic Institute and State University in partial fulfillment of requirements for degree of

Doctor of Philosophy
In
Materials Science & Engineering

Xian-Ming Bai, Chair
William T. Reynolds
Sean G. Corcoran
Hongliang Xin

Aug 5th, 2021
Blacksburg, Virginia

Keywords: Thermal conductivity, oxide fuels, metallic fuels
Copyright 2021, Weiming Chen

Modeling of Thermal Transport Properties in Metallic and Oxide Fuels

Weiming Chen

(ABSTRACT)

Thermal conductivity is a critical fuel performance property not only for current UO_2 oxide fuel based light water reactors but also important for next-generation fast reactors that use U-Zr based metallic fuels. In this work, the thermal transport properties of both UO_2 based oxide fuels and U-Zr based metallic fuels have been studied.

At first, molecular dynamics (MD) simulations were conducted to study the effect of dispersed Xe fission gas atoms on the UO_2 thermal conductivity. Numerous studies have demonstrated that xenon (Xe) fission gas plays a major role on fuel thermal conductivity degradation. Even a very low Xe concentration can cause significant thermal conductivity reduction. In this work, the effect of dispersed Xe gas atoms on UO_2 thermal conductivity were studied using three different interatomic potentials. It is found that although these potentials result in significant discrepancies in the absolute thermal conductivity values, their normalized values are very similar at a wide range of temperatures and Xe concentrations. By integrating this unified effect into the experimentally measured thermal conductivities, a new analytical model is developed to predict the realistic thermal conductivities of UO_2 at different dispersed Xe concentrations and temperatures. Using this new model, the critical Xe concentration that offsets the grain boundary Kapitza resistance effect on the thermal conductivity in a high burnup structure is studied.

Next, the mechanisms on how Xe gas bubbles affect the UO_2 thermal conductivity have been studied using MD. At a fixed total porosity, the effective thermal conductivity of the bubble-containing UO_2 increases with Xe cluster size, then reaches a nearly saturated value at a cluster radius of 0.6 nm, demonstrating that dispersed Xe atoms result in a lower thermal conductivity than clustering them into bubbles. In comparison with empty voids of the same size, Xe-filled bubbles lead to a lower thermal conductivity when the number ratio of Xe atoms to uranium vacancies (Xe:V_U ratio) in bubbles is high. Detailed atomic-level analysis shows that the pressure-induced distortion of atoms at bubble surface causes additional phonon scattering and thus further reduces the thermal conductivity.

For metallic fuels, temperature gradient and irradiation induced constituent redistribution in U-Zr based fuels cause the variation in fuel composition and the formation of different phases that have different physical properties such as thermal conductivity. In this work, a semi-empirical model is developed to predict the thermal conductivities of U-Zr alloys for the complete composition range and a wide range of temperatures. The model considers the effects of (a) scattering by defects, (b) electron-phonon scattering, and (c) electron-electron scattering. The electronic thermal resistivity models for the two pure components are empirically determined by fitting to the experimental data. A new mixing rule is proposed to predict the average thermal conductivity in U-Zr alloys based on their nominal composition. The thermal conductivity predictions by the new model show good agreement with many available experimental data. In comparison with previous models, the new model has further improvement, in particular for high-U alloys that are relevant to reactor fuel compositions and at the low-temperature regime for the high-Zr alloys.

The average thermal conductivity model for the binary U-Zr fuel is also coupled with finite element-based mesoscale modeling technique to calculate the effective thermal conductivities of the U-Zr heterogeneous microstructures. For a U-10wt.%Zr (U-10Zr) fuel at temperatures below the γ phase transition temperature, the dominant microstructures are lamellar δ-UZr_2 and α-U. Using the mesoscale modeling, the phase boundary thermal resistance R (Kapitza resistance) between δ-UZr_2 and α-U has been determined at different temperatures, which shows a T^{-3} dependence in the temperature range between 300K and 800K. Besides, the Kapitza resistance exhibits a strong dependence on the aspect ratio of the δ-UZr_2 phase in the alloying system. An analytical model is therefore developed to correlate the temperature effect and the aspect ratio effect on the Kapitza resistance. Combining the mesoscale modeling with the newly developed Kapitza resistance model, the effective thermal conductivities of many arbitrary δ-UZr_2 + α-U heterogeneous systems can be estimated.

Modeling of Thermal Transport Properties in Metallic and Oxide Fuels

Weiming Chen

(GENERAL AUDIENCE ABSTRACT)

Thermal transport in nuclear fuels is critical for both energy conversion efficiency and nuclear energy safety. Therefore, understanding the thermal transport properties such as thermal conductivity of nuclear fuels is not only important for current UO_2 oxide fuel-based light water reactors but also critical for next-generation fast reactors that use U-Zr based metallic fuels. The thermal transport mechanisms in the two fuel types are fundamentally different: the predominant heat carriers in UO_2 are phonons while they are electrons in U-Zr. This work studies the thermal transport properties for both types of nuclear fuels.

At first, molecular dynamics (MD) simulations were conducted to study the effect of dispersed xenon (Xe) fission gas atoms on the UO_2 thermal conductivity, because Xe is the major fission gas product and even a small concentration of Xe can cause significant fuel thermal conductivity reduction. In this work, three different interatomic potentials were used to study the Xe effect. It is found that although these potentials result in significant discrepancies in the absolute thermal conductivity values, the normalized values are very similar at a wide range of temperatures and Xe concentrations. By integrating this unified effect into the experimentally measured thermal conductivities, a new analytical model is developed to predict the thermal conductivities of UO_2 at different Xe concentrations and temperatures. Then this new model is used to study how dispersed Xe influences the effective thermal conductivity of heterogeneous UO_2 microstructures with different grain sizes.

Next, we focused on how the presence of Xe bubbles degrades the effective UO_2 thermal conductivity using MD. The effects of both Xe gas bubble size and pressure were examined. Our results show that dispersed Xe gas atoms or small Xe clusters result in a lower thermal conductivity than clustering them into larger bubbles if the total porosity is fixed. In comparison with empty voids of the same sizes, a Xe-filled bubble leads to a lower thermal conductivity when the bubbles pressure is high, because the distorted bubble surface can cause additional phonon scattering effect.

Besides the UO_2 based oxide fuels, U-Zr based metallic fuels are promising fuel forms for next-generation fast reactors due to their high thermal conductivity. In this work, a semi-empirical model with a single set of parameters is developed to predict the average thermal conductivities of U-Zr alloys for the complete composition range and a wide range of temperatures. The thermal conductivities predicted by the new model have good agreement with many available experimental data, even if some experimental data are not included in the model fitting.

The above thermal conductivity model for the binary U-Zr alloy has been coupled with finite element-based mesoscale modeling to calculate the effective thermal conductivities of U-Zr heterogeneous microstructures containing α-U and δ-UZr_2 lamellar phases. Using the mesoscale modeling, the phase boundary thermal resistance R (Kapitza resistance) between δ-UZr_2 and α-U has been determined for a wide range of temperatures as well as the aspect ratio of the lamellar δ-UZr_2 phase. An analytical model is therefore developed to correlate the effects of temperature and aspect ratio on the Kapitza resistance. Combining the mesoscale modeling with the newly developed Kapitza resistance model, the effective thermal conductivities of many U-Zr heterogeneous systems can be accurately estimated.

Dedication

To my mom and dad, Fang Liu and Chao Chen

Acknowledgements

At first, I would like to thank my advisor Dr. Xian-Ming Bai. He has provided me with a lot of help throughout my PhD life. He gave me a lot of advice on the scope of my research projects. He patiently taught me knowledge. He also spent tremendous time to improve my scientific writing and critical thinking ability. All in all, he is a very kind person and has a rigorous attitude towards science, he is a good advisor with responsibilities.

Next, I would like to thank my committee members Dr. William T. Reynolds, Dr. Sean G. Corcoran, Dr. Hongliang Xin. They have offered me with a lot of helpful suggestions. I also appreciate all the help from the staff members and professors in the MSE department. Kim and Cindy gave me a lot of support outside the academic field, thank you!

Then, I would like to express my gratitude to all the colleagues that I worked with. Ziqi Xiao, Wenjiang Huang, Yaxuan Zhang, Jarin French, Axel Alcocer Seoane, Fengai Zhao and Jason Brown, they all gave me lots of help. And we have spent wonderful time working together.

I would like to thank my family for the love and support. Thank you, my mom Fang Liu and my dad Chao Chen. For my girlfriend Yijie Cui, thank you for your understanding and love. Thanks to all of my friends that enriched my life in Blacksburg.

Last but not least, thanks for all the resources that I used at Virginia Tech. The high-performance computing facilities at Virginia Tech, the Advanced Research Computing (ARC), are the main computing resources for my projects. I would also like to acknowledge the US Department of Energy (DOE) Nuclear Energy University Program (NEUP Award #DE-NE0008279 through the University of Florida and NEUP Award #DE-NE0008558 through Purdue University), for the financial support of my PhD research.

Attributions

Multiple colleagues and researchers have contributed to this work, their contributions are specified as follows:

For the work done in Chapter 3. I conducted all the simulations in this chapter and wrote the first draft of a journal manuscript as the lead author. Dr. Xian-Ming Bai guided the project direction, and we discussed the simulation details as well as the simulation results. Dr. Bai served as the corresponding author on this paper and contributed efforts on editing the manuscript.

The work described in Chapter 3 is reproduced in [W. Chen and X.M. Bai, "Unified effect of dispersed Xe on thermal conductivity of UO2 predicted by three interatomic potentials", JOM 72, 1710–1718 (2020).], with the permission of Springer, that I can include the article as part of my non-commercial dissertation.

For the work done in Chapter 4. I conducted most of the simulations in this chapter and wrote the first draft of a journal manuscript as the lead author. Dr. Xian-Ming Bai guided the project direction, and we discussed the simulation details as well as the simulation results. Dr. Bai served as the corresponding author on this paper and contributed efforts on editing the manuscript. Dr. M.W.D. Cooper and Dr. D.A. Andersson from the Los Alamos National Laboratory served as co-authors in this work, and they conducted simulations of special Xe cluster effect on UO_2 thermal conductivity, which is explained in Chapter 4.3.4. Dr. M.W.D. Cooper and Dr. D.A. Andersson also contributed efforts on editing the manuscript. Mr. Ziqi Xiao is currently a graduate student in the Department of Material Science and Engineering at Virginia Tech. He is also a co-author in this work, and he contributed to the work of code writing on creating different UO_2-Xe structures.

The work described in Chapter. 4 is reproduced in [W. Chen, M.W.D. Cooper, Z. Xiao, D.A. Andersson and X.M. Bai, "Effect of Xe bubble size and pressure on the thermal conductivity of UO2—Amolecular dynamics study", Journal of Materials Research 34(13): 2295-2305 (2019).], with the permission of Springer, that I can include the article as part of my non-commercial dissertation.

For Chapter 5: I conducted all the simulations in this chapter and wrote the first draft of a journal manuscript as the lead author. Dr. Xian-Ming Bai guided the project direction, and we discussed the simulation details as well as the simulation results. Dr. Bai served as corresponding author on this paper and contributed efforts on editing the manuscript.

The work described in Chapter 5 is reproduced in [W. Chen and X.M. Bai, "Temperature and Composition Dependent Thermal Conductivity Model for U-Zr Alloys", Journal of Nuclear Materials 507, 360-370 (2018).], with the permission of Elsevier, that I can include the article as part of my non-commercial dissertation.

For Chapter 6: I conducted all the simulations in this chapter and wrote the first draft for a potential journal manuscript as the lead author. The manuscript will be sent to a peer-review journal. Dr. Xian-Ming Bai guided the project direction, and we discussed the simulation details as well as the simulation results. Dr. Bai served as corresponding author on this paper and contributed efforts on editing the manuscript.

Table of Contents

List of figures

List of tables

Chapter 1: Overview

Since the first nuclear reactor was built around 1950's in USA, the nuclear energy has become a reliable source of electrical energy, which makes up of world's 13% electrical energy consumption [1]. Due to the limited availability of resources like oil, natural gas and coal, there has been a growing demand for this alternative clean and economic energy source. The current commercial reactors are predominately light water reactors (LWRs), which are thermal reactors and use UO_2 or UO_2 based mixed oxides as the fuels. Recently, the next-generation fast reactors such as sodium-cooled faster reactors have received significant interest, which are proposed to use U-Zr or U-Pu-Zr based metallic fuels. In nuclear reactors, the fuel safety and thermal energy conversion efficiency are of major concerns, in which the fuel thermal conductivity plays a vital role [2-4]. In reactors, radiation causes complex microstructural evolution in nuclear fuels, which degrades the fuel thermal conductivity significantly. Therefore, understanding how radiation-induced small defects (e.g., point defects and their clusters) and large microstructural features affect the fuel thermal conductivity is critical for the safe use of both metallic fuels and oxide fuels.

1.1 Oxide fuels

Nowadays the widely deployed reactors are generation-II type reactors, which are light water reactors (LWRs). The generation-III light water reactors are the emerging reactor type during the recent two decades. The LWRs are primarily fueled with UO_2 or $(U, Pu)O_2$. And there are growing interests on alternative fuel types such as U-Si fuels for future LWRs [5, 6], since U-Si fuels showed certain advantages over UO_2 fuels. However, the significant swelling of U-Si fuels in reactor conditions could be problematic. To date, UO_2 based oxide fuels are still the dominant fuel types in LWRs. In this report, the current knowledge and our work of UO_2 fuels will be explained. There are several advantages of UO_2 fuels. Frist of all, oxide fuels have been highly commercialized over the decades. Secondly, UO_2 has a very high melting point, which enables a wide range of operating temperatures. Last but not least, UO_2 fuels are very stable since there is no phase change at high temperatures and there is only minor thermal expansion and swelling when subjected to high temperatures and irradiation.

There are also a few disadvantages of UO_2 fuels. As mentioned previously, its thermal conductivity is a critical metric for fuel performance. However, one of the biggest problems is that even in its pristine form, UO_2 has a very low thermal conductivity [7]. Due to the low thermal conductivity, a large thermal gradient along the radial direction of the fuel rod can build, leading to fuel restructuring with different grain structure [8]. Besides, under reactor environment, the evolution of radiation/fission-induced defects and fission products leads to complex microstructural evolution. The resulted microstructures include grain boundaries (GBs), gas bubbles, metallic and ceramic precipitates, dislocation loops, etc. [9-12]. In turn the fuel thermal conductivity decreases significantly with increasing burnup [3]. In addition to these large microstructures, the fuel matrix also contains some small atomic-level defects such as interstitials and vacancies, dispersed fission products, as well as their small clusters. Some of them can cause significant phonon scattering effects to the fuel thermal conductivity [13], which affect the overall fuel performance. Therefore, development of physics-based models that can predict the thermal conductivity degradation by both large microstructures and small defects is critical for accurately predicting the thermal transport behavior of UO_2 fuels in reactor conditions.

1.2 Metallic fuels

Fast reactors are another type of fission reactor. Although currently there are no commercial fast reactors available, some experimental fast reactors had been employed in the last few decades, including the Experimental Breeder reactor (EBR-II), Fast Flux Test Facility (FFTF) reactor and Fermi I reactor. The fast reactors are well-recognized as the next-generation (Gen-IV) reactors, and some of them use uranium-zirconium (U-Zr) based metallic fuels. In U-Zr based metallic fuels, the Zr composition is typically at 10 wt.% (denoted as U-10Zr. Note all compositions for U-Zr alloys in this report are based on weight percent unless specified differently). Previously, U-10Zr and U-19Pu-10Zr fuels have been irradiated in the Fast Flux Test Facility (FFTF) reactor [14] and the Experimental Breeder Reactor II (EBR-II) [15].

There has been increasing interest on the metallic fuels since they show certain benefits over the oxide fuels [16, 17]. In comparison with oxide fuels such as UO_2 and $(U,Pu)O_2$, U-Zr based metallic fuels have higher fissile density and breeding ratio, which will allow for longer operation before refueling. Besides, metallic fuels have good thermal conductivity to ensure energy harvesting. Moreover, these fast reactor fuels have the potential to transmute long-lived minor actinides such as americium (Am) in light-water reactor (LWR) spent fuels, which would help reduce the volume of radioactive wastes in geological repositories [16].

However, metallic fuels are susceptible to fission gases (e.g., xenon, krypton) induced fuel swelling [18]. The fuel swelling can induce a physical contact between a fuel rod (also called fuel slug) and its cladding that is typically made of stainless steels. The contact can result in fuel-cladding mechanical and chemical interactions (FCMI/FCCI). For instance, a recent study shows the FCCI phenomenon between U-10Zr fuel and HT-9 cladding (a ferritic/martensitic steel developed for fast reactor applications) [14], as is shown in Fig. 1.1. The FCCI could lead to cladding failure [16, 19]. The fuel swelling is closely related to the fuel temperature and thus the fuel thermal conductivity. Therefore, understanding the thermal transport behavior in metallic fuels is important for predicting the fuel performance in fast reactors.

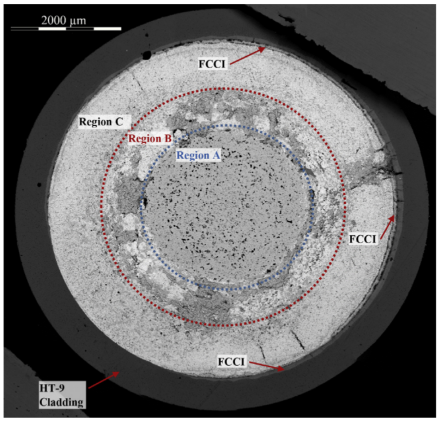

Fig. 1. 1. Back-scattered electrons (BSE) image of U-10Zr alloy with the HT-9 cladding, which clearly shows the FCCI phenomenon at the rim region (region C) [14].

Chapter 2: Background knowledge

This chapter mainly describes certain background knowledge of UO_2 and U-Zr fuels. In this chapter, we will discuss a very unique microstructure in UO_2 fuels, i.e. the high burnup structure (HBS). For metallic fuels, the constituent redistribution in U-Zr fuels will be explained in this chapter. During such a redistribution process, the composition varies along the radial direction of the fuel rod (or called "slug"). In this case, we will discuss the U-Zr phase diagram in this chapter.

2.1. HBS

For irradiated UO_2 fuels, there are various microstructure features, including gas bubbles, grain boundaries, metallic and ceramic precipitates. In general those microstructure features will reduce the fuel thermal conductivity. However, one interesting microstructural feature in reactor irradiated UO_2 fuels is the HBS. HBS typically forms at the rim region of a fuel pellet where the temperature is much lower than that at the fuel pellet center [9, 20]. During HBS formation, the average grain size decreases from about 10 μm in the original unrestructured fuel to about a few hundred nanometers in HBS through a grain subdivision process [9]. Interestingly, it has been experimentally observed that the formation of HBS can improve the fuel thermal conductivity in comparison with the unrestructured fuel at the same burnup [3, 9, 21], which is counterintuitive because the increased GB density in HBS should cause more thermal conductivity reduction. Researchers [21, 22] have argued that the high density of GBs in HBS can effectively remove point defects from the grain interior and thus reducing the phonon scattering effect. The overall effect is that the thermal conductivity in the HBS region can be improved after the transformation.

2.2. Constituent redistribution in U-Zr alloys

During a reactor operation, the fuel temperature is higher at the cylindrical fuel rod center than at the rim region. Therefore, a thermal gradient can build up along the radial direction of a fuel rod. The combined effects of the thermal gradient and radiation can drive the fuel constituents to migrate along the fuel radial direction. It has been found in experiments that in both U-10Zr and U-19Pu-10Zr fuels, Zr migrates to the hotter fuel center while U migrates in the opposite direction [14, 15]. Pu, if presents in the fuel, does not migrate significantly [15]. As a result, Zr becomes enriched at the fuel rod center and its molar fraction can exceed 50% in an irradiated U-10Zr fuel [14]; On the other hand, U becomes enriched at the intermediate region in the radial direction. This phenomenon is called fuel constituent redistribution, as shown in Fig. 2.1. Hofman et al. [23], Kim et al. [15, 24] and Galloway et al. [25] have developed mechanistic models for modeling the constituent redistribution in U-Zr and U-Pu-Zr based fuels, which are based on the thermodynamic and diffusion properties of the metallic fuels. Due to the fuel constituent redistribution, the local fuel compositions can be very different from the nominal composition (e.g., U-10Zr). As a result, the thermal conductivities of those regions with composition variations also change. Therefore, a temperature- and composition-dependent thermal conductivity model is needed to accurately predict the fuel thermal transport properties in the irradiated fuels.

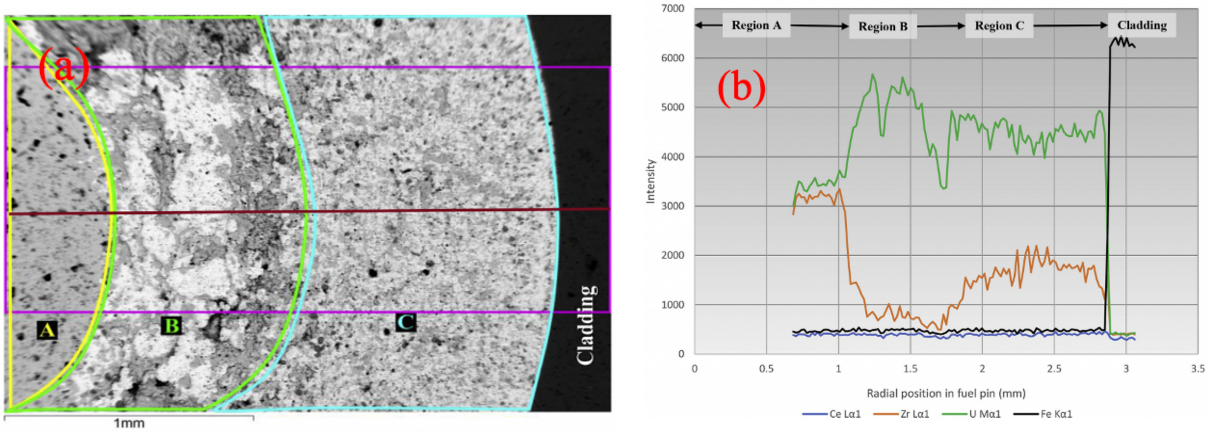

Fig. 2. 1. Constituent redistribution in a U-10Zr fuel from experimental measured [14] (a) Back-scattered electron (BSE) image of the U-Zr fuel along radial direction and (b) X-ray peaks from energy dispersive X-ray spectroscopy (EDS). Zr moves towards region A, which is the cold region and U becomes enriched at intermediate region (region B).

2.3. U-Zr phase diagram

The phase diagram of a U-Zr system [26] in Fig. 2.2 shows that variation of temperature and alloy composition can lead to the formation of many intermetallic phases. Therefore, the combination of the thermal gradient and constituent redistribution could cause phase transformations along the fuel rod radial direction [14, 16]. In the early 1950s [27], it had been experimentally determined that pure uranium exists three crystalline phases at different temperatures: orthorhombic α phase, tetragonal β phase, and body-centered-cubic (BCC) γ phase. According to the U-Zr phase diagram [26], α phase is the stable phase at temperatures below 668 °C; β phase is stable between 668 °C and 776 °C; γ phase is stable above 776 °C until it melts at about 1133 °C. Both α and β phases have limited Zr solubilities while the γ phase has a complete solubility with the BCC β-Zr. In a U-10Zr alloy, the fuel composition before irradiation is nearly homogenous with a lamellar structure of α-U and δ-UZr_2 at the room temperature. Here δ phase has a hexagonal crystal structure, and its composition is close to Uzr_2 (or U-43wt.%Zr). This phase is stable below about 610 °C. Upon the constituent redistribution in reactors, the fuel consists of a BCC γ phase of U-Zr solid solution in the center hot region; In the intermediate region in the radial direction, the fuel has a (γ+β) two-phase coexistence; In the cold rim region, the fuel has a (δ+α) two-phase coexistence. Therefore, α, β, δ, and γ phases all present in the irradiated U-Zr fuels.

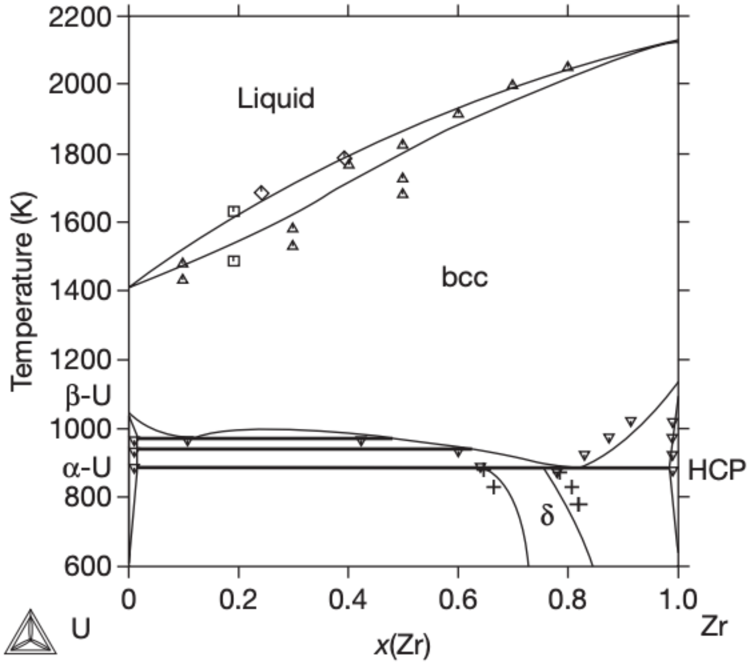

Fig. 2. 2. U-Zr phase diagram [26].

Chapter 3: Dispersed Xe effect on UO_2 thermal conductivity by Molecular Dynamics Simulations

The work presented in this chapter is reproduced from [W. Chen and X.M. Bai, "Unified effect of dispersed Xe on thermal conductivity of UO2 predicted by three interatomic potentials", JOM 72, 1710–1718 (2020).], with the permission of Springer Publishing.

3.1 Motivation and current study

In addition to the large microstructure features mentioned in Chapter 2, there are extensive small defects present in a UO_2 fuel after irradiation. The typical small defects in a UO_2 fuel include nonstoichiometric $UO_{2\pm x}$ [28, 29], interstitials and vacancies as well as their clusters [30], and dispersed fission products (Zr, La, Xe, Kr, etc.) [13]. Unlike interstitials and vacancies that can be annihilated through defect recombination or loss to sinks and thus their concentrations can be low at the steady state [31], fission products cannot be annihilated or recombined so that they typically remain in the fuel (except for fission gas release). Therefore, it is important to understand how the non-vanishing dispersed fission products affect the thermal conductivity of UO_2.

MD simulations are widely used to calculate the thermal conductivity of UO_2 [13, 32-36]. The studied systems include pure UO_2 [36], and defective UO_2 containing various types of dispersed fission products and point defects [13], dislocations [34], GBs [35], helium bubbles [33]. For dispersed fission products and point defects, Liu et al. have shown that dispersed Xe atoms caused a stronger phonon scattering effect than other fission products (e.g., Zr, La and Pu) and nonstoichiometric $UO_{2\pm x}$ defects [13]. Note that Xe is a major gaseous fission product in the fuel. It can either aggregate to form intergranular and intragranular bubbles [37], or be trapped by small defects to form dispersed fission gas atoms in the UO_2 matrix [38-40]. Therefore, it is of great interest to understand the effect of dispersed Xe on UO_2 thermal conductivity. Recently Tonks et al. [32] have conducted MD simulations using the Busker potential to study the effect of dispersed Xe on the thermal conductivity of UO_2. Based on their MD results, a Xe scattering term was added into the Fink's semi-empirical model [7] to predict the UO_2 thermal conductivity at different dispersed Xe concentrations and temperatures. Note that the Fink's model is a commonly accepted thermal conductivity model for unirradiated UO_2 [7], which was fitted to a wide range of experimental data. Tonks's Fink+Xe model has been implemented [22] in the mesoscale fuel performance software – MARMOT [41]. The model has been successfully used to predict the effective thermal conductivities of heterogeneous microstructures that contain dispersed Xe atoms, Xe gas bubbles, and GBs [22, 32].

Despite of the success of Tonks's model, it was developed based on one single interatomic potential. It is well known that the accuracy of thermal conductivity predicted by MD strongly depends on the quality of the potential. For single crystal UO_2, Chernatynskiy et al. have surveyed nearly 30 potentials and found that different potentials predict very different thermal conductivities [36]. Liu et al. [13] have used two potentials to calculate the phonon scattering parameters for different types of defects in UO_2. Although similar scattering terms were found for some fission products and defects (e.g., Zr, Pu, U^{5+}, uranium vacancy (V_U)) between two potentials, large discrepancies exist for some others such as La and oxygen interstitial (I_O) [13]. For dispersed Xe, only the results of one potential (Busker) were shown. Therefore, it is unclear whether large discrepancies exist between different potentials for dispersed Xe.

3.2 Methods

In this chapter, the non-equilibrium molecular dynamics (NEMD) method was used to calculate the thermal conductivities of UO_2 containing different concentrations of dispersed Xe atoms at different temperatures, using the LAMMPS package [42]. The primary simulation system consisted of $6 \times 6 \times 50$ fluorite UO_2 unit cells with periodic boundary conditions (PBCs) employed in all directions. In addition, a larger $10 \times 10 \times 50$ supercell was used for spot check to test the system size effect. Unless specified differently, all reported results are from the smaller (primary) system. The longest dimension of each supercell (in the z direction) was applied with thermal gradients for thermal conductivity calculation (Fig. 3.1). Xenon atoms were randomly introduced into the supercells as substitutional defects to replace uranium atoms but keeping the number of Xe atoms the same on each side of the heat sink. To maintain the charge neutrality of the entire system, two neighboring oxygen atoms of each inserted Xe atom were removed. In other words, each Xe atom replaced a UO_2 pair. The Xe concentration is defined as the ratio between the number of inserted Xe atoms to the total number of U sites in the original perfect supercell. The Xe concentration ranges from 0.33% to 2% in the primary simulation system. The temperature ranges from 300 K to 1500 K with an interval of 300 K.

Three interatomic potentials were tested: Busker [43], Basak [44] and Cooper-Rushton-Grimes [45, 46] (referred as CRG potential). All potentials consist of at least a Buckingham term and a Coulombic term. The Basak potential contains an additional Morse term. The CRG potential includes an embedded atom method (EAM) term in addition to the other three pairwise terms to capture the many-body effects. For U-Xe, O-Xe, and Xe-Xe interactions, Buckingham, Morse, Lennard-Jones or combination of them are used. The Xe related potential parameters can be found in Ref. [47] for Busker potential, Ref. [48] for Basak potential, Refs. [46, 49] for CRG potential. The interatomic potentials are well described in the next context.

In most of the simulations, the thermal conductivities were calculated at 300 K. To study the temperature effects, temperatures up to 1,500 K were also used. The time step was 2 femtoseconds (fs) in all simulations. Initially, the system was equilibrated in a NPT ensemble (constant number of atoms, pressure, and temperature) at 300 K and zero external pressure for 40 picoseconds (ps). Next the simulation was conducted in a NVE ensemble (constant number of atoms, volume, and energy) with heat input at the ends and heat removal at the middle of the simulation system along the z direction, as shown in Fig. 3.1. The employment of periodic boundary conditions meant that two nearly identical thermal gradients were established in the system. After the system reached the steady state, the temperature profiles were averaged over about 1.6 nanoseconds (ns). The thermal conductivity k was calculated based on the Fourier's law:

$$J = -k\frac{dT}{dz}, \tag{3.1}$$

where J is the heat flux imposed in the system and dT/dz is the resulting temperature gradient. Here the heat flux for establishing one thermal gradient was 37.2 GW/m^2. To calculate the temperature gradient, a linear fitting of the temperature profile within an appropriate fitting range was conducted for each gradient, as shown in Fig. 3.1. The dT/dz in Eq. (3.1) was the average of the slopes of the two thermal gradients. Therefore, each reported thermal conductivity from the primary simulation system was based on the average of eight values (four runs, two temperature gradients each). In the larger system, one simulation was conducted at each condition to save to computational cost.

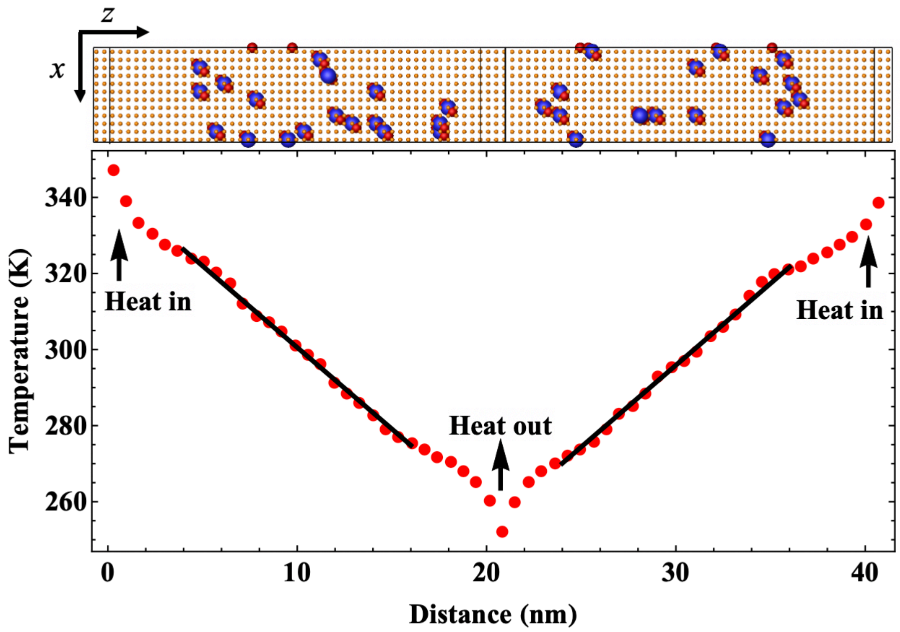

Fig. 3. 1. Snapshot of randomly distributed 0.5 at.% Xe atoms and the NEMD method ("direct method") for calculating the thermal conductivity in a UO_2 system containing dispersed Xe. The small orange spheres represent uranium atoms, the large blue spheres represent Xe substitutional atoms, red medium spheres represent oxygen vacancies (removed oxygen atoms) near the inserted Xe atoms. Oxygen lattice atoms are not shown for clarity purpose.

3.3 Results

3.3.1. Thermal conductivity of pure UO_2

First, the thermal conductivities of pure single crystal UO_2 were calculated using the three potentials from 300 K to 1500 K, as shown in Fig. 3.2. These values were used as references for our later study of the dispersed Xe effect. It can be clearly seen that different potentials predict very different thermal conductivities. At a given temperature, Busker potential results in the highest value while the CRG potential gives the lowest. As expected, all potentials predict that the thermal conductivity decreases with temperature – a typical phonon-dominant thermal transport behavior. Previously researchers [13, 36] have used various potentials to calculate the thermal conductivities of single crystal UO_2. The thermal conductivity at 300 K reported by Chernatynskiy et al. [36] is 17.34 $W \cdot m^{-1} \cdot K^{-1}$ for Basak potential and 19.16 $W \cdot m^{-1} \cdot K^{-1}$ for Busker potential, respectively. These values are in good agreement with our results of 16.10 $W \cdot m^{-1} \cdot K^{-1}$ for Basak potential and 18.99 $W \cdot m^{-1} \cdot K^{-1}$ for Busker potential. Note that Chernatynskiy et al. [36] calculated the bulk thermal conductivity through solving Boltzmann Transport Equations (BTE). Unlike MD having finite size effect [50, 51], BTE results are not sensitive to the simulation system size [36, 52]. Therefore, the values reported in Ref. [36] can be used as references to check the accuracy of our MD results. The thermal conductivity predicted by the GRG potential is 12.05 $W \cdot m^{-1} \cdot K^{-1}$ at 300 K in this chapter, which is much smaller than the value of 17.09 $W \cdot m^{-1} \cdot K^{-1}$ calculated by Liu et al. [13]. However, our value agrees well with 13.5 $W \cdot m^{-1} \cdot K^{-1}$ at 300 K reported by Maxwell et al. [53] using the same CRG potential. The discrepancies may be due to different simulation methodologies used in these studies. In this chapter all simulations have the same simulation setup. In addition, only the normalized thermal conductivities are used for describing the effect of dispersed Xe. Therefore, the effects of system size and simulation setup are expected to cancel out in this work.

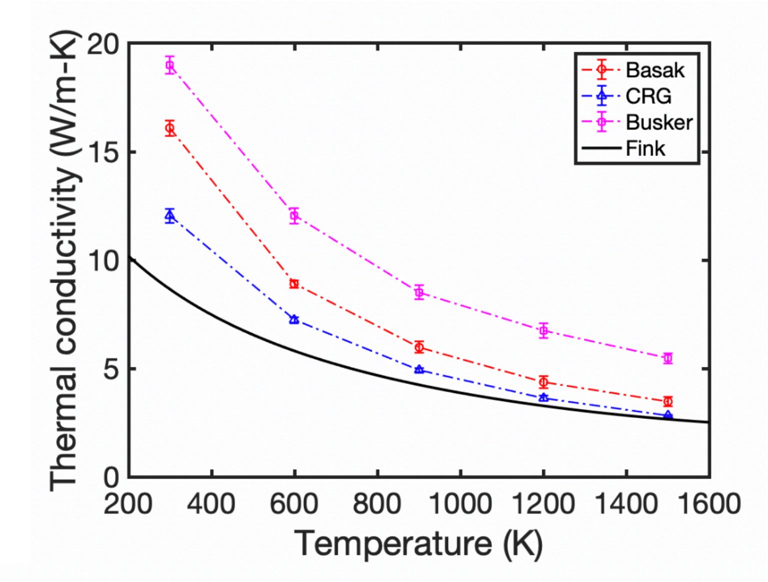

Fig. 3. 2. Absolute thermal conductivities of single crystal UO_2 predicted by the three potentials and Fink's model for fully dense UO_2 at different temperatures. Error bars represent standard deviation and some of them are smaller than the symbol size.

3.3.2. UO_2+Xe thermal conductivity model

Based on many experimental thermal conductivity data of unirradiated UO_2, Fink [7] developed a semi-empirical thermal conductivity model as a function of temperature (T) for 95% of theoretical density,

$$k(T) = \frac{1}{A+BT+CT^2} + \frac{6400}{\left(\frac{T}{1000}\right)^{5/2}} \exp\left(-\frac{16350}{T}\right), \tag{3.2}$$

where the first and second terms on the right-hand side represent phonon-mediated lattice thermal conductivity and small polaron contribution, respectively; T is absolute temperature in Kevin. The A, B, C values are listed in Table 3.1. Equation (3.2) can be scaled to 100% of theoretical density by using the same equation as in Fink's work [7], which was recommended by Brandt and Neuer [54],

$$\frac{k_p}{k_s} = 1 - (2.6 - 0.5\frac{T}{1000})p \ , \tag{3.3}$$

where k_s is the thermal conductivity of fully dense UO_2, k_p is the thermal conductivity for none-fully-dense UO_2 with a porosity of p. For Fink's model (Eq. (3.2)), $p = 0.05$ is used. The Fink's model for fully dense UO_2 is plotted as the solid line in Fig. 3.2. Clearly, the three potentials overpredict the thermal conductivity.

Next the thermal conductivities of UO_2 containing dispersed Xe were calculated using three potentials. The Xe concentration was 0.33%, 0.67%, 1% and 2%, respectively. Same as for pure UO_2, the temperature range was from 300 K to 1500 K. Since different potentials predict very different absolute thermal conductivities (Fig. 3.2), the normalized values are used to characterize the effect of dispersed Xe on the thermal conductivity reduction. The normalized thermal conductivity is defined as,

$$\eta = \frac{k_{Xe+UO_2}(T)}{k_{pure\,UO_2}(T)}, \tag{3.4}$$

where $k_{pure\,UO_2}(T)$ and $k_{Xe+UO_2}(T)$ are the thermal conductivities of a pure UO_2 and a UO_2 system containing dispersed Xe at temperature T predicted by the same potential, respectively. Figure 3.3(a) shows the normalized thermal conductivities at different Xe concentrations and temperatures predicted by three potentials. At a given temperature, the normalized thermal conductivity decreases with the increasing Xe concentration, which is expected because more Xe atoms cause stronger phonon scattering effect and thus more thermal conductivity reduction. At a given Xe concentration, the normalized thermal conductivity increases with temperature. This is because the anharmonic phonon scattering dominates at high temperatures so that the Xe-induced phonon scattering becomes relatively weaker. The most interesting trend observed in Fig. 3.3(a) is that all three potentials predict very similar normalized thermal conductivities at any given temperature and Xe concentration studied in this work. To check whether the trend is sensitive to the system size, the normalized thermal conductivities were also calculated using a larger system (with $10 \times 10 \times 50$ unit cells) containing 1% Xe at 300 K and 1000 K. The Xe distribution was also different for each potential. The results are shown with smaller symbols enclosed in the two circles in Fig. 3.3(a). The agreement among three potentials is even better than in the smaller system. In addition, the results from the larger system align very well with the trend obtained from the smaller system. The results from the two-sized systems clearly indicate that three potentials predict consistent phonon scattering effect by dispersed Xe, even though they predict very different absolute thermal conductivities. This unified effect provides a scientific basis for the later development of a new analytical model to quantify the effect of dispersed Xe on the thermal conductivity reduction in UO_2.

To describe the effect of dispersed Xe on UO_2 thermal conductivity, Tonks et al. [32] added a Xe scattering term into Fink's model (Eq. (3.2)),

$$k(T) = \frac{1}{A+BT+CT^2+\alpha_{Xe}C_{Xe}^{d}} + \frac{6400}{\left(\frac{T}{1000}\right)^{5/2}} \exp\left(-\frac{16350}{T}\right), \tag{3.5}$$

where α_{Xe} is the scattering parameter for dispersed Xe, C_{Xe} is Xe concentration, d is an exponent, and other parameters have the same meaning as in Eq. (3.2). They conducted MD simulations using the Busker potential to calculate the thermal conductivity of UO_2 containing dispersed Xe. Then they corrected the MD results to account for the phonon-spin mechanism. Based on their

MD results, α_{Xe}, C_{Xe}, and d were determined. Using a similar approach, recently Liu et al. [13] have determined the scattering parameters of various fission products and point defects.

Table 3. 1. The fitting parameters in Eq. (3.5) for different potentials as well as for the averaged MD + Fink model.

	A $(\mathrm{m\cdot K\cdot W^{-1}})$	B $(\mathrm{m\cdot W^{-1}})$	C $(\mathrm{m\cdot K^{-1}\cdot W^{-1}})$	α_{Xe} $(\mathrm{m\cdot K\cdot W^{-1}})$	d
Fink	7.5408×10^{-2}	17.692×10^{-5}	3.6142×10^{-8}	-	-
Basak	1.671×10^{-2}	14.285×10^{-5}	2.804×10^{-8}	10.256	0.984
EAM	3.534×10^{-2}	14.448×10^{-5}	4.572×10^{-8}	9.216	0.915
Busker	2.315×10^{-2}	9.571×10^{-5}	0.7036×10^{-8}	5.825	0.888
Average MD + Fink	7.5408×10^{-2}	17.692×10^{-5}	3.6142×10^{-8}	13.422	0.902

Since our MD results show that three different potentials predict similar dispersed Xe effect, we intend to integrate our MD results into Eq. (3.5), using a different approach from Ref. [32]. Here two steps are used. First, for pure UO2 ($C_{Xe} = 0$), the MD results are fitted to the first term of Eq. (3.5) so that parameters of A, B and C are obtained for each potential. Next α_{Xe} and d are obtained by fitting to the MD results at different Xe concentrations, using A, B and C values obtained from the previous step. These parameters are given in Table 3.1 for each potential. Since different potentials result in different absolute thermal conductivities, the A, B and C values are very different. However, the Xe related terms (α_{Xe} and d) predicted by the three potentials are similar, suggesting that the three potentials predict similar Xe effect, although not identical.

Based on our MD results from three potentials, we use a new approach to re-parameterize Eq. (3.5). At each Xe concentration, the average values of the normalized thermal conductivities as a function of temperature are fitted to a second-order polynomial function,

$$\eta_i = a_i + b_i T + c_i T^2, \tag{3.6}$$

where *i* represents a Xe concentration, a_i, b_i, c_i are fitting parameters. The lines in Fig. 3.3(a) are the fitted results. The fitting parameters are given in Table 3.2.

Table 3. 2. The fitting parameters in Eq. (3.6) for different Xe concentrations.

Xe concentration	a_i	b_i (K^{-1})	c_i (K^{-2})
0.33%	-1.039×10^{-7}	4.068×10^{-4}	0.498
0.67%	-1.167×10^{-7}	4.788×10^{-4}	0.334
1%	-0.963×10^{-7}	4.633×10^{-4}	0.247
2%	-0.602×10^{-7}	3.938×10^{-4}	0.105

Since different potentials predict similar reduction fractions in thermal conductivity (or normalized thermal conductivities) at a given Xe concentration and temperature, it is assumed that the experimental thermal conductivity (Fink's model) can be reduced by the same fraction as in MD. Therefore, Eq. (3.6) is combined with the fully dense Fink's model (the first term of Eq. (3.2) and Eq. (3.3)),

$$k_{ave,i} = \eta_i \times k_{Fink-100\%}(T). \qquad (3.7)$$

Using Eq. (3.7), the realistic thermal conductivities at different Xe concentrations and temperatures are estimated, which are shown as symbols in Fig. 3.3(b). To obtain a new analytical equation, the first term of Eq. (3.5) (after converted for fully dense UO$_2$) is fitted to these data to get new α_{Xe} and d (the last row in Table 3.1). The A, B, C parameters are kept the same as in the Fink's model. The thermal conductivities predicted by the new analytical model are plotted as lines in Fig. 3.3(b). Our fitting gives $\alpha_{Xe,ave}$ = 13.422 m $\cdot$ K $\cdot$ W^{-1} and d_{ave} =0.902, which are different from those in Tonks's model (α_{Xe} = 1.5 m $\cdot$ K $\cdot$ W^{-1} and d = 0.45) [32]. The discrepancy could be caused by different simulation setups between two studies. In addition, we did not use the phonon-spin correction as in Tonks's work.

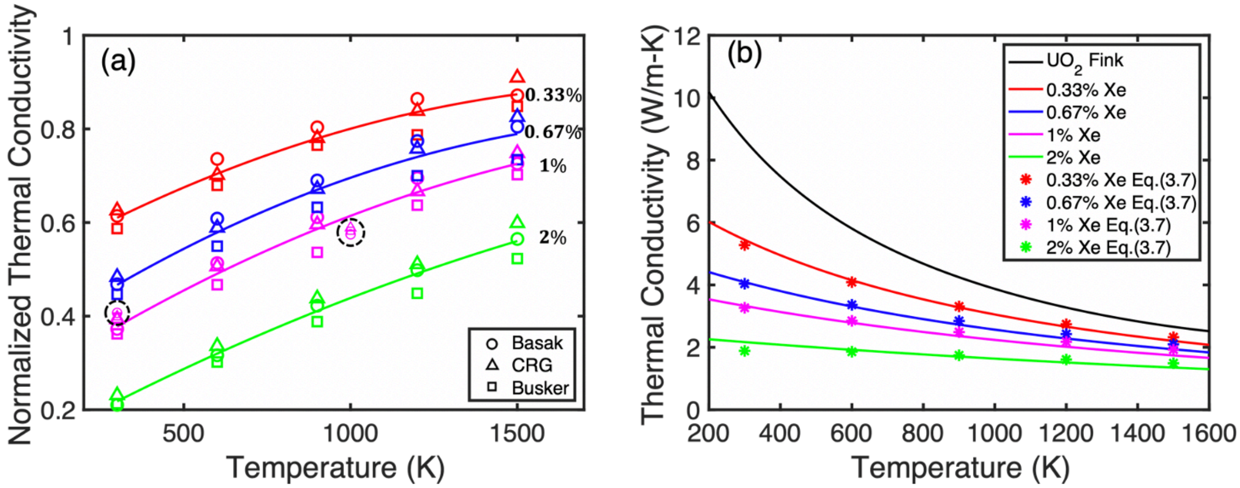

Fig. 3. 3. (a) Normalized thermal conductivities predicted by three potentials at different Xe concentrations and temperatures. The symbols in (a) represent MD results and the lines are the fitting curves of the average of MD data (Eq. (3.6)). The results from a larger simulation system are shown with smaller symbols enclosed in the two dashed circles. (b) New thermal conductivity model based on the average of three potentials and Fink's model. The symbols are calculated from Eq. (3.7). The lines are plotted based on Eq. (3.5). All thermal conductivities are converted for fully dense UO_2.

Figure 3.4 illustrates the difference between two models. Note in this figure both terms in Eq. (3.5) are included and both models are converted to fully dense UO_2. When the Xe concentration is low (0.1% and 0.5%), our model gives a higher thermal conductivity than Tonks's model over the entire temperature range. In particular, when the Xe concentration is very low (0.1%), the thermal conductivity reduction in Tonks's model is significantly larger than our model. For example, our model predicts that the thermal conductivity decreases by 17.7% from Fink's model at 300 K while Tonks's model predicts the reduction is 33.7%. On the other hand, our model gives a lower thermal conductivity when the Xe concentration is greater than 1%. Therefore, the two models predict qualitatively similar but quantitatively different thermal conductivities. However, since different approaches were used in the two studies and there are no experimental data to validate them, our model can be considered as an alternative model for describing dispersed Xe effect on the thermal conductivity of UO_2.

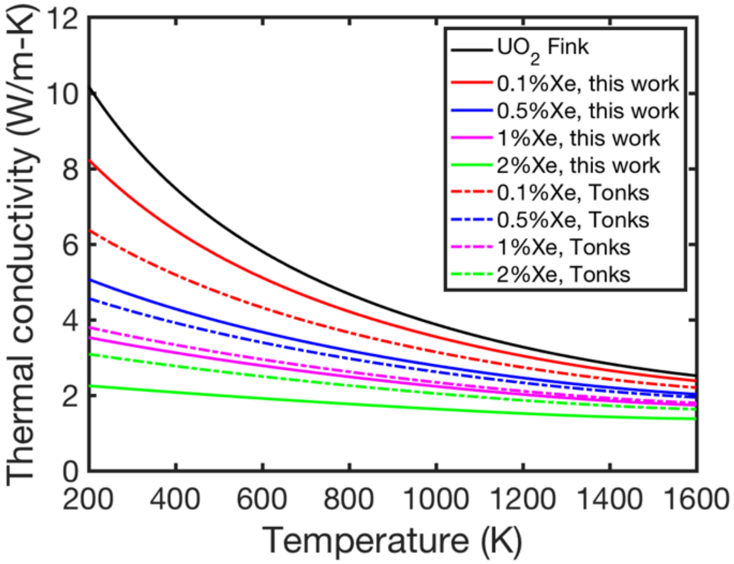

Fig. 3. 4. Comparison of thermal conductivities predicted by our new model (Eq. (3.5)) and Tonks's model. All thermal conductivities are converted for fully dense UO_2.

3.3.3. Effective thermal conductivity of UO$_2$ (HBS VS unrestructured fuel)

Using the new model, the thermal conductivity of a UO$_2$ fuel matrix can be estimated as long as the Xe concentration and temperature are known. If the fuel contains some other microstructural features such as GBs and fission gas bubbles, the effective thermal conductivity of such a composite system also can be estimated. For example, Bai et al. [22] conducted mesoscale simulations in MARMOT to calculate the effective thermal conductivities of different microstructures. Based on the mesoscale simulation results, an analytical "multiplier" model has been developed to predict the effective thermal conductivity of a composite system containing dispersed Xe, GBs, and Xe gas bubbles,

$$k_{Xe+GB+bubble}^{eff} = k_{Xe} \times \frac{k_{GB}}{k_m} \times \frac{k_{bubble}}{k_m}, \qquad (3.8)$$

where k_{Xe} and k_m are the thermal conductivities of a UO_2 matrix with and without dispersed Xe, respectively. Both of which can be calculated from Eq. (3.5) (note: Eq. (3.3) should be used to convert the thermal conductivity for fully dense UO_2); k_{GB} is the effective thermal conductivity of a UO_2 containing GBs, and k_{bubble} is the effective thermal conductivity of a UO_2 having bubbles. In this multiplier model, each term can be evaluated separately [22]. For example, k_{bubble}/k_m can be evaluated by constructing a UO_2 matrix containing only bubbles.

When a UO_2 contains some GBs, the effective thermal conductivity (k_{GB}) can be calculated based on the grain size (*D*) and GB thermal (Kapitza) resistance (*R*) [55]. So the second term on the right-hand side of Eq. (3.8) can be calculated by

$$\frac{k_{GB}}{k_m} = \frac{1}{1+k_m\frac{R}{D}}. \tag{3.9}$$

For large bubbles, various models have been proposed, as summarized in Refs. [33, 56]. Same as in Ref. [22], Nikolopoulos et al.'s model [57] is used,

$$\frac{k_{bubble}}{k_m} = (1-p)^n, \tag{3.10}$$

where *p* is the porosity and *n* is a fitting parameter. The exponent *n* is 1.5 in Ref. [57] based on the analysis of experimental data for spherical pores and 1.75 in Ref. [22] from mesoscale simulations. So that Eq. (3.8) can be rewrite as

$$k_{GB+Xe+bubble}^{eff} = k_{Xe} \times \frac{1}{1+k_m\frac{R}{D}} \times (1-p)^n. \tag{3.11}$$

Equation (3.11) has been calibrated to predict the effective thermal conductivity of a UO_2 system having dispersed Xe, GBs, and Xe bubbles [22]. Using a similar approach, here we use our new dispersed Xe model to re-examine the thermal conductivities in HBS and unrestructured UO_2.

Figure 3.5 schematically illustrates the typical Xe distribution in a HBS and an unrestructured UO_2, which is taken from Ref. [22]. In HBS, the GB density is high because its grain size is small – typically a few hundred nanometers. These GBs are effective sinks for Xe so that they can effectively remove Xe in the grain interior of HBS. For simplicity, it is assumed that the dispersed Xe concentration in the grain interior of HBS is zero and all Xe atoms aggregate to form GB Xe bubbles (Fig. 3.5(a)). In the unrestructured UO_2, the grain size is large – about a few microns. As a result, the removal of Xe from its grain interior is less effective than in HBS. Therefore, it is assumed that the unrestructured UO_2 has dispersed Xe in the grain interior and randomly distributed Xe gas bubbles (Fig. 3.5(b)). As mentioned earlier, previous experimental studies [3, 9, 21] showed that the thermal conductivity of a HBS could be higher than that of an unrestructured UO_2 at the same burnup, because the surviving dispersed Xe in the unstructured fuel can offset the GB resistance in HBS [22]. To determine the critical Xe concentration in the unstructured fuel using our new model, the bubble porosity is assumed to be the same in HBS and unrestructured UO_2 so that the effect of gas bubbles (the third term in Eq. (3.11)) is canceled out in the two microstructures. By equating the overall effective thermal conductivities of two microstructures, the critical concentration of dispersed Xe in an unrestructured UO_2 fuel can be determined by the following equation,

$$\frac{1}{k_{Xe}}+\frac{R}{D_{large}}=\frac{1}{k_m}+\frac{R}{D_{HBS}}. \tag{3.12}$$

Here we assume $D_{large} = 3.162\ \mu m$ and $D_{HBS} = 0.577\ \mu m$, which are the same as in Ref. [22]. Then the critical concentration of dispersed Xe (C_{Xe}^*) in the unrestructured UO_2 is determined as a function of GB Kapitza resistance (R) at both 300 K and 1000 K, as shown in Fig. 3.6. For comparison, the critical Xe concentration predicted by Tonks's model [22, 32] is also shown. Both models predict a nearly linear correlation between C_{Xe}^* and R in the log-log plot. The physical meaning is that as the GB Kapitza resistance increases, C_{Xe}^* also increases in order to offset the increasing thermal conductivity reduction caused by GBs in HBS. Interestingly, each model predicts almost the same C_{Xe}^* for 300 K and 1000 K (Fig. 3.6), suggesting that C_{Xe}^* is not sensitive to temperature in both models. Compared with Tonks's model, our model predicts a larger C_{Xe}^* when R is smaller than 100 $m^2 \cdot K/GW$. For a typical GB Kapitza resistance of 10 m^2K/GW and at 300 K, our model gives $C_{Xe}^* = 5.0 \times 10^{-4}$ in the unrestructured UO_2 matrix, while Tonks's model predicts $C_{Xe}^* = 3.2 \times 10^{-5}$. The two models predict similar results only if the Kapitza resistance reaches to 100 m^2K/GW.

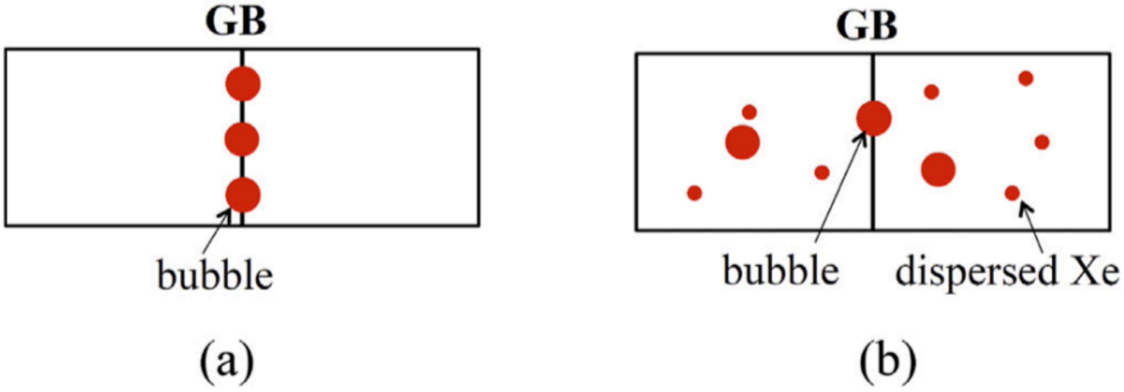

Fig. 3. 5. Assumptions of Xe distributions in two microstructures [22]. (a) HBS. All Xe atoms form GB bubbles. (b) Unrestructured UO_2 fuel. Both dispersed Xe atoms (small sphere) and Xe bubbles (large spheres) are randomly present in the system. (Images reproduced with permission.)

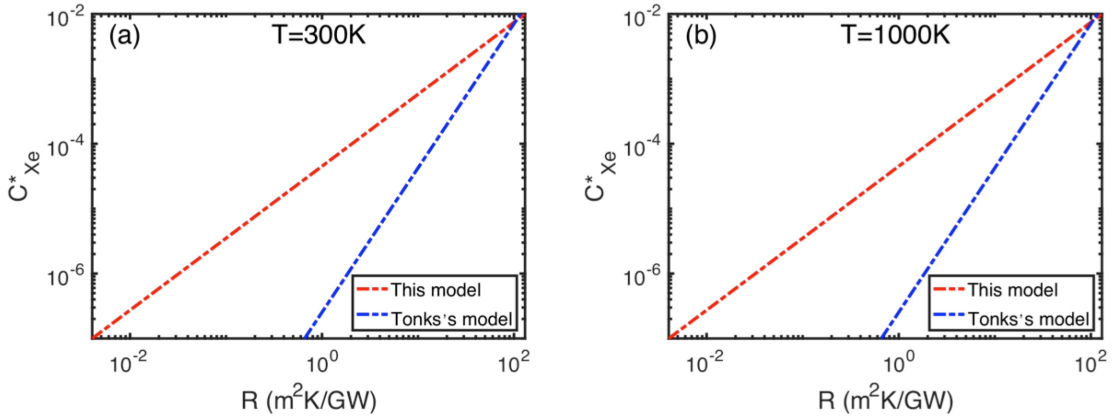

Fig. 3. 6. Critical Xe concentration (C^*_{Xe}) in the unrestructured UO₂ fuel as a function of GB Kapitza resistance (R) predicted by our new model and Tonks's model [32]. (a) T = 300 K. (b) T = 1000 K.

In reality, GBs typically do not remove dispersed Xe completely from the grain interior of HBS. Previous electron probe microanalysis (EPMA) measurement of the Xe concentration at the HBS region [58] showed that some dispersed Xe still survived. The measurement showed that the local Xe concentration has dropped from 1.1 wt.% (2.2 at.%) to 0.3 wt.% (0.6 at.%) upon the formation the HBS [22, 58]. To estimate the overall effective thermal conductivities of the two microstructures at these Xe concentrations, we use the same parameters as in Ref. [22]: $R = 10\, m^2 \cdot K/GW$, $D_{large} = 3.162\ \mu m$ and $D_{HBS} = 0.577\ \mu m$. Assuming that there are no bubbles in Eq. (3.11), our model gives the thermal conductivities of 1.919 W/m·K and 3.645 W/m·K for the unrestructured fuel and the HBS at 300 K, respectively. As a comparison, Tonks's model predicts 2.685 W/m·K and 3.424 W/m·K, respectively. Both models are consistent with experimental observation that HBS can improve the overall fuel thermal conductivity upon its formation [3, 9, 21].

3.4. Discussions and conclusions

In this chapter, molecular dynamics simulations have been conducted to examine the effect of dispersed Xe on the thermal conductivity reduction in UO_2 using three different interatomic potentials (Busker, Basak and CRG). Although these potentials predict very different absolute thermal conductivities, the normalized thermal conductivities predicted by the three potentials have quantitatively similar trends for a wide range of Xe concentrations and temperatures. Based on this unified phonon-scattering effect by dispersed Xe, a Xe scattering term is obtained from the average results of the three potentials. This Xe scattering term is added to Fink's experimental thermal conductivity model to predict the realistic thermal conductivity at a given Xe concentration and temperature. In comparison with the existing dispersed Xe model in literature that is based on one single potential [32], the new model predicts higher thermal conductivities at low Xe concentration (0.1 at.%) and lower values at high Xe concentration (2 at.%). Since the two studies are based on different approaches and there are no experimental data for validation, our new model can be considered as an alternative model to describe the effect of dispersed Xe on thermal conductivity reduction in UO_2.

The new thermal conductivity model is applied to reevaluate the effective thermal conductivities of a HBS and an unrestructured fuel in UO_2. Both our model and the literature model can qualitatively explain the counterintuitive phenomenon that why a small-grain HBS can have a higher thermal conductivity than an unrestructured large-grain fuel at the same burnup. As expected, the quantitative predictions by two models have some discrepancies. Assuming that the high density of GBs can remove all dispersed Xe in the grain interior of HBS while the large grain unrestructured fuel still has some survived dispersed Xe atoms, the critical Xe concentration in the unrestructured fuel that offsets the GB effect in HBS is estimated as a function of GB Kapitza resistance at both 300 K and 1000K. In both models, critical Xe concentration is not sensitive to temperature. At any given GB thermal resistance less than 100 m^2K/GW, our new model predicts a higher critical Xe concentration than the literature model. At a typical GB Kapitza resistance of 10 m^2K/GW, our model predicts the critical Xe concentration in the order of 10^{-4}, which is about one order of magnitude higher than that predicted by the literature model (10^{-5}). The model developed in this chapter may be implemented in fuel-performance codes such as MARMOT as an alternative model for predicting the dispersed Xe effect on the thermal conductivity reduction in UO_2 fuels. The robustness and accuracy of the model may be further improved by using more dispersed Xe concentrations and distributions, and different system sizes in the future.

Chapter 4: Effect of Xe bubble size and pressure on the thermal conductivity of UO_2 - a molecular dynamics study

The work presented in this chapter is reproduced from [W. Chen, M.W.D. Cooper, Z. Xiao, D.A. Andersson and X.M. Bai, "Effect of Xe bubble size and pressure on the thermal conductivity of UO2—Amolecular dynamics study", Journal of Materials Research 34(13): 2295-2305 (2019).], with the permission of Springer Publishing.

4.1 Introduction

As we already demonstrated in Chapter 3 that the atomistic-level modeling combined with mesoscale modeling can well explain certain thermal transport behavior in UO_2 (e.g., HBS). Besides the point defects like dispersed Xe gas atoms, it is of great importance to understand the effects of small defect clusters and large microstructures on the thermal conductivity of UO_2 at both atomistic and mesoscale.

Currently, the most widely used semi-empirical thermal conductivity model for unirradiated UO_2 was developed by Fink [7], which was fitted to many experimental data and normalized to 95% of theoretical density. The model correctly captures the phonon-dominant thermal transport behavior at intermediate temperatures and includes the additional polaron contribution at high temperatures. In terms of radiation effects, researchers have used computer modeling to study the effects of point defects and microstructures on the thermal transport properties of UO_2 from atomistic to mesoscale [13, 22, 32, 33, 59]. At the atomic scale, molecular dynamics (MD) simulation method has been widely used to study the phonon scattering effects induced by point defects, small defect clusters, and extended defects. Liu et al. [13, 32] have used

MD simulations to quantify the phonon scattering effects on the thermal conductivity of UO_2 induced by different types of point defects including dispersed xenon (Xe). The results have been integrated into Fink's analytical model [7] to predict the degradation of thermal conductivity at different defect concentrations [32]. Deng et al. [34] have studied the effect of dislocations on the thermal conductivity of UO_2 and found that the effect is small unless the dislocation density is very high. Chen et al. [35] have calculated interface thermal resistance (Kapitza resistance) of various grain boundaries in UO_2 and found that the Kapitza resistance correlates with the grain boundary energy. Lee et al. [33] have studied the effect of helium bubbles on the thermal conductivity of UO_2. The results showed that helium resolution from bubbles to fuel matrix can cause additional reduction in thermal conductivity. At the mesoscale, the effects of different microstructures and their topology on the thermal conductivity of UO_2 have been studied. Millett et al. [60] have found that the alignment of gas bubbles at grain boundaries causes more thermal conductivity reduction than randomly distributed bubbles in UO_2. Recently, Bai et al. [22] have shown that the consideration of the topology of microstructures alone in mesoscale modeling may not be sufficient to capture some important thermal transport behavior in UO_2. By including the atomistic-level phonon scattering effects induced by dispersed Xe in the UO_2 matrix [32], the work correctly explains why small-grain high burnup structures can have improved thermal conductivity than the large-grain counterparts [22]. Mesoscale modeling can also quantitatively predict the effective thermal conductivities of heterogeneous microstructures that contain dispersed Xe, gas bubbles, grain boundaries, etc. [22, 32]. It has been shown that the microstructure-based thermal conductivity model developed from mesoscale modeling can improve the engineering level fuel performance modeling significantly [32]. Therefore, it is important to understand the effects of small defects/clusters and large microstructures on the thermal conductivity of UO_2 at both atomic scale and mesoscale.

Fission gases (e.g., Xe, Kr) are expected to have significant effects on the degradation of the thermal conductivity in UO_2 [2]. These inert fission gases are insoluble in UO_2 and they tend to precipitate as intergranular and intragranular bubbles [61]. In addition, fission gas atoms can be trapped by defects or defect clusters and become dispersed fission gas atoms in the UO_2 matrix. MD calculations have shown that Xe atoms are likely to occupy the Schottky defect sites (one uranium vacancy and two nearest oxygen vacancies) [40]. Xe may also stay at O vacancy, U vacancy, UO divacancy, and octahedral interstitial site, depending on the stoichiometry of UO_2 [39]. Those defects will diffuse across the defect sites and form into defect clusters. Cluster that has the radius larger than $0.5nm$ may be considered as small bubbles, which involves surface diffusion around the bubble interface [39]. In analytical modeling, gas bubbles are typically treated as empty voids [62, 63]. Many theoretical models such as Loeb equation [63] and Maxwell-Eucken equation [62] have been proposed to describe the correlation between thermal conductivity and porosity. However, the thermal conductivity reduction in these models only depends on porosity regardless of void size and distribution. These models may be valid for large voids whose size is much larger than the phonon mean free path (~ a few nanometers). When void size is comparable with the phonon mean free path, the phonon scattering effects induced by the void surface cannot be neglected. To include the void size effect, Alvarez's model [64] has been developed as a function of bubble size, phonon mean free path, and total porosity. The model predicts that at a given porosity the thermal conductivity increases with void size initially and then reaches a staturated value beyond a critical void size. By comparing to the Maxwell-Eucken equation [62], Tonks et al. [32] have theoratically determined that the critical void radius is about 5 nm. When voids are filled with gase to form bubbles, intuitively the effective thermal conductivity may increase slightly because the gas in bubbles can contribute to the thermal conduction [22], even though the thermal conductivity of gas is very low. In other words, the Alvarez's model may be applied to gas bubbles. However, Lee et al. [33] have used MD simulations to show that helium bubbles can cause more thermal conductivity reduction than empty voids and the reduction increases with the increasing helium density in bubbles. The reason is that some helium atoms can diffuse from the bubbles into the surround UO_2 matrix. Therefore, they concluded that the helium resolution from bubbles can cause additional phonon scattering effects. Since the atomic size of helium is small, the gas resolution process may take place easily. However, such a gas resolution process may not happen in Xe bubbles because the atomic size of Xe is comparable with that of uranium. Since Xe is the primary gaseous fission products in UO_2 fuels and the size of intragranular bubbles is typically about a few nanometers [65, 66], it is of great interest to investigate whether small Xe bubbles can cause additional thermal conductivity reduction than empty voids. To our best of knowledge, such effects have not been demonstrated to date.

In this work, we have examined the effects of Xe bubbles on the thermal conductivity of UO_2 at different Xe bubble sizes. To compare the results, empty voids of the same sizes are also studied. In these studies, the total porosity is fixed so that the effects of bubble/void size on the thermal conductivity can be elucidated. The results may help the development of science-based models to better predict the thermal conductivity degradation due to the presence of Xe bubbles.

4.2 Simulation detail

Similar to the methodologies described in Chapter 3, non-equilibrium molecular dynamics (NEMD) method was used in LAMMPS to calculate the thermal conductivities of a UO_2 system that contains voids or Xe gas bubbles[50, 67, 68]. The Basak potential [44] was used to describe the interatomic interactions in UO_2. The potential parameters are described in Table 4.1. The simulation system contains $6 \times 6 \times 75$ UO_2 unit cells with the longest length along the z direction, as shown in Fig. 4.1. Therefore, the system contains 10,800 uranium atoms and 21,600 oxygen atoms before any voids or Xe bubbles are introduced. Periodic boundary conditions were employed in all directions. Different from Lee et al.'s helium bubble work [33] in which only single bubble was modeled, in our work the primary simulation system contains multiple voids or Xe bubbles while the total porosity was fixed at p=2% (Fig. 4.1). Using this approach, the effects of bubble or void size on the thermal conductivity reduction can be compared fairly at the same porosity. To maintain the charge neutrality of the simulation system, the removed uranium and oxygen atoms in each void/bubble had the ratio of U:O = 1:2. The largest void/bubble radius was about 1 nm, in which 108 uranium and 216 oxygen atoms were removed. The smallest vacancy cluster created in this work contains one uranium vacancy and two oxygen vacancies ($1V_U + 2V_O$), or one Schottky vacancy cluster. Strictly, small clusters cannot be called as voids or bubbles. Here we call all these defect clusters as voids or bubbles simply for convenience. To describe the Xe content in a bubble, the ratio of the number of Xe atoms in a bubble to the number of vacant uranium sites (i.e., Xe:V_U ratio) is used. For example, if all the uranium sites in a bubble are occupied by Xe, Xe:V_U = 1.

Table 4. 1. Potential parameters of Basak potential [44] for pure UO$_2$ and Geng's potential [48] for Xe-UO$_2$ interactions. The charges for U and O are q_U = 2.4 and q_O = -1.2, respectively.

Parameters (units)	U-U	U-O	O-O	U-Xe	O-Xe	Xe-Xe
A_{ij}(eV)	294.63999	693.64877	1633.00515	4887.7		
ρ_{ij}(Å)	0.327022	0.327022	0.327022	0.415		
c_{ij}(eVÅ^6)	0.0	0.0	3.948788	0.0		
D_{ij}(eV)		0.577188				
β_{ij}(Å^{-1})		1.65				
r_{ij}^0(Å)		2.369				
ε(eV)					0.0099	0.017
σ(Å)					2.50	4.29

The MD simulation set is the same as described in Chapter 3.2. The only difference is the input structures, which is described in Fig. 4.1.

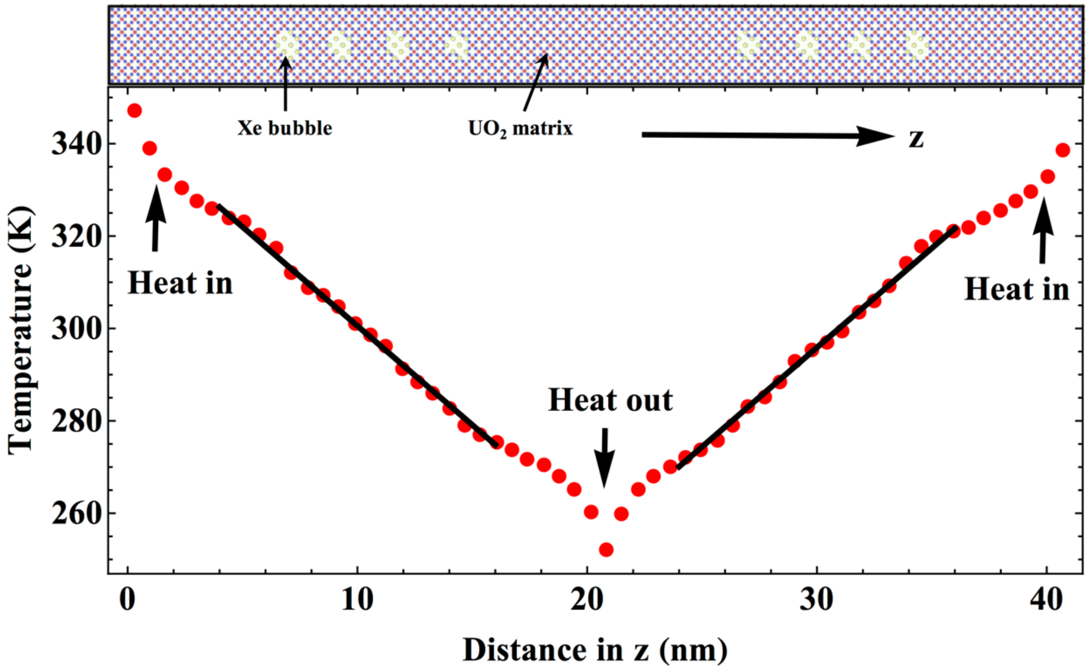

Fig. 4. 1. Illustration of the NEMD method ("direct method") for calculating the thermal conductivity in a UO$_2$ system containing multiple Xe bubbles. The filled red circles represent the temperatures calculated by MD along the z direction of the simulation box. The black solid lines show the two linear fitting ranges along the temperature profile.

4.3 Results

4.3.1 Validation of the Alvarez's model

First the thermal conductivity reduction due to empty voids at 300 K was calculated. The results were used as references for later studies of the effect of Xe-filled bubbles on the thermal conductivity reduction. For single crystal UO$_2$, the thermal conductivity predicted by the Basak potential is 18.02 W/m·K at 300 K in this work, which is in good agreement with the value of 17.34 W/m·K obtained by Chernatynskiy et al. [36] using the same potential. The small discrepancy may be caused by different simulation dimensions used in the two studies. Since different potentials predict different thermal conductivities for UO_2 [36], in this work all thermal conductivities of void/bubble-containing systems are normalized with respect to the single crystal value to highlight the effect of void/bubble on the thermal conductivity reduction. Two cases were studied for empty voids: single void of different radii (thus different porosities) and multiple voids with a fixed porosity of $p = 2\%$. The results are shown in Figs. 4.2(a) and 4.2(b) respectively. The simulation results are compared with Alvarez's model [64],

$$\frac{k_{Alvarez}}{k_S} = \left\{\frac{k_S}{k_{Loeb}} + \frac{9}{2}p\left(\frac{l}{r}\right)^2 (1 + \frac{3}{\sqrt{2}}\sqrt{p}) / \left[1 + (0.864 + 0.29e^{-\frac{1.25r}{l}})l/r\right]\right\}^{-1}, \tag{4.1}$$

where k_S is the thermal conductivity of a perfect single crystal, p is porosity (void volume fraction), l is phonon mean free path, and r is the void radius. The k_{Loeb} term is a simple model to describe the thermal conductivity in a porous media and has the form [63],

$$\frac{k_{Loeb}}{k_S} = 1 - p. \tag{4.2}$$

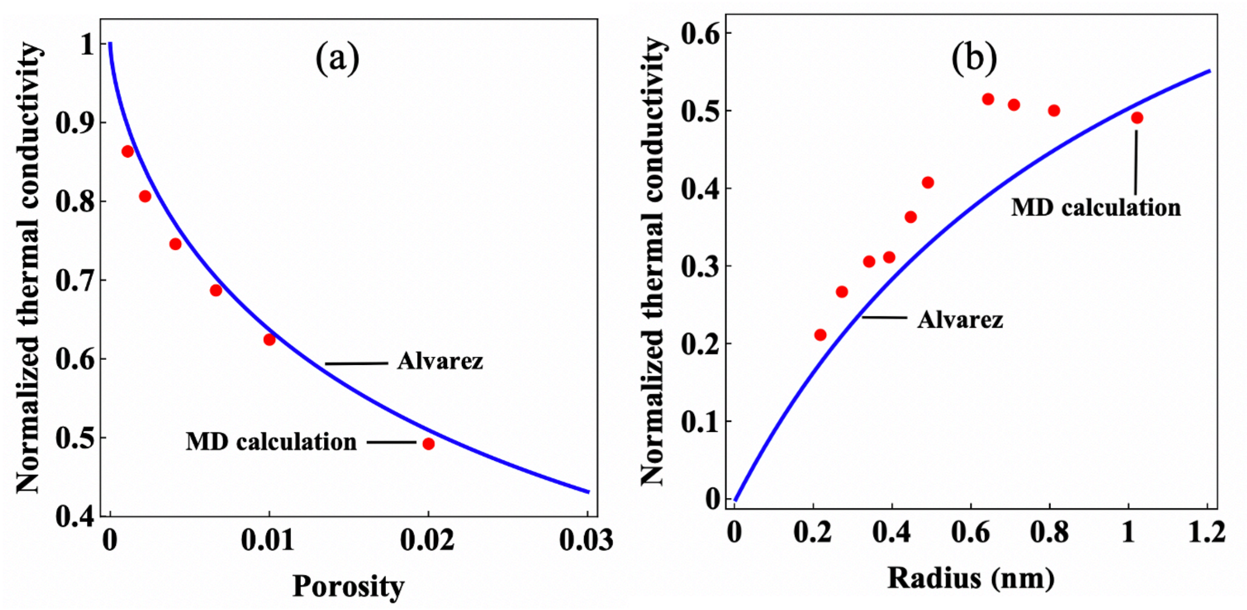

Fig. 4. 2. Comparison between the thermal conductivities calculated from MD simulations (filled circles) and Alvarez's theoretical model [64] (lines). All MD-calculated thermal conductivities are normalized with respect to the single crystal value at 300 K. (a) Single void. Different porosity corresponds to different void radii. The phonon mean free path of $l = 9.8$ nm is used in Alvarez's model. (b) Multiple voids with a fixed porosity of $p = 2\%$. The solid line is Alvarez's model with $l = 9.8$ nm. The dashed line is the perfect fit of Alvarez's model to the simulation data, which yields $l = 11.7$ nm.

The advantage of Alvarez's model over Loeb's model is that the former includes the phonon scattering effects when the phonon mean free path l is comparable or larger than the bubble radius r. When $l \ll r$, the phonon scattering effect is negligible and Alvarez's model is the same as Loeb's model (Eq. (4.2)). The comparison between Alvarez's model and the MD results for single voids is shown in Fig. 4.2(a). The best fit gives the phonon mean free path of $l = 9.8$ nm at 300 K. Previously, Lee et al. [33] obtained the phonon mean free path of $l = 3.6$ nm at 800 K in a UO_2 system with $10 \times 10 \times 40$ unit cells. This discrepancy may be mainly due to the temperature effect because a higher temperature yields a shorter phonon mean free path. In addition, the phonon mean free path may depend on the simulation system size [69, 70]. Nevertheless, both studies show that Alvarez's model can well describe the non-linear decrease of thermal conductivity with increasing porosity for single voids. The comparison between Alvarez's model and the MD results of multiple voids with a fixed porosity of 2% is shown in Fig. 4.2(b). In this case, the number of voids (vacancy clusters) varies with the void radius, ranging from 2 to 108 Schottky-vacancy clusters. The MD results show that initially the thermal conductivity increases nearly linearly with void radius then reaches a saturated value of about 0.5 at about $r = 0.6$ nm (27

Schottky-vacancy clusters). This critical radius indicates that the phonon scattering mechanism may change from point-defect-dominant scattering to interface-dominant scattering. It also indicates that at a given porosity, many dispersed small vacancy clusters can cause more thermal conductivity reduction than if they aggregate to a few large voids. Therefore, defect clustering can improve the thermal conductivity. Using the same phonon mean free path as for the single void case (l = 9.8 nm), Alvarez's model slightly underpredicts the thermal conductivity in the linear regime. The best fit gives a slightly larger value, l = 11.7 nm. The thermal conductivity predicted by Alvarez's model keeps increasing with the void radius and eventually will saturate at the value of 0.98 as predicted by Leob's model. Tonks et al. [32] compared the Maxwell-Eucken equation with Alvarez's model and determined that the threshold void radius for the transition is about 5 nm for a tolerance of 5% between two models. Therefore, the discrepancy in the critical radius between MD and the theoretical analysis is about one order of magnitude. In addition, the thermal conductivity reduction in the saturated regime obtained from MD simulations is significantly larger than that predict by the theoretical models. Similar large discrepancy was also obtained in Lee et al.'s MD work [33]. The discrepancy may be caused by the finite system size and non-random distribution of voids in MD simulations. For example, the cross-section area in our MD simulations is relatively small (6×6 unit cells). Due to the periodic boundary conditions, voids may align with their periodic images so that the assumption of random void distribution in Alvarez's model breaks down. On the other hands, the theoretical models that are purely based on the porosity (e.g., Leob's model) were found to disagree with experimental data [57] so that many different models have been proposed [33]. Therefore, more research is needed to clarify the underlying reasons for the discrepancies between MD simulations and theoretical models regarding the critical radius and the thermal conductivity reduction ratio.

4.3.2 Degradation of Xe bubbles on the UO_2 thermal conductivity

To study the effect of Xe bubbles on the thermal conductivity, the empty voids studied above were filled with Xe. Two Xe:V_U ratios were used: 0.5 (half filled) and 1.0 (full filled). The total porosity in each Xe-containing system is still 2%. Since the system dimensions and pore configurations are the same for voids and bubbles, the differences in thermal conductivity reduction between them are simply due to the Xe content in bubbles. The comparison of the thermal conductivity between three cases (empty voids, half-filled bubbles, and full-filled bubbles) are shown in Fig. 4.3(a). Similar to the voids, there are two distinct regimes for Xe bubbles: point defect scattering dominant regime and surface scattering dominant regime. The critical bubble sizes for the transition are also similar as in the void-containing system, about 0.6 nm. When the defect cluster size is small, the thermal conductivities in the three cases are similar, although a full-filled Xe cluster has a slightly lower thermal conductivity than those in the other two cases at the same cluster size. When the defect cluster size is greater than the critical size, the half-filled bubbles result in nearly identical thermal conductivities as the empty voids. However, the full-filled bubbles lead to lower thermal conductivities than the empty voids. In addition, the thermal conductivity reduction induced by the full-filled Xe bubbles becomes more pronounced as the bubble size increases. Similar to helium bubbles studied by Lee et al. [33], our results are surprising because Xe gas can be a heat conducting medium and the Xe addition in a void should lead to a higher thermal conductivity. However, our MD results show an opposite trend.

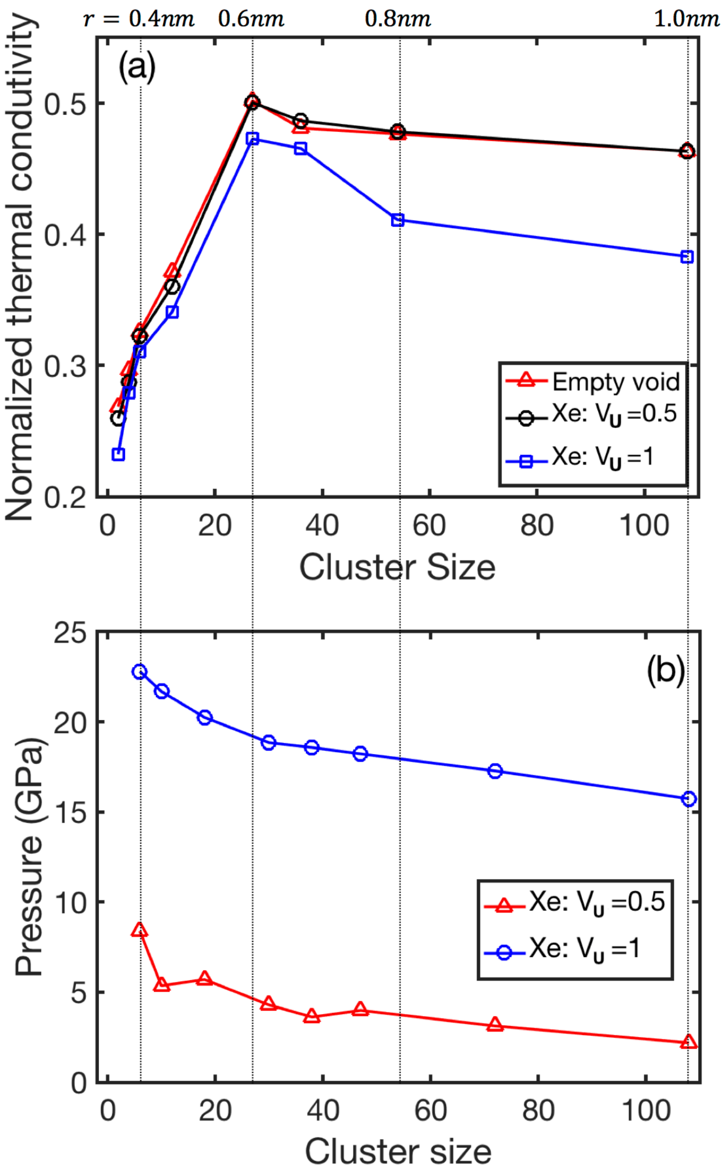

Fig. 4. 3. Effect of pore size and Xe bubble pressure on the thermal conductivity in a system contains multiple pores. The porosity is 2% in all thermal conductivity simulations. The pore size is represented by the number of removed UO_2 pairs in the pore. (a) Normalized thermal conductivity as a function of pore size. Three types of pores are studied: empty voids, half-filled bubbles (Xe:V_U = 0.5), and full-filled bubbles (Xe:V_U = 1.0). (b) Xe bubble pressure as a function of bubble size.

4.3.3 Xe bubble pressure effect on the UO_2 thermal conductivity

It is well known that bubble pressure increases with the Xe density or Xe:V_U ratio in a bubble. To investigate how the bubble pressure changes when the Xe:V_U ratio varies from 0.5 to 1.0, bubble pressures were calculated based on the virial stresses of Xe atoms for the two Xe:V_U ratios at different bubble sizes, as shown in Fig. 4.3(b). Generally speaking, the bubble pressure in a full-filled bubble is about 4 times higher than that in a half-filled bubble at a given bubble size. Since small bubbles are over-pressurized [71], bubble pressure decreases with increasing bubble size. For the full-filled bubbles, bubble pressure is in the range of 16 – 23 GPa, which agrees well with Liu et al.'s MD results of 15 – 25 GPa [71] using a different interatomic potential. From Figs. 4.3(a) and 4.3(b), it seems that there exists a critical pressure or Xe:V_U ratio, below which a Xe bubble behaves like a void and above which a Xe bubble causes extra thermal conductivity reduction.

To determine the critical bubble pressure or Xe:V_U ratio for the extra thermal conductivity reduction, a single bubble with a radius of 1 nm is created. Different Xe:V_U ratios ranging from 0 to 1.0 are used to fill the bubble with Xe. The normalized thermal conductivity as a function of bubble pressure at 300 K is shown in Fig. 4.4(a). When bubble pressure is low, the thermal conductivity is close to that of the empty void (i.e., the value at 0 GPa). When bubble pressure is about 7 GPa, which corresponds to Xe:V_U = 0.75, the thermal conductivity has a clear drop. As pressure increases further, thermal conductivity decreases almost linearly with pressure. Although the Xe density in bubbles has a significant effect on thermal conductivity at 300 K, we found that this effect becomes weaker at high temperatures. Figure 4.4(b) shows the thermal conductivity as a function of Xe:V_U ratio at 300 K, 500 K, 1300 K and 1500 K. The results show that the critical Xe:V_U ratio increases with temperature. For example, the critical ratio is at 0.75 at 300 K, while it shifts to 0.83 at 500 K. At elevated temperatures (1300 K and 1500 K), the effect of Xe density on thermal conductivity seems to disappear, suggesting that temperature effects may dominate the thermal transport at high temperatures. It may also be that the large thermal noises at high temperatures, some are artificial due to the finite system size, make the effect less discernible.

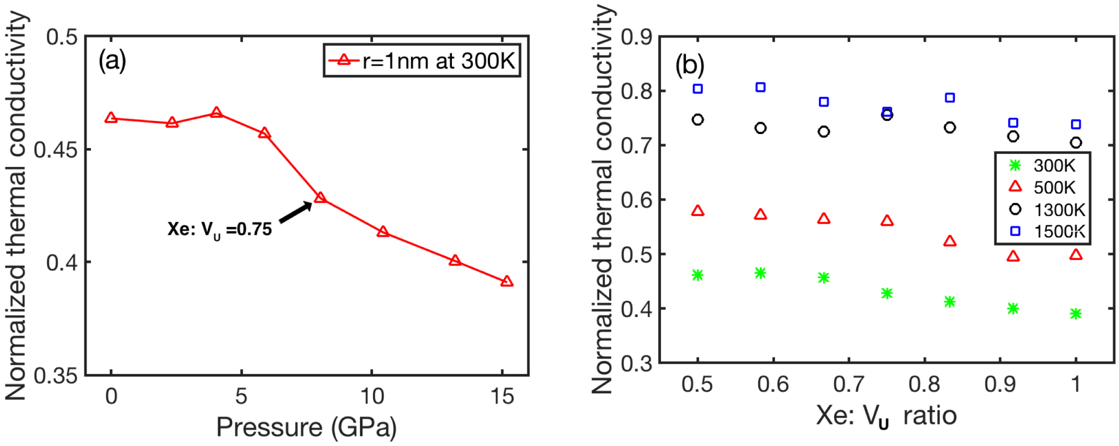

Fig. 4. 4. Effect of bubble pressure (or Xe:V_U ratio) and temperature on the thermal conductivity in a system containing a single pore with r = 1 nm. All thermal conductivities are normalized to the single crystal value at the respective temperature. (a) Normalized thermal conductivity as a function of bubble pressure at 300 K. (b) Normalized thermal conductivity as a function of Xe:V_U ratio at four different temperatures (300, 500, 1300 and 1500 K).

The thermal conductivity reduction at high Xe:V_U ratios is similar as in the previous helium bubble work by Lee et al. [33]. In that work, they found that helium atoms can diffuse away from a helium bubble into the UO_2 matrix. The formation of such a diffuse interface was also confirmed by Liu et al.'s MD simulations [71]. As a result, thermal conductivity is further reduced with respect to an empty void due to the formation of this diffuse interface. However, such a helium gas resolution mechanism may not be applicable for Xe because Xe has a much larger atomic size. To understand the underlying mechanism for the additional thermal conductivity reduction caused by Xe bubbles, the final positions of atoms near a void/bubble are visualized in Fig. 4.5. The vectors indicate the displacements of atoms with respect to their initial positions, with arrow tails showing the initial atom positions. Figures 4.5(a – c) show the atom positions around a 1 nm void/bubble with three Xe:V_U ratios: 0, 0.5, and 1.0, respectively. For the empty void (Fig. 4.5(a)), only a few oxygen atoms have discerned displacements. For the half-filled bubble (Fig. 4.5(b)), again only a few oxygen atoms have large displacements, but uranium atoms remain at their original positions. The Xe atoms have significant displacements, but they never leave the bubble. When the bubble is fully filled (Fig. 4.5(c)), many oxygen and uranium atoms have distinguishable displacements. The vector directions indicate that most atoms displace away from the bubble. This is because the full-filled bubble has a very high pressure, as shown in Fig. 4.3(b). Therefore, the bubble tends to release its pressure through displacing the surrounding atoms. Interestingly, atoms above the bubble have more displacements than those below the bubble. This is because the temperature above the bubble is higher than that below the bubble due to the thermal gradient. Since a crystal lattice at a higher temperature is softer than that at a lower temperature, these atoms in the hotter region can be displaced more. It should be noted that Xe atoms do not have noticeable displacements in Fig. 4.5(c), and they do not diffuse into the matrix either. Therefore, Xe behaves like a solid when the bubble is fully filled. This observation is consistent with the work by Liu et al. [71] in which they found that uranium atoms around a Xe bubble were displaced to release the bubble pressure for $Xe:V_U = 1.0$. The interface distortion around an over-pressurized bubble can cause additional phonon scattering. A similar bubble surface distortion effect on thermal conductivity reduction was also observed in tungsten with over-pressurized helium bubbles [72]. As a result, the thermal conductivity is reduced further with respect to an empty void or half-filled bubble. Therefore, although the phenomenon of additional thermal conductivity reduction in UO_2 is observed for both over-pressurized He bubbles [33] and Xe bubbles, the underlying mechanisms are different. In the former, helium resolution creates a diffuse interface that causes additional phonon scattering. In the latter, the distorted bubble surface in an over-pressurized bubble induces the additional phonon scattering. It seems that temperature does not affect the different behaviors of gas atoms in UO_2. For example, in the work by Liu et al. [71], both helium and Xe bubbles were annealed at 1000 K. Helium diffused to the UO_2 matrix while Xe remained inside the bubble, which is consistent with our Xe results at 300 K.

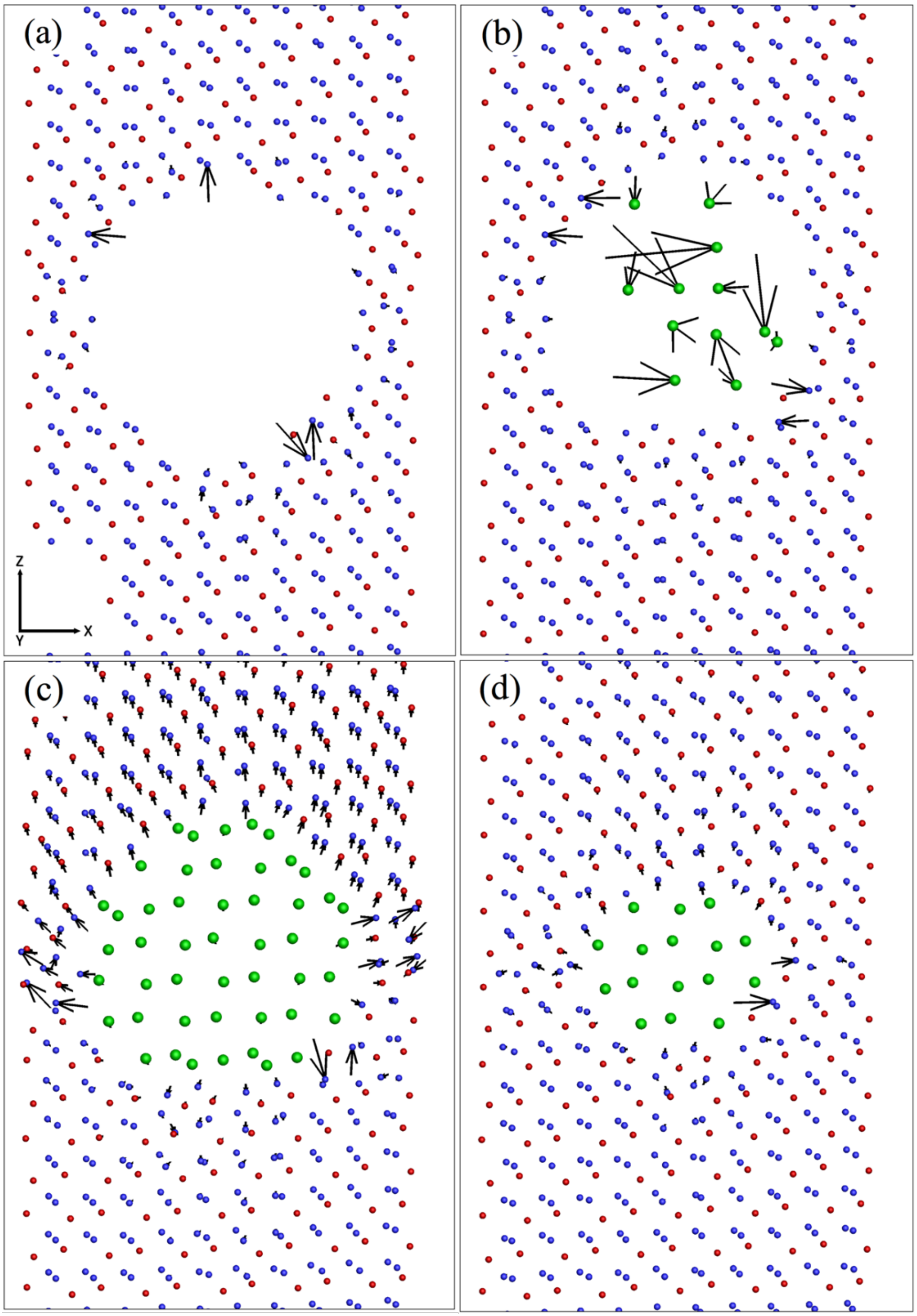

Fig. 4. 5.Visualization of the final atom positions near a bubble or void, with red spheres being U atoms, blue spheres being oxygen atoms, and green spheres being Xe atoms. The atomic displacements are indicated by black vectors with the tails representing the initial atom positions. The vector length is proportional to the actual atom displacement. (a) An empty void with r = 1

nm. (b) A half-filled bubble (Xe:V_U *= 0.5) with r = 1 nm. (c) A full-filled bubble (Xe:*V_U *= 1.0) with r = 1 nm. (d) A full-filled bubble (Xe:*V_U *= 1.0) with r = 0.6 nm.*

The above results show that bubble pressure or Xe:V_U ratio is an important factor for causing the interface distortion. Currently there is no consensus on the pressure or Xe:V_U ratio in Xe bubbles in UO_2. Garcia et al. [73] estimated that the typical Xe gas bubble pressure in UO_2 is in the range of 2 – 5 GPa based on their experimental measurements using X-ray absorption spectroscopy. If this is always true, bubbles may be only half-filled and they may behave similarly as voids. Based on the experimental measurements and Ronchi's model [74], Nogita et al. [75] estimated that Xe bubble pressure was in the range 1.5-15 GPa for a bubble radius between 4 – 10 nm. Based on MD simulations, Liu et al. [71] concluded that the Xe:V_U ratio is likely to be 1.0 in pre-existing voids if Xe diffusion kinetics allows. The calculated bubble pressure is about 15 GPa for a 1 – 2 nm bubble. If this happens in reality, bubbles may be fully-filled and they may cause more thermal conductivity reduction than voids.

It should be noted that bubble surface distortion depends on not only bubble pressure but also bubble size because smaller bubbles can accommodate higher pressures [71]. To demonstrate the effect of bubble size, Figure 4.5(d) shows the distortion of surface atoms around a full-filled bubble with a radius of 0.6 nm (27 Schottky vacancy clusters). Compared with the larger bubble (Fig. 4.5(c)), the surface atoms around the smaller bubble have much smaller displacements (Fig. 5(d)). As a result, the thermal conductivity of this full-filled bubble is only slightly lower than the empty void, as shown in Fig. 4.3(a).

4.3.4 Special Xe clusters

As mentioned earlier, there exists a critical void/bubble size below which point defect scattering dominates (Fig. 4.3(a)). In this regime, our MD results show that incorporation of Xe into the small vacancy clusters still leads to the extra reduction of thermal conductivity, even though the atoms near the clusters do not have much distortion (e.g., Fig. 4.5(d)). To verify this, we study the effect of Xe incorporation into a special vacancy cluster - octahedron cluster on the thermal conductivity of UO_2. An octahedron cluster consists of six uranium vacancies and eight oxygen vacancies ($6V_U$: $8V_O$). Previous DFT calculations [39] showed that this cluster is surprisingly stable so that it may be important for Xe bubble nucleation. In addition, to further validate that our results are not specific to the interatomic potential, here we use the recently developed embedded atom method (EAM) potential [45, 46] to study the effect of Xe incorporation into octahedron clusters. In this potential, an additional EAM component is added to Eq. (4.1) to include the many-body effects in the UO_2. The Xe-U and Xe-O are described by the Buckingham potential, and the Xe-Xe interaction was originally developed the Tang et al. [49]. Note these potential parameters can be downloaded online [76].

Here the simulation system contained $5 \times 5 \times 50$ UO_2 unit cells initially. Then 5 octahedron clusters per 1280 uranium atoms were created so that the total porosity in this system is 2.34% with respect to the uranium sites. In each octahedron cluster, up to 8 Xe atoms were incorporated. The calculated thermal conductivities were used to fit to a semi-empirical model [13]:

$$k = \frac{1}{A + B \cdot T + C \cdot x}, \tag{4.6}$$

where *A* and *B* are parameters for the non-defective lattice, *C* is a scattering parameter for one type of defects or clusters, *T* is temperature, and *x* is the lattice concentration of defects or clusters. The parameters *A* and *B* are listed in Table 4.2, which were previously determined by fitting to the spin scattering adjusted MD data [13]. Therefore, in this work we only need use MD results to determine the scattering parameters (*C*) for different number of Xe atoms occupying the octahedron cluster (nXe : $6V_U$: $8V_O$). These determined parameters are listed in Table 4.2. Note a smaller scattering parameter means a higher thermal conductivity at a given temperature. It can be seen that the scattering parameter has a non-linear relationship with the Xe:V_U ratio. The general trend is that the scattering parameter increases with the increasing Xe:V_U ratio. In other words, the more Xe atoms incorporated into octahedron clusters, the lower the thermal conductivity. This trend is consistent with the above results obtained from the Basak potential (Fig. 4.3(a)), indicating that the conclusions in this work are not specific to the interatomic potentials used. Table 4.2 also shows that when the Xe:V_U = 4:6 = 0.667, the scattering parameter increases significantly, suggesting that a critical Xe:V_U ratio may exist. Figure 4.6 shows the thermal conductivity as a function of the Xe:V_U ratio in the octahedron cluster at 300 K, which is calculated based on Eq. (4.6) and the parameters are listed in Table 4.2. Clearly, the thermal conductivity decreases with the increasing number of Xe atoms in octahedron clusters. Overall, both Basak potential and EAM potential predict that incorporation of Xe into vacancy clusters or small voids causes additional decrease in thermal conductivity, which is counter-intuitive and such effect should be included in mesoscale or analytical modeling.

Table 4. 2. Parameters obtained from MD simulations for predicting the thermal conductivity of Xe-filled octahedron clusters using Eq. (4.6).

UO$_2$ single crystal parameters	
A	$3.11 \times 10^{-2}\ mKW^{-1}$ [13]
B	$2.08 \times 10^{-4}\ mW^{-1}$ [13]
Octahedron cluster scattering parameters	
$C_{\{6V_U:8V_O\}}$	$21.83\ mKW^{-1}$
$C_{\{Xe:6V_U:8V_O\}}$	$21.87\ mKW^{-1}$
$C_{\{2Xe:6V_U:8V_O\}}$	$23.99\ mKW^{-1}$
$C_{\{3Xe:6V_U:8V_O\}}$	$23.99\ mKW^{-1}$
$C_{\{4Xe:6V_U:8V_O\}}$	$26.08\ mKW^{-1}$
$C_{\{5Xe:6V_U:8V_O\}}$	$30.31\ mKW^{-1}$
$C_{\{6Xe:6V_U:8V_O\}}$	$29.08\ mKW^{-1}$
$C_{\{7Xe:6V_U:8V_O\}}$	$31.32\ mKW^{-1}$
$C_{\{8Xe:6V_U:8V_O\}}$	$39.85\ mKW^{-1}$

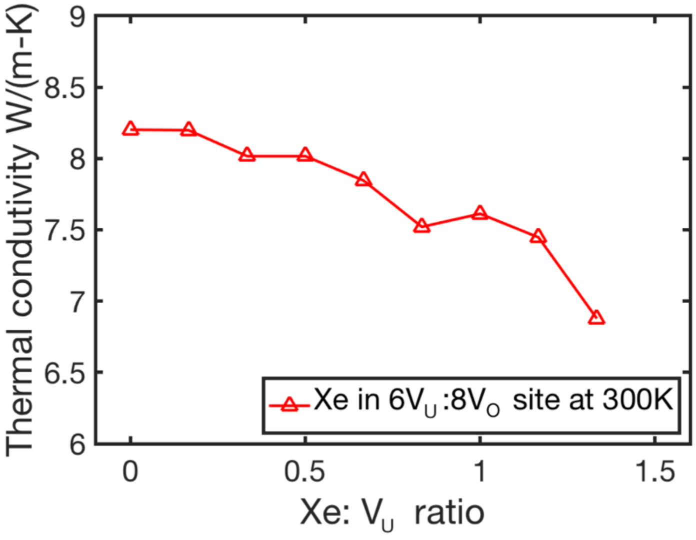

Fig. 4. 6.Thermal conductivity of the system containing Xe-filled octahedron clusters as a function of Xe:V_U *ratio at 300K. The results were calculated based on the EAM potential. (courtesy to M.W.D. Cooper and D.A. Andersson at Los Alamos National Lab)*

4.4 Conclusion and discussion

In this work, MD simulations are conducted to study the size and pressure effects of small Xe bubbles on the thermal transport properties in UO_2. The results are compared with empty voids of the same sizes to elucidate the role of Xe addition on the thermal conductivity. The results show that for both voids and Xe bubbles, at a fixed porosity the thermal conductivity initially increases with pore size then reaches a saturated value, suggesting that there is a transition from point defect dominant phonon scattering to surface dominant phonon scattering. This transition also demonstrates that dispersed Xe atoms or vacancies typically result in a lower thermal conductivity than clustering them into bubbles or voids. The critical radius for the transition is about 0.6 nm, which is much smaller than the theoretical prediction of 5 nm [32]. In terms of the effect of Xe addition, it is found that half-filled Xe bubbles ($Xe:V_U = 0.5$) give nearly the same thermal conductivity as empty voids, while full-filled bubbles ($Xe:V_U = 1.0$) lead to additional reduction in thermal conductivity with respect to empty voids. Further analysis shows that this effect becomes important when the $Xe:V_U$ ratio is greater than 0.75. In addition, this effect is found to exist even when the Xe cluster size is small, although it is not as significant as in the relatively large bubbles. The results are surprising because it is usually assumed that Xe can serve as a heat conducting medium [22] so that Xe bubbles can improve the thermal conductivity in comparison with empty voids. Through visualization of the displacements of bubble surface atoms, it is found that bubble surface atoms are displaced to release the bubble pressure. In addition, Xe atoms are found to stay within bubbles because their atomic size is large. The bubble-pressure-induced surface distortion causes additional phonon scattering and therefore further reduces the thermal conductivity. This mechanism is different from the helium resolution mechanism in helium bubbles [33], because helium has a small atomic size and can diffuse into the UO_2 matrix to form a diffuse interface. This work suggests that the surface distortion of over-pressurized Xe bubbles is an important surface scattering mechanism, in particular when bubble size is small such as intragranular bubbles. Therefore, this mechanism should be incorporated in mesoscale modeling of thermal conductivity degradation due to small Xe bubbles in the future.

Chapter 5: Temperature and composition-dependent U-Zr thermal conductivity model

The work presented in this chapter is reproduced from [W. Chen and X.M. Bai, “Temperature and Composition Dependent Thermal Conductivity Model for U-Zr Alloys", Journal of Nuclear Materials 507, 360-370 (2018)], with the permission of Elsevier Publishing.

5.1. Current study on U-Zr thermal conductivity

As suggested by the U-Zr phase diagram, α, β, δ, and γ phases all present in the irradiated U-Zr fuels. These phases have different Zr compositions and thermal conductivities. In turn, the phase transformations induced by the constituent redistribution can alter the fuel temperature profile and affect the fuel performance properties. Therefore, understanding the correlation between the thermal conductivity and alloy composition as well as temperature is important for predicting the fuel microstructural evolution and change of fuel physical properties.

There have been extensive studies on the thermal conductivity of U-Zr experimentally and analytically. The composition- and temperature-dependent thermal conductivities of some U-Zr alloys have been measured experimentally [77-81]. Most of those data are summarized by Janney et al. in a new Metallic Fuels Handbook [82]. These results show that the thermal conductivities of U-Zr alloys increase with increasing temperature, indicating that the thermal transport in U-Zr alloys is mainly mediated by free electrons rather than phonons. In general, the thermal conductivity also decreases with the increasing Zr concentration due to the alloying effects of Zr. Several thermal conductivity models for U-Zr based alloys have been developed by fitting to some of these experimental data. The early models developed by Ogata [83] and Hofman et al. [84] have shown reasonable agreement with experimental data. However, these models have limited extrapolation ranges in composition and temperature. As Kim et al. [85] pointed out, these models either predict negative thermal conductivities at room temperature or significantly underpredict the thermal conductivity at high Zr compositions. Therefore, these models may result in incorrect predictions of thermal conductivity at the fuel rod center where Zr becomes enriched due to constituent redistribution. Kim et al. [85] developed a semi-empirical model that has significant improvement to those early models. This model can predict very reasonable thermal conductivities of U-Zr alloys as well as other U based alloys for a wide range of temperatures and Zr compositions. Recently, an improved model based on Kim's model has been developed and implemented in the Bison fuel performance code by scientists at Los Alamos National Laboratory (termed as "LANL" in Bison's manual) [86]. However, the accuracy of these models is still not very satisfactory for some composition and temperature ranges. For example, at low Zr (high U) concentrations such as U-1.5Zr and U-5Zr which are relevant to the reactor fuel compositions, the model overpredicts the thermal conductivity; At high Zr concentrations such as U-70Zr and U-77Zr (Note according to our conversion, the U-77wt.%Zr mentioned in Kim's paper should be U-79.4wt.%Zr for U-91at.%Zr), the model predicts that the thermal conductivity has a minimum at the low temperature regime, which is similar to pure Zr. However, the experimental data [78] do not show such a minimum at these compositions. Instead, the thermal conductivities at these compositions increase almost linearly with temperature. Such discrepancies may limit the model to be applied to the regimes outside of the fitting ranges.

5.2. Model development and description

In this Chapter, we have developed a new semi-empirical model that can predict the thermal conductivities of U-Zr alloys for the full composition range and a wide range of temperatures. The model is based on the assumption that lattice (phonon) thermal conductivity is negligible at temperatures above the Debye temperature. The Widemann-Franz law is applied to correlate the thermal resistivity with the electrical resistivity. For pure U and Zr metals, the temperature-dependent thermal resistivities are empirically fitted to the theoretical model that considers different electron scattering effects [87]. For U-Zr alloys, a semi-empirical mixing rule is applied to interpolate the thermal conductivities at different Zr concentrations. Compared with previous models, our model has improvement for predicting the thermal conductivities of U-Zr alloys, especially for high U (low Zr) alloys and at the low-temperature regime for some high Zr alloys. As a validation test, the model is used to compare with some independent experimental results that are not included in the model fitting. Reasonable agreement is obtained for most compositions and temperatures.

5.2.1 Electronic thermal conductivity

In general the thermal conductivity of a metal is contributed by two major parts: electronic thermal conductivity (k_e) and lattice (phonon) thermal conductivity (k_p) [87]:

$$k_{tot} = k_e + k_p \,. \tag{5.1}$$

Though this rule is valid for most metals, it is difficult to separate these two individual contributions. In pure metals, it has been argued that the lattice thermal conductivity only contributes to a very small fraction of the total thermal conductivity [88]. For U-Zr alloys, experimental measurements show that their thermal conductivities increase almost linearly with the increasing temperature at temperatures above 300 K [77-79], which is a clear indication that free electrons are the main carriers for heat conduction in these alloys. If phonons were the main heat carriers, the thermal conductivities would decrease with temperature. Therefore, in this work, the lattice thermal conductivity is assumed to be zero for both pure metals and U-Zr alloys. For free-electron-mediated thermal transport, the correlation between the electronic thermal conductivity (k_e) and the electrical conductivity (σ) can be described by the Wiedemann-Franz law [87],

$$\frac{k_e}{\sigma} = L \cdot T, \qquad (5.2)$$

where L is Lorenz number and T is temperature. Note that the Lorenz number is both material and temperature dependent [87]. Its ideal value (Sommerfeld value) is 2.44×10^{-8} V^2K^{-2}. Sometimes a Seebeck coefficient can be included in Eq. (5.2) to capture the thermoelectric effects. However, the Seebeck coefficient is typically much smaller than the Lorenz number for metals [87] and therefore it is neglected in this work. The Wiedemann-Franz law shows that the electronic thermal conductivity can be estimated if the electrical conductivity is known.

According to the Drude theory, the electrical conductivity is proportional to the relaxation time (τ) of electrons during scattering processes, i.e., $\sigma \propto \tau$. In term of electrical resistivity ($\rho = 1/\sigma$), it is proportional to the reciprocal of the relaxation time, $\rho \propto \tau^{-1}$. In metals, electrons are scattered by three main processes [87, 88]: (a) electron scattering by static imperfections such as point defects and dislocations, (b) electron scattering by lattice vibrations (electron-phonon scattering), and (c) electron scattering by other electrons (electron-electron scattering). These scattering processes increase the electrical resistivity and therefore reduce the thermal conductivity. According to the Matthiessen's rule, these scattering processes are assumed to be independent to each other [87]. Therefore, the total relaxation time can be calculated from the reciprocal addition of each individual relaxation time. As a result, the total electrical resistivity is simply the sum of the individual resistivity induced by each scattering process,

$$\rho = \rho_{res} + \rho_{e-p} + \rho_{e-e}, \qquad (5.3)$$

where ρ_{res} is residual electrical resistivity due to the scattering process (a), ρ_{e-p} and ρ_{e-e} are resistivities induced by electron-phonon and electron-electron scattering, respectively. The sum of ρ_{e-p} and ρ_{e-e} is called intrinsic resistivity [88]. Sometimes an additional term is added to Eq. (5.3) to consider the deviation from the Matthiessen's rule [89].

The electrical resistivity resulted from the electron-phonon scattering process can be described by the Bloch-Gruneisen theory [87],

$$\rho_{e-p}(T) = A\left(\frac{T}{\theta_D}\right)J_5\left(\frac{\theta_D}{T}\right), \qquad (5.4)$$

where θ_D is the Debye temperature of the metal, coefficient A is a material-specific coefficient, and the function J_n is defined as,

$$J_n\left(\frac{\theta_D}{T}\right) = \int_0^{\theta_D/T} \frac{x^n e^x}{\left(e^x - 1\right)^2} dx \; . \qquad (5.5)$$

It has been shown that Eq. (5.4) gives very different temperature dependence on the e-p electrical resistivity at high temperatures (above Debye temperature) and at very low temperatures:

$$\rho_{e-p}(T) = \frac{A}{4}\left(\frac{T}{\theta_D}\right) \text{ for } T \geq \theta_D, \qquad (5.6)$$

$$\rho_{e-p}(T) = 124.4A\left(\frac{T}{\theta_D}\right)^5 \text{ for } T \ll \theta_D. \qquad (5.7)$$

For metallic fuels the thermal transport behavior at high temperatures is more relevant to their applications. Therefore, the *e-p* electrical resistivity should have a linear dependence on temperature according to Eq. (5.6) at high temperatures.

For the electron-electron scattering process, the electrical resistivity can be described as [90]:

$$\rho_{e-e}(T) = B \cdot T^2, \qquad (5.8)$$

where B is a material-related coefficient. Equation (5.8) shows that the electrical resistivity induced by the e-e scattering has a T^2 dependence, indicating that the *e-e* scattering may dominate at high temperatures.

Using the Wiedemann-Franz law (Eq. (5.2)), the thermal resistivity (i.e., $W_e = \frac{1}{k_e} = \frac{\rho}{LT}$) can be related to electrical resistivities due to different electron scattering,

$$W_e = \frac{\rho_{res}}{LT} + \frac{\rho_{e-p}}{LT} + \frac{\rho_{e-e}}{LT} \qquad (5.9)$$

Combining Eqs. (5.6), (5.8), (5.9), one can get the temperature dependence of electronic thermal resistivity of metals at high temperatures,

$$W_e = \frac{A_{res}}{T} + A_{e-p} + A_{e-e} \cdot T, \qquad (5.10)$$

where A_{res}, A_{e-p}, A_{e-e} are coefficients to be determined. The electronic thermal conductivity is simply the inverse of Eq. (5.10). Equation (5.10) is a simplified model for describing the temperature dependence of electronic thermal resistivity (or conductivity) for metals. It is derived from quantum mechanics theories with many approximations and assumptions. It may be used to describe the temperature dependence of thermal resistivity/conductivity for some simple monovalent alkali metals or noble metals that have nearly spherical Fermi surfaces [87]. In this work, the temperature-dependent thermal resistivities of pure U and Zr will be fitted to Eq. (5.10) to determine whether this simple model can be used to describe the thermal transport behavior of the two metals that have complex electronic structures.

5.2.2 Mixing rule for thermal conductivity of binary alloys

In a binary alloy, one type of alloying element can be considered as an impurity, which induces additional electron scattering effects on the thermal transport. Assuming α_A and α_B are the respective weight fractions of A and B components in a binary alloy, the relation $\alpha_A + \alpha_B = 1$ holds. The overall thermal resistivity can be described by the model [91],

$$W_{binary} = \alpha_A W_{e,A} + \alpha_B W_{e,B} + \rho_0/LT \ , \qquad (5.11)$$

where ρ_0 is the residual electrical resistivity induced by the alloying element. The physical meaning of Eq. (5.11) is that the total thermal resistivity of an alloy has a concentration-dependent contribution from each alloy component and an additional resistivity from the alloying effects. The shape of residual resistivity curve may be assumed as a symmetric function of concentration such as the Nordheim's rule [92],

$$\rho_0 = C\alpha_A\alpha_B \qquad (5.12)$$

where C is a material-dependent coefficient. Although this simple rule works well for Au-Ag system [93], it is not consistent with many binary systems such as Co-Pd [94]. Tsiovkin et al. [95, 96] have derived a more general formulation to describe the mixing effects on thermal resistivity in binary alloys. Zhang et al. [97] have adopted such an approach and developed a simplified equation for the U-Si binary system:

$$\rho_0 = \alpha_A\alpha_B\left(C_A + C_B\left(\alpha_B^2 - \alpha_A^2\right)\right). \qquad (5.13)$$

Here we use this simplified equation to describe the U-Zr system and rewrite Eq. (5.11) as,

$$W_{binary} = \alpha_A W_{e,A} + \alpha_B W_{e,B} + \alpha_A\alpha_B\big(C_A + C_B(\alpha_B^2 - \alpha_A^2)\big)/LT. \qquad (5.14)$$

In addition, the material related parameters of L_A and L_B are defined as,

$$\begin{aligned} L_A &= C_A / LT \\ L_B &= C_B / LT \end{aligned} . \qquad (5.15)$$

Therefore, the thermal resistivity of a binary alloy can be derived from a simple interpolation between the thermal resistivities of two pure metal components using the following equation,

$$W_{binary} = \alpha_A W_{e,A} + \alpha_B W_{e,B} + \alpha_A \alpha_B \left(L_A + L_B \left(\alpha_B^2 - \alpha_A^2 \right) \right). \quad (5.16)$$

Equation (5.16) shows that the richer component dominates the total thermal conductivities and the alloying element reduces the thermal conductivity.

5.3. Results

5.3.1. Thermal resistivity of pure U, Zr

For pure U, the experimentally measured thermal conductivity data at different temperatures are those summarized by Touloukian et al. [77] and measured by Takahashi et al. [78]. The thermal resistivities are therefore obtained by taking the inverse of these thermal conductivity data. In this work, Eq. (5.10) is used to fit to these experimental resistivities and the parameters are determined by least square fitting. The fitting yields,

$$W_U = \frac{1.67606}{T} + 0.0358 - 1.454 \times 10^{-5} T, \quad (5.17)$$

where W_U is the thermal resistivity of uranium and T is in the unit of Kevin. Given the availability of experimental data, the valid temperature range is $293 \leq T \leq 1173\ K$. The fitted curve and the experimental data are shown in Fig. 5.1(a). The fitted resistivity decreases almost linearly with temperature. The fitted equation (Eq. (5.17)) agrees well with both Touloukian's [77] and Takahashi's [78] data sets. The melting temperature of pure U is about 1406 K (1133 °C). Therefore, extrapolation to higher temperatures is possible if this nearly linear temperature dependence holds. Previously, Kim et al. [85] used a 2nd order polynomial function to fit to the same set of thermal conductivity data,

$$k_{U-Kim} = 21.73 + 1.591 \times 10^{-2} T + 5.907 \times 10^{-6} T^2. \quad (5.18)$$

The Bison-LANL model [86] adjusts the coefficients in Kim's model slightly,

$$k_{U-Bison} = 21.76 + 1.665 \times 10^{-2}T + 5.167 \times 10^{-6}T^2. \qquad (5.19)$$

The inverse curves of Eqs. (5.18) and (5.19) are also shown in Fig. 5.1(a) for comparison. They give nearly identical resistivities as our model. Fig. 5.1(b) shows the thermal conductivity comparison between predictions of the inverse of Eq. (5.17) of this report and previous models of Eqs. (5.18) and (5.19).

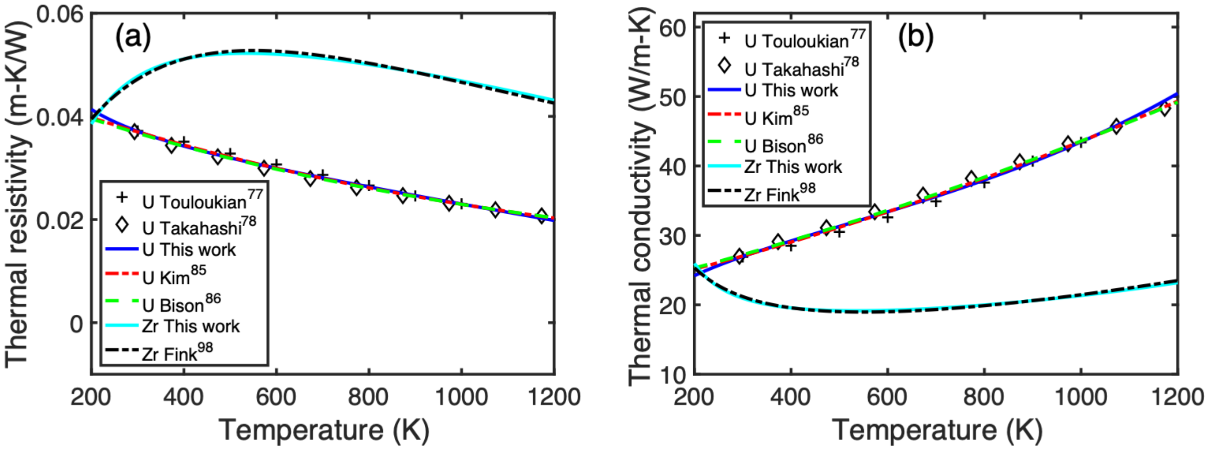

Fig. 5. 1. Fitted (a) thermal resistivities curve and (b) thermal conductivity of pure uranium and pure zirconium as a function of temperature. Previous fitted models [85, 86, 98] for pure U and pure Zr are also shown.

For pure Zr, the thermal conductivities at temperatures between 298 K to 2000 K have been measured by many researchers previously. However, the data are very scattered, as summarized by Fink and Leibowitz [98]. Based on a statistical analysis, Fink and Leibowitz [98] developed a polynomial function to describe the temperature dependence of Zr thermal conductivity,

$$k_{Zr} = 8.853 + 7.082 \times 10^{-3}T + 2.533 \times 10^{-6}T^2 + 2.992 \times 10^3 T^{-1}. \qquad (5.20)$$

The equation contains a 1/T temperature dependence term, which captures the temperature dependence of the electron-electron scattering effects (for thermal resistivity, the temperature dependence is thus $W_{e-e} \propto T$, as shown in Eq. (5.10)). It has been shown that Eq. (5.20) can be used to describe most of the Zr thermal conductivity data with an uncertainty of one standard deviation. In both Kim's [85] and Bison's model [86], Equation (5.20) is used to describe the temperature dependence of thermal conductivity of pure Zr.

In this work, Eq. (5.10) is used to fit to the inverse of Eq. (5.20) to obtain the temperature dependence of the thermal resistivity of pure Zr (W_{Zr}) in the temperature range of $293 \leq T \leq 1400K$. The least square fitting yields,

$$W_{Zr} = -\frac{7.0125}{T} + 0.0785 - 2.461 \times 10^{-5} T \quad . \qquad (5.21)$$

Equation (5.21) is plotted in Fig. 5.1. For comparison, Fink's model (inverse of Eq. (5.20)) is also shown in Fig. 5.1. The two fitting equations give nearly identical results. The thermal resistivity of pure Zr increases with temperature initially until it reaches a maximum value at about 400 K. Then the thermal resistivity decreases almost linearly with temperature. Fink et al. [98] argued that the maximum thermal resistance (or minimum thermal conductivity) is an outcome of the strong *e-e* scattering in Zr at the low temperature regime.

It can be seen that the thermal resistivities of both pure U and pure Zr can be well fitted to the simple analytical electronic thermal resistivity model (Eq. (5.10)). However, one also can notice that some coefficients in our fitted models (Eqs. (5.17) and (5.21)) have negative values, indicating that these fitting are more empirical rather than physical. This is not surprising because the simple electronic thermal resistivity model (Eq. (5.10)) is derived based on many assumptions such as that metals have a spherical Fermi surface, as mentioned earlier. U and Zr, however, have complex electronic structures. It has been argued [87] that thermal transport in metals is a very complex many-body quantum statistical problem so that such simple theories cannot describe the complex thermal transport behaviors in all metals. Therefore, it is a challenge to use such a simple model to determine the accurate contribution of each electronic scattering mechanism to the thermal conductivities of pure U and pure Zr. Nevertheless, our semi-empirical fitting gives good agreement with experimental results. Therefore, these fitted models will be used to interpolate the thermal conductivities of binary U-Zr alloys.

5.3.2. Thermal conductivity model for binary U-Zr alloys

The main temperature-dependent and composition-dependent thermal conductivity data of U-Zr binary alloys are those reported by Touloukian et al. [77] and Takahashi et al. [78]. These data sets have been frequently used to fit the thermal conductivity models for U-Zr alloys [85]. Touloukian et al. [77] collected the thermal conductivity data of both U-rich and Zr-rich U-Zr alloys as a function of temperature and Zr composition that were measured in 1950s. Unfortunately, there is no information about the sample porosities and uncertainties of the measurements. In 1988, Takahashi et al. [78] used the laser flash method to measure the thermal conductivities of a few U-Zr alloys of different compositions as a function of temperature. The porosities of the samples were not specified either. The uncertainties in thermal diffusivities were about 10% as indicated in the figure for the U-72at.%Zr. The compositions reported in Takahashi et al.'s work is in atomic percent, but they are converted to weight percent in our paper. In our model development, the experimental data collected by Touloukian et al. [77] (U-5Zr, U-20Zr, U-40Zr, U-70Zr, U-86Zr) and the data reported by Takahashi et al. [78] (U-5.87Zr, U-17Zr, U-49.6Zr, U-79.4Zr) are used to fit to our temperature- and composition-dependent thermal resistivity model (Eq. (5.16)), all in weight percent. In the fitting, no bias or weighting scheme is used for any temperature and composition ranges. In other words, all data are weighted equally. For very high content (nearly pure) U-rich and Zr-rich alloys such as U-1.5Zr and U-97Zr by Touloukian [77], the data are not included in the fitting procedure because their thermal conductivities deviate substantially from the pure metals, in particular the U-97Zr. However, their experimental values are compared with our model prediction in this report. The temperature range is $293 \leq T \leq 1273K$ for the data by Touloukian et al. [77] and $300 \leq T \leq 800K$ for the data by Takahashi et al. [78].

In addition to the data reported by Touloukian et al. [77] and Takahashi et al. [78], there are some other experimental thermal conductivity data of U-Zr alloys available in literature. Janney et al. collected some of these additional data in the recently published Metallic Fuels Handbook [82]. Scientists at Argonne National Laboratory (ANL) [80] measured the thermal conductivity of a U-11.4Zr between 600 K and 1200 K. A polynomial function was obtained by fitting to the data. The systematic errors were not apparent in this study and no sample porosity information was provided. Matsui et al. [79] estimated the temperature-dependent thermal conductivities of a U-9Zr (U-20at.%Zr) at different temperatures based on the experimentally measured heat capacities and thermal diffusitivies. Recently, Kaity et al. [81] measured the thermal conductivities of a U-6Zr alloy between 303.7 K and 920.6 K. In both work by Matsui et al. and Kaity et al., no information about the sample porosity and measurement uncertainties were provided. These additional experimental data [79-81] are not included in our fitting procedure, rather they are used as independent data to validate our model. Therefore, all the available data reported in literature (to our best knowledge) are compared in this paper. In our fitting, the first step is to take the inverse of the experimental thermal conductivities and convert them to thermal resistivities. Next an exponential decay function is used to describe the two parameters in Eq.

(5.16), L_U and L_{Zr}. Note this exponential decay function was used to fit the thermal conductivities of pure U and Si previously [97]. The exponential decay function has the form,

$$L = b_0 + b_1 \exp\left(-\frac{T - T_0}{T_1}\right) + b_2 \exp\left(-\frac{T - T_0}{T_2}\right), \qquad (5.22)$$

where b_0, b_1, b_2, T_0, T_1, and T_2 are parameters to be determined for L_U and L_{Zr}, respectively. Through a least square fitting procedure, these coefficients are obtained, as shown in Table 5.1.

Table 5. 1. Fitted parameters for L_U and L_{Zr}.

	b_0	b_1	b_2	T_0	T_1	T_2
L_U	-0.04622	7.647×10^{-5}	0.4018	349.738	677.422	412.642
L_{Zr}	-0.07028	-1.518×10^{-4}	0.1609	184.487	646.095	985.206

By replacing the L_U and L_{Zr} in Eq. (5.16) using Eq. (5.22) and Table 5.1, together with the thermal resistivities of pure U (Eq. (5.17)) and pure Zr (Eq. (5.21)), the thermal resistivity model for U-Zr alloys is developed. The model can predict the temperature-dependent thermal resistivities in the full composition range. The predicted thermal resistivities of U-rich alloys as a function of temperature are plotted as lines in Fig. 5.2(a) and those of Zr-rich alloys are shown in Fig. 5.2(b). The experimental data are also shown as symbols for comparison. For U-rich alloys (Fig. 5.2(a)), the model prediction has very good agreement with the experimental data, although minor discrepancies can be seen at low temperatures for the U-17Zr and U-20Zr alloys. For the Zr-rich alloys (Fig. 5.2(b)), the agreement is also reasonable although the discrepancies are larger. Since thermal resistivity is the inverse of thermal conductivity, the discrepancies are magnified in this plot. As shown in Fig. 5.3, our model predicts reasonable thermal conductivities for Zr-rich alloys.

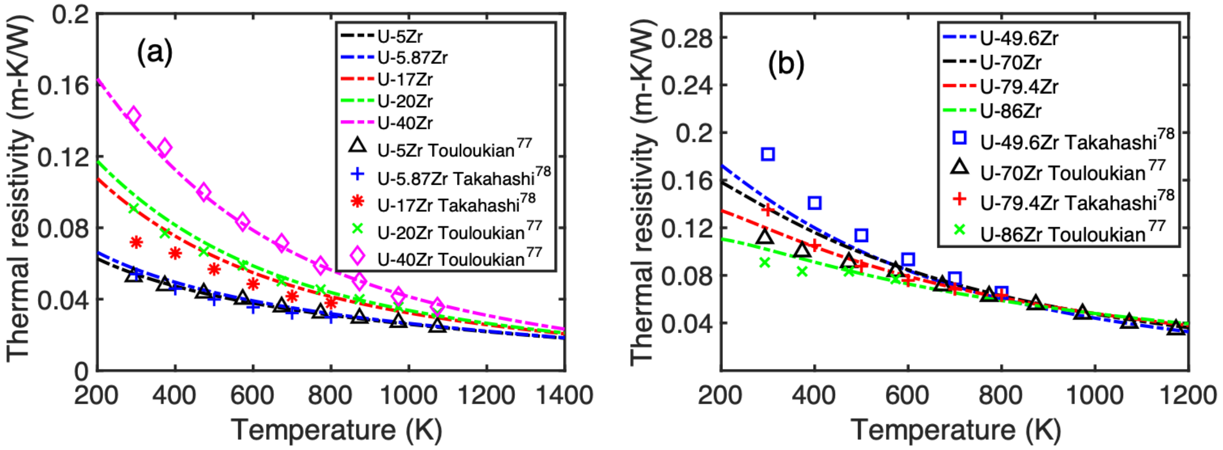

Fig. 5. 2. Temperature-dependent thermal resistivities of different U-Zr alloys. The lines are model predictions and the symbols are experimental data. The experimental data are taken from Touloukian et al. [77] and Takahashi et al. [78]. (a) U-rich alloys. (b) Zr-rich alloys.

The predicted thermal resistivities shown in Fig. 5.2(a) and Fig. 5.2(b) are converted to the temperature-dependent thermal conductivities, as shown in Fig. 5.3(a) and Fig. 5.3(b). It can be clearly seen that for U-rich alloy (Fig. 5.3(a)), the thermal conductivity increases monotonically with the increasing temperature for each composition. The temperature dependence behavior is similar to that of pure U shown in Fig. 5.1(b), indicating that U dominates the thermal transport behavior. For Zr-rich alloys (Fig. 5.3(b)), the thermal conductivity also increases monotonically with temperature for each composition. The temperature dependence in Zr-rich alloys is different from the pure Zr in which a minimum thermal conductivity value can be found at about 400 K.

The results suggest that even if Zr concentration is high, U still plays a dominant role in affecting the temperature dependence behavior of the thermal conductivity.

As for the composition dependence, in U-rich alloys (Fig. 5.3(a)) the thermal conductivity decreases with the increasing Zr concentration at any given temperature because pure U has a higher thermal conductivity than pure Zr (Fig. 5.1. (b)). However, in Zr-rich alloys (Fig. 5.3(b)), the trend is a little complex. The thermal conductivity typically increases with the increasing Zr weight fraction at the low temperature regime but decreases with the increasing Zr weight fraction at the high temperature regime. The crossover temperature is at about 850 K. We think that this may be a result of formation of δ-UZr_2 phase at low temperatures in Zr-rich alloys. For example, the atomic fractions of Zr is 72 at.% in the U-49.6Zr alloy. According to the U-Zr phase diagram [26], the U-49.6Zr (U-72 at.%Zr) alloy should form the δ-UZr_2 phase below 873 K. In other Zr-rich alloys, the δ+α-Zr phase should form at low temperatures. Therefore, it is expected that the δ phase has a lower thermal conductivity than other phases. Similar argument was also made by Takahashi et al. [78]. Above 873 K, the δ-UZr_2 phase transforms to a BCC γ U-Zr solid solution. Therefore, the Zr composition dependence of thermal conductivity is expected to follow the normal trend, i.e., thermal conductivity decreases with the increasing Zr concentration. Our model indeed predicts a crossover temperature around 850 K and above which the thermal conductivity of U-49.6Zr is higher than other alloys, as can be seen in Fig. 5.3(b).

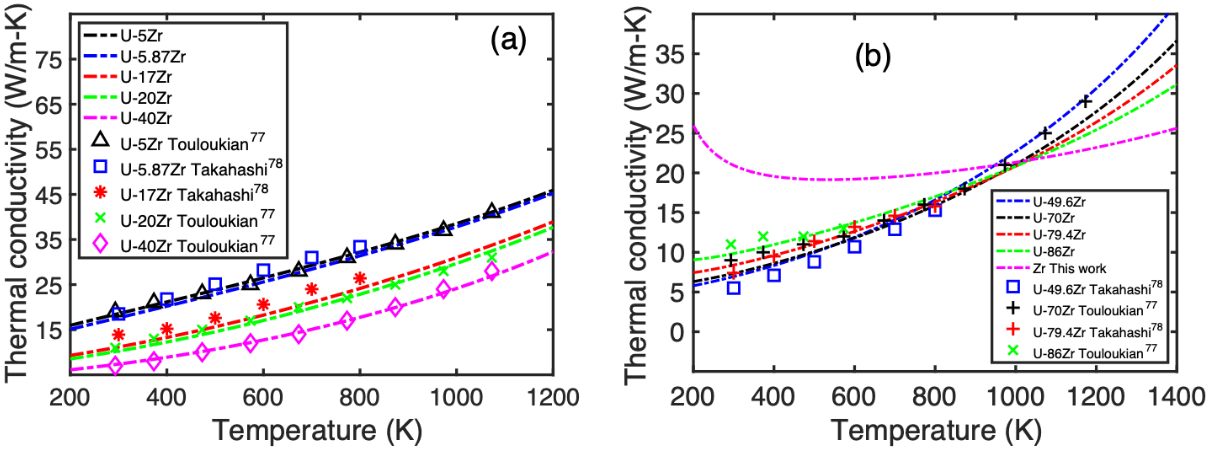

Fig. 5. 3. Temperature-dependent thermal conductivities of different U-Zr alloys. The lines are our model predictions and the symbols are experimental data. The experimental data are taken from Touloukian et al. [77] and Takahashi et al. [78]. (a) U-rich alloys. (b) Zr-rich alloys.

5.3.3. Model predictions and comparison with previous models

As mentioned earlier, several thermal conductivity models for U-Zr alloys have been developed previously [83-86]. Kim et al. [85] compared some previous models with their newly developed model and demonstrated that their model gives much better predictions in thermal conductivity for a wide range of temperatures and compositions. Recently, scientists at Los Alamos National Laboratory have adjusted the parameters in Kim's model and the improved model [86] has been implemented in Bison (termed as Bison's model in this paper). In both Kim et al. and Bison's model [85, 86], polynomial functions were used to describe thermal conductivities of pure metals. For alloys, an empirical mixing rule is used and the factor that accounts for the alloying effects was determined by another polynomial fitting. Here comparisons between Kim's model, Bison's model, and our model are shown as follows.

Regarding Touloukian's experimental data [77] (U-5Zr, U-20Zr, U-40Zr and U-70Zr), the comparison of the three models is shown in Fig. 5.4. It can be seen that Kim's model and Bison's model predict very similar values. For the U-5Zr alloy shown in Fig. 5.4(a), our model predicts almost identical thermal conductivities as Touloukian's recommended values, while Kim's model and Bison's model overpredict the thermal conductivities below 1000 K. For U-20Zr alloy (Fig. 5.4(b)), our model predicts similar results as the other two models, although our model has slightly larger discrepancies. For U-40Zr (Fig. 5.4(c)), our model predicts very good results over all temperatures, while the other two models result in slightly larger discrepancies. For the U-70Zr alloy (Fig. 5.4(d)), Kim's model and Bison's model have better agreement with experimental data than our model. However, at low temperatures, the other two models yield Zr-like temperature dependence behavior, i.e., a minimum value in thermal conductivity appears. In contrast, our model predicts that the thermal conductivity decreases monotonically with the decreasing temperature, which is consistent with the experimental trend in this alloy and other Zr-rich alloys (shown below).

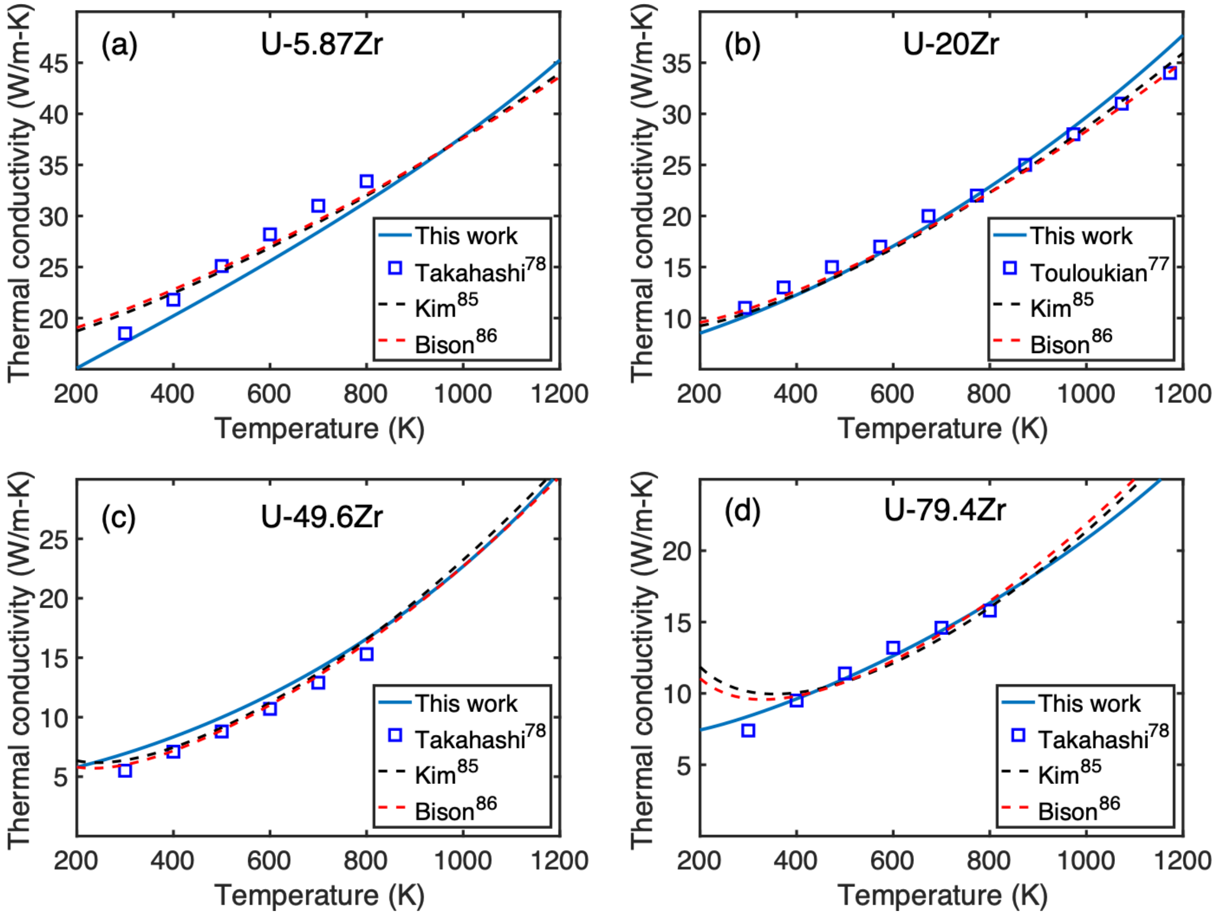

Fig. 5. 4. Comparison of the model predictions with the experimental data by Touloukian [77]. Kim's model (dashed black line), Bison's model (dashed red line) and our model (solid blue line) are shown in all figures. The experimental data are represented by symbols. (a) U-5Zr. (b) U-20Zr. (c) U-40Zr. (d) U-70Zr.

Regarding Takahashi's [78] data (U-6Zr, U-17Zr, U-49.6Zr and U-79.4Zr), the comparison of three models is shown in Fig. 5.5. For the U-5.87Zr (Fig. 5.5(a)), the other two models predict better results than our model, while our model gives better temperature-dependence (slope) for the thermal conductivity. For the U-17Zr (Fig. 5.5(b)), the other two models are slightly better than our model at low temperatures. However, all models underpredict the results. For the U-49.6Zr

(Fig. 5.5(c)), the other two models have very good agreement with Takahashi's experimental data, while our model overpredicts the thermal conductivity slightly. For the U-79.4Zr alloy (Fig. 5.5(d)), the other two models have larger deviations from the experimental values than our model at low temperatures because they predict Zr-like minimum thermal conductivities. As compared to the results in the U-70Zr alloy (Fig. 5.4(d)) and U-79.4Zr alloy (Fig. 5.5(d)), it is clear that this Zr-like temperature dependence behavior becomes more pronounced as Zr concentration increases in Kim's and Bison's models. However, this Zr-like behavior does not appear in the available experimental data, even if Zr has a very high content such as U-79.4Zr (Fig. 5.5(d)).

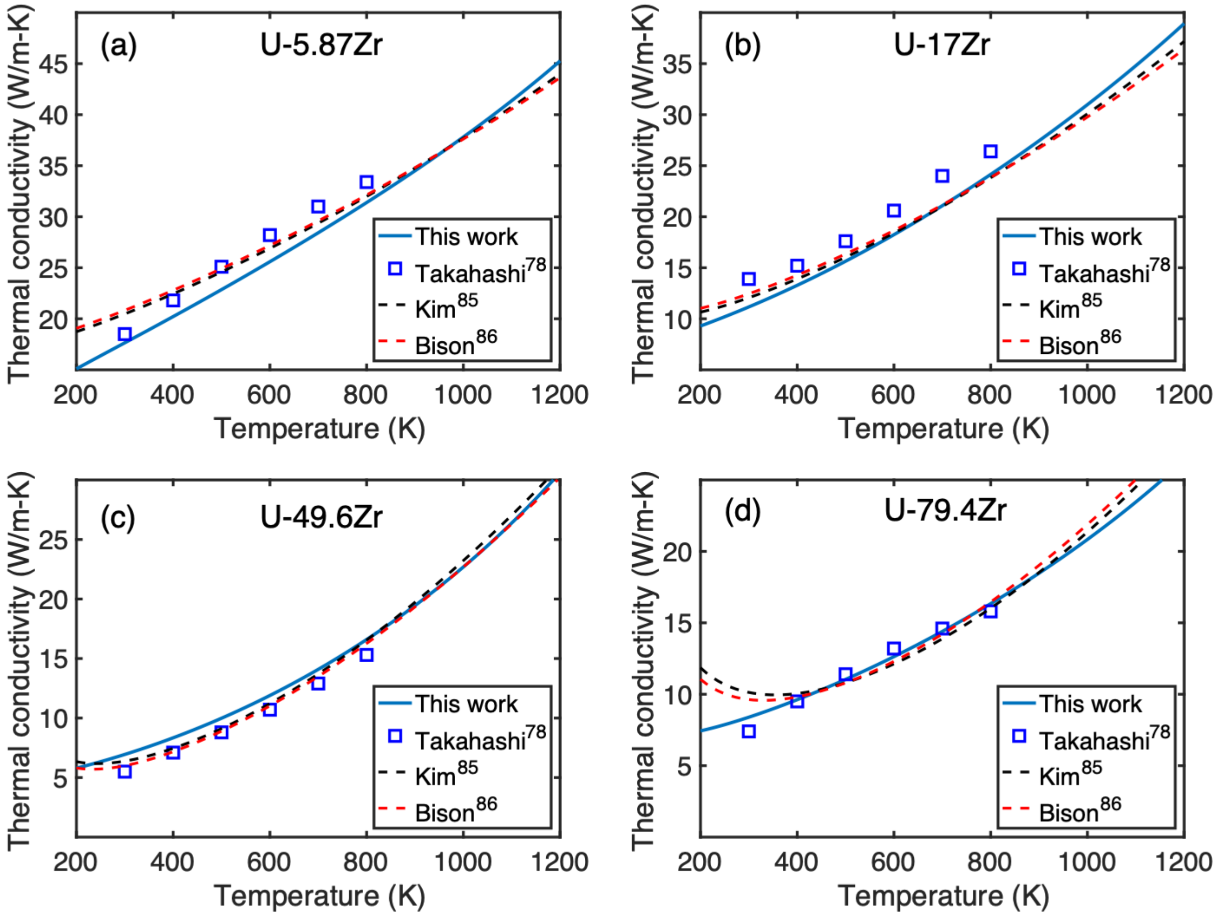

Fig. 5. 5. Comparison of the model predictions with the experimental data by Takahashi [78]. Kim's model (dashed black line), Bison's model (dashed red line) and our model (solid blue line)

are shown in all figures. The experimental data are represented by symbols. (a) U-5.87Zr. (b) U-17Zr. (c) U-49.6Zr. (d) U-79.4Zr.

For U-Zr alloys with very high (nearly pure) Zr content, the comparisons of the three models are shown in Fig. 5.6. Our model agrees well with the experimental data for the U-86Zr (U-94at.%Zr) alloy (Fig. 5.6(a)), and there is still no minimum value for this composition. Kim's and Bison's models also have good agreement with the experimental data although a minimum value appears. However, we admit that the limited number of experimental data points may not be sufficient to validate our model for this composition. For the U-97Zr (U-98.83at.%Zr) alloy (Fig. 5.6(b)) which is not included in our model fitting, our model predicts that the thermal conductivities are in the middle between the experimental data of U-97Zr by Touloukian [77] and pure Zr data by Fink [98]. On the other hand, Kim's and Bison's models have better agreement because this composition is included in their modeling fitting. The discrepancies between our model and experimental data indicate that our model may need further improvement. It is also possible that the impurity or porosity induced uncertainty in experiments is large for such a high-Zr alloy because the thermal conductivities of U-97Zr decrease substantially from that of the pure Zr. Unfortunately, no such information is available for this data set.

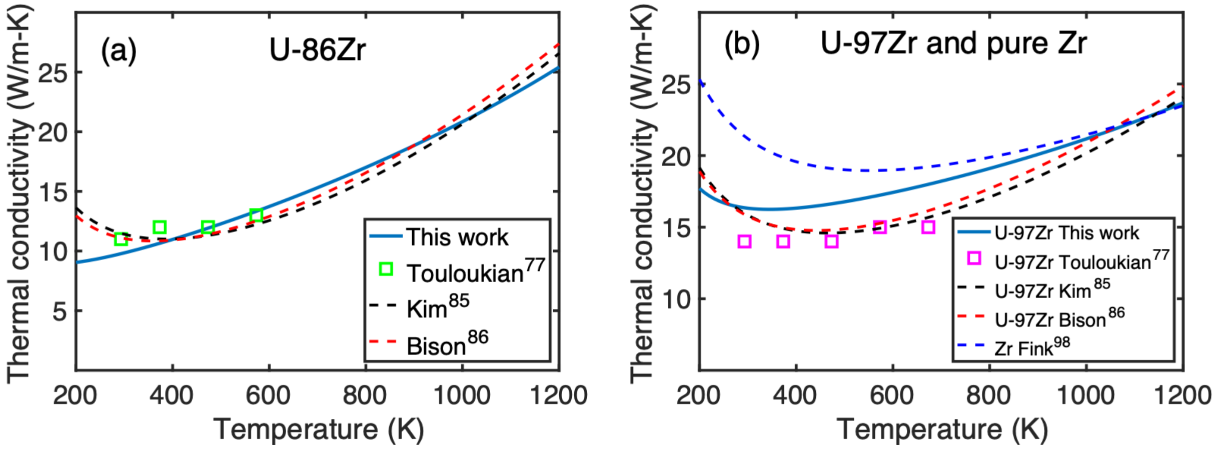

Fig. 5. 6. Comparison of model predictions with experimental data for two U-Zr alloys with nearly pure Zr content. Kim's model (dashed black line), Bison's model (dashed red line) and our model (solid blue line) are shown in all figures. The experimental data for the two alloys are shown as symbols. (a) U-86Zr (U-94at.%Zr). (b) U-97Zr (U-98.83at.%Zr). The thermal conductivity curve of pure Zr (blue dashed line) is also shown. Note that the U-97Zr data were included as fitting data in Kim's model but not in our model.

Next the model predictions are compared with the data that are not included in the model fitting. The comparison with such independent data may be considered as a way of model validation. In addition to the U-97Zr discussed above (Fig. 5.6(b)), the thermal conductivity data for the U-1.5Zr alloy by Touloukian [77] are not used in our model fitting. As can be seen in Fig. 5.7(a), although our model prediction deviates slightly from the experimental data, overall our model has slightly better predictions than Kim's and Bison's models, although this data set was included in Kim's model fitting.

Recently, Kaity et al. [81] measured the temperature-dependent thermal conductivity for a U-6Zr alloy and the data is not included in our model fitting. The comparison between model predictions and this data set is shown in Fig. 5.7(b). The U-5.87Zr (can be approximated as U-6Zr) data by Takahashi [78] is also shown for comparison. Clearly, Kaity's results (solid green line) are higher than Takahashi's data at temperatures below 600 K. The large discrepancies between two experimental data sets indicate that the uncertainties in experiments can be large as well. Our model underpredicts the thermal conductivities for both data sets while Kim's and Bison's models have better agreement.

Matsui et al. [79] measured the temperature-dependent thermal conductivities for a U-9Zr (or U-20at.%Zr) alloy and ANL [80] measured the thermal conductivities for a U-11.4Zr alloy. These data sets are not included in our model fitting. The comparison between the model predictions and these data is made, as shown in Fig. 5.7(c). Our model has good agreement with Matsui's U-9Zr data at the full temperature range, while the other two models overpredict the results. For ANL's U-11.4Zr data (extracted from the fitted polynomial function in Ref. [80]), our model overpredicts the results at high temperatures, while Kim's model agrees well with this data set [82]. It should be noted that two experimental data sets measured by two different groups overlap, even though they have different compositions. Moreover, the U-11.4Zr thermal conductivities are even slightly higher than the U-9Zr data, which is opposite to the correct composition dependence behavior.

The comparison between the model predictions and the data of U-29Zr by Takahashi [78] is shown in Fig. 5.7(d). Neither our model nor Kim's model includes this data set for model fitting. Clearly, all models overpredict the results. Our model predicts similar results as the other two models. Overall, our model and the other two models can predict reasonable thermal conductivities for the compositions not included in the fitting.

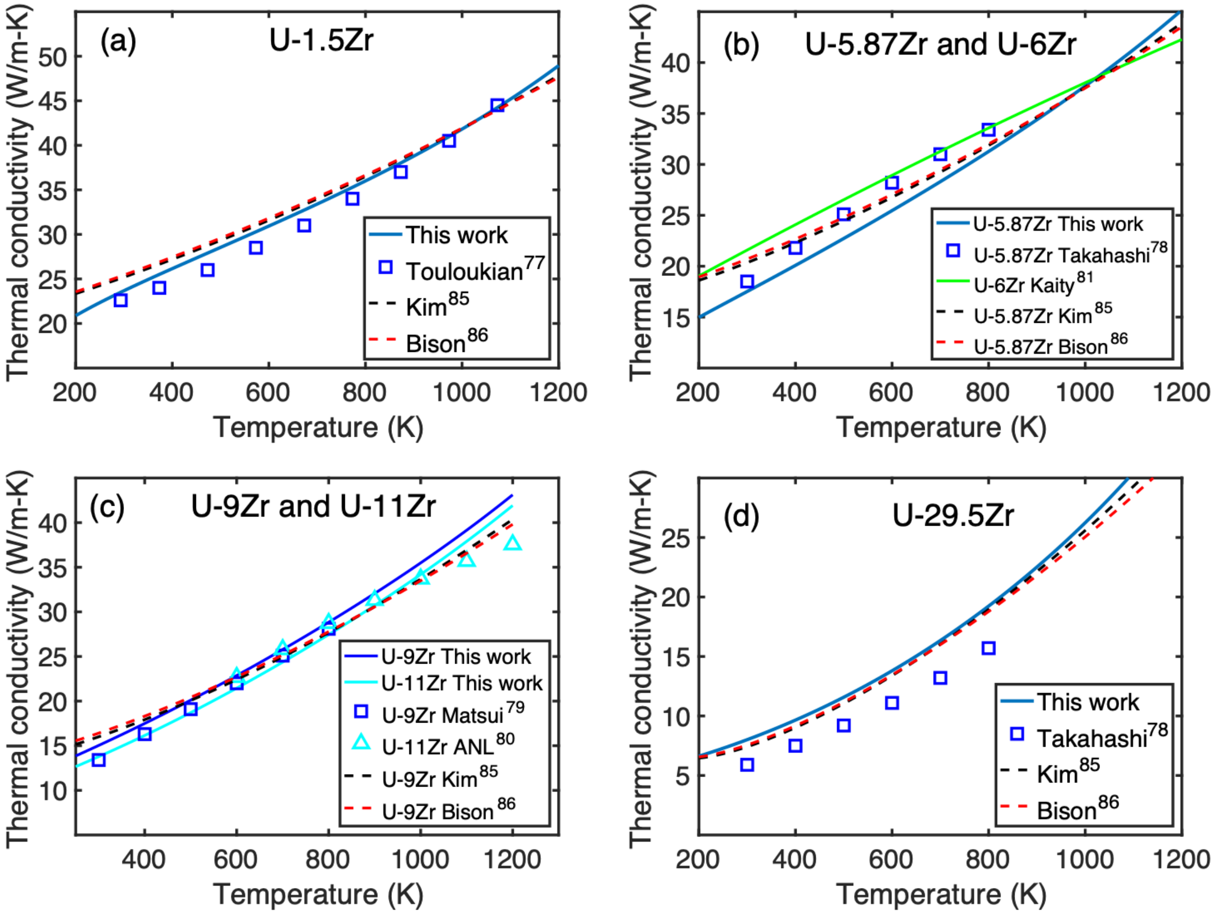

Fig. 5. 7. Model predictions for the data sets that are not included in our model fitting. Kim's model (dashed black line), Bison's model (dashed red line), our model (solid blue line), and experimental data (symbols) are shown in each figure. (a) U-1.5Zr by Touloukian [77]. (b) U-6Zr by Kaity (solid green line) [81]. The U-5.87Zr data by Takahashi [78] are also shown for comparison. (c) U-9Zr by Matsui [79] and U-11.4Zr by ANL [80]. (d) U-29Zr by Takahashi [78].

A comprehensive comparison between our new model and Bison's model can be found in Fig. 5.8, which shows how the model predictions deviate from the experimental data (the solid line). Since Bison's model is an improved version of Kim's model, here only Bison's model is compared. The U-97Zr data by Touloukian [77] and the U-6Zr by Kaity [81] are not included in this figure because their possible large experimental uncertainties. All other experimental data discussed in this work are included in this figure. Overall, both models result in very good agreement with the experimental data. Bison's model has slightly more scattered data points than our model. The root mean square errors (RMSE) between the model predictions and experimental data are also calculated for all the experimental data sets (except for U-97Zr). Three scenarios are considered: (a) If only the data by Touloukian [77] and Takahashi [78] are used, which are widely used for model fitting, the RMSE is 1.31 $W/(m \cdot K)$ for our model and 1.42 $W/(m \cdot K)$ for Bison's model; (b) If the data by Matsui [79] and ANL [80] are further included in addition to (a), the RMSE is 1.37 and 1.55 $W/(m \cdot K)$ for our model and Bison's model, respectively; (c) If the data by Kaity [81] are included in addition to (b), the RMSE is 1.61 and 1.55 $W/(m \cdot K)$ for our model and Bison's model, respectively. Overall our model gives slightly better predictions for most of the data sets. Since the errors or uncertainty information was not provided for most of the experimental data, we simply assume that the experimental error is ±1 $W/(m \cdot K)$ for all the experimental data. In Fig. 5.8, the two dashed lines indicate this assumed uncertainty. It can be seen that most of our model predictions are within this uncertainly range. Some deviated data points can be seen at the intermediate thermal conductivity range, but the magnitudes are small.

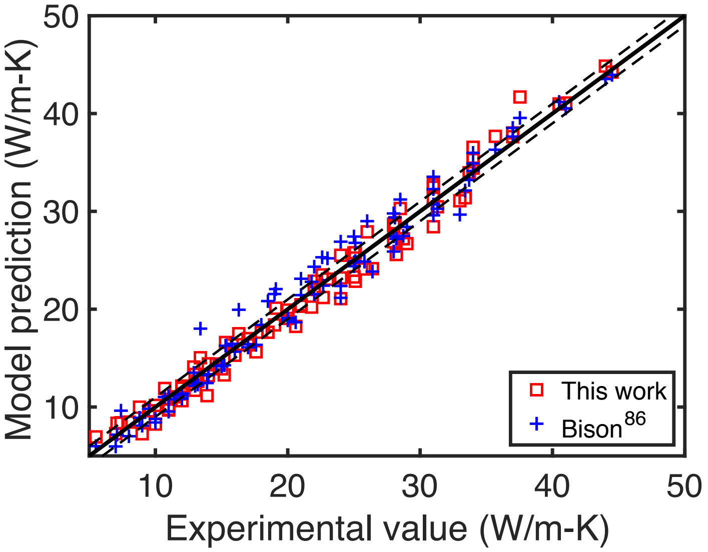

Fig. 5. 8. A comprehensive comparison of model predictions against the experimental data. The model predictions by our model and Bison's model are both shown. The solid line indicates the perfect fit. The two dashed lines indicate ±1 $W/(m \cdot K)$ *uncertainty.*

5.4. Discussions and conclusions

In this chapter, a new semi-empirical model is developed to predict the thermal conductivities of U-Zr alloys for the whole composition range and a wide range of temperatures. A new mixing rule is proposed to interpolate the thermal resistivities (and thus conductivities) between pure U and pure Zr to get the effective resistivities for U-Zr alloys of different compositions. The model is based on the assumption that free electrons are the main carriers for the thermal transport in both pure metals and alloys. Different from previous models that use polynomial functions to describe the thermal conductivities of pure U and Zr metals, our model attempts to use electrical resistivities to calculate thermal resistivities. The model considers three independent electron scattering effects on electrical resistivity: electron-defect scattering, electron-phonon scattering, and electron-electron scattering. The Wiedemann-Franz law is used to correlate the electrical resistivities to thermal resistivities. Although the thermal resistivity model is science-based (but very simplified), the obtained parameters are rather empirical, indicating that such a simple science-based model is not sufficient to capture the complex effects in pure metals and U-Zr alloys. To predict the thermal conductivities of U-Zr alloys, the alloying effects on the thermal resistivity are described by an exponential decay function in the new mixing rule model. Some of the experimental thermal conductivity data collected by Touloukian et al. [77] and measured by Takahashi et al. [78] are used to parameterize the model. The calibrated model is compared with a wide range of experimental data reported by different groups. To our best knowledge, all the available experimental data of U-Zr alloys are assessed in our work. The assessment shows that the thermal conductivities predicted by our model are in good agreement with most of experimental data. In comparison with the previous Kim's and Bison's models [85, 86], our model shows further improvement for some compositions, especially for low-Zr (e.g., U-1.5Zr, U-5Zr, U-9Zr) and high-Zr (e.g., U-79.4Zr) alloys. The ability of predicting good results for low-Zr alloys is important because it is relevant to the realistic fuel compositions (e.g., U-9Zr). For alloys with high Zr compositions, our model shows that the temperature dependence behavior is still dominated by U rather than Zr. This prediction is consistent with the experimental data that no minimum thermal conductivity is observed in high-Zr alloys.

The current model is based on the implicit assumption that U-Zr alloys form solid solutions. In reality, the alloys contain many phases and complex microstructures. To model the thermal conductivities in such heterogeneous systems, a microstructure-based approach may be used, which has been applied to model the effective thermal conductivities in a UO_2 system containing various microstructures [22]. The thermal conductivity model developed in this work can be used as input for the thermal conductivities of individual phases of different compositions. The model may also be coupled with constitute redistribution models and gas swelling models to conduct the fuel performance modeling. The model developed in this work is for unirradiated U-Zr alloys. In reactors, the thermal conductivity of U-Zr fuels can be further affected by radiation but such effects are not well understood for metallic fuels. Therefore, more theoretical and experimental work is needed in the future to understand the radiation effects on the thermal transport in metallic fuels.

Chapter 6: Mesoscale modeling of microstructure-dependent thermal conductivities of unirradiated U-Zr fuels

The work present in this chapter is planned to submit to a peer-review journal.

6.1 Introduction

In our previous work, we have successfully developed a composition- and temperature-dependent thermal conductivity model for U-Zr alloys [99], which is calibrated using some experimentally measured thermal conductivity data [77, 78]. This model can accurately predict the average thermal conductivity of an unirradiated fuel if the nominal composition and the temperature are known. However, this model neglects the microstructural information. In this chapter, the main focus is the U-rich U-Zr system, in which the predominant microstructure is α-U + δ-UZr_2 laminar structure when the temperature is below the γ-phase transition temperature. There are experimental measurements for thermal conductivities of pure α-U [77, 78]. And the temperature-dependent thermal conductivity for pure α-U also has been well-predicted by our recently developed thermal conductivity model [99] as well as in Chapter 5. For δ-UZr_2, however, there are only limited experimental data exist until very recently in 2020 and 2021. Ding et al. have measured the thermal conductivity of UZr_2 at temperature from 1.8 to 300K [100]. Hua et al. have measured the thermal conductivity for U-50wt.%Zr at 300K [101]. Both experimental data at 300K for the UZr_2 composition are only slightly lower than our model prediction [99]. This is reasonable since δ-UZr_2 has a wide compositional or stoichiometric range so that there are uncertainties in determining its composition. According to the U-Zr phase diagram (Fig. 2.2), the weight percentage of Zr in δ-UZr_2 varies significantly [102], roughly ranges from 40% to 60% (in weight percentage). Due to the lack of experimental data for δ-UZr_2 at temperatures above 300K, we use our thermal conductivity model [99] to predict its thermal conductivity at full temperature range for δ-UZr_2 (Note that all the δ-UZr_2 in the following context has the ideal composition at U-43.4Zr). In addition, there are other analytical models to estimate the average U-Zr thermal conductivity [85, 86]. Among those models [85, 86, 99], our U-Zr thermal conductivity model gives the relatively smaller errors when compared to experiment measurements. Therefore, we use our U-Zr thermal conductivity model [99] as references in this work.

If the temperature-dependent thermal conductivities of α-U and δ-UZr_2 are known, as well as if the volume fraction of each individual phase can be estimated from the phase diagram, one can estimate the effective thermal conductivity of a U-Zr system with a heterogeneous microstructure such as α-U + δ-UZr_2 laminar structure. There have been early models developed to estimate the effective thermal conductivities of heterogeneous systems containing heterogeneous microstructures [103, 104]. In 1980s, Hasselman and Johnson [105] pointed out that the thermal conductivity of composites should have nonzero interfacial thermal resistance (Kapitza resistance [106]), and they derived a new analytical model based on the original Maxwell model [103]. An interface between two phases or grains can act as a heat conduction barrier and has a strong phonon scattering effect to reduce the overall thermal conductivity. For polycrystals, microstructures with different grain sizes may result in different thermal conductivities even though they have the same composition. Therefore, in order to accurately estimate the effective thermal conductivity of a U-Zr heterogeneous microstructure, understanding the Kapitza resistance for a particular system is of great interest.

Our focus in this chapter is to quantify the interphase Kapitza resistance as well as to predict the effective thermal conductivity of U-rich U-Zr heterogeneous microstructures. Previously, C.W. Nan [107, 108] has developed an effective thermal conductivity model for polycrystals, which utilizes effective medium approach combining the factor of Kapitza resistance R to calculate effective thermal conductivities. Nan's model accounts for Kapitza resistance, grain size, grain shape and geometry effects. His model has been used and validated by B. He et al. [109] in calculating the effective thermal conductivity for two-phase polymer-matrix material. In addition to Nan's model, F. Badry and K. Ahmed [110] have estimated the interface thickness effect on Kapitza resistance. By adding the interface thickness effect, the overall error for the predicted effective thermal conductivity has been significantly reduced. However, as suggested [106], the Kapitza resistance is also showing strong temperature dependence. Current models [107, 108, 110] did not directly quantify the temperature effect as well as the geometry effect on the Kapitza resistance. Instead, they were only used to calculate the reduction of the effective thermal conductivities as functions of those factors to indirectly show how those factors affect the Kapitza resistance. Therefore, it is imperative to develop a comprehensive Kapitza resistance model that directly quantifies the temperature effect as well as the geometry effect (e.g., aspect ratio). If successful, such a model can be applied to predict the effective thermal conductivities more accurately.

For estimating the Kapitza resistance, the mesoscale phase field module in the MOOSE (Multiphysics Object-Oriented Simulation Environment) framework [111] is used, which is an open-source partial differential equation solver based on the finite element method (FEM). MOOSE is also capable of generating the desired microstructures for this work. In the phase field modeling, we treated the phase boundary as an additional 'phase' with a finite width. The detailed calculation approach is discussed in Chapter 6.2 and Chapter 6.3. Using MOOSE, we have calculated the Kapitza resistances at different temperatures and different spatial variations between the two phases. The calculated values are used to develop an analytical model to capture the effects of both the temperature and the spatial variation on the Kapitza resistance. The new Kapitza resistance model is able to overcome the shortcomings of the previous effective thermal conductivity models mentioned above. Coupling this Kapitza resistance model with the mesoscale modeling in the MOOSE framework, we accurately predicted the effective thermal conductivities of many different microstructures at a wide range of temperatures in a heterogeneous U-Zr system.

6.2 Simulation methods

6.2.1 MOOSE framework and AEH method

The mesoscale phase field module in the MOOSE framework [111] coupled with the heat conduction module is used to calculate the effective thermal conductivity of different heterogeneous microstructures consisting of α-U and δ-UZr_2 phases. The phase field method is used to relax the continuous interface between α-U and δ-UZr_2 phases. The heat conduction module is used to impose a thermal gradient to the heterogeneous system so that the effective thermal conductivity can be calculated through Fourier's law. This is a direct method for calculating the effective thermal conductivity. However, practically this direct method may induce some artifacts in the mesoscale modeling. For example, as is pointed out by JD. Hales et al. [112], if some microstructural features are located at the boundary of the simulation box, the effective thermal conductivity calculated by MOOSE using the direct method may not be accurate. On the other hand, the asymptotic expansion homogenization (AEH) method [113, 114] can be used to solve such problems. The AEH method is capable of calculating the nonlinear properties through coupling the microscopic properties at different length scales and passing them to a homogenized property over a periodic domain. In this work, the AEH method is used to calculate the effective thermal conductivities of heterogeneous microstructures in the U-Zr system. The overall effective thermal conductivity is obtained by averaging the thermal conductivities in both x and y directions in our 2-D simulation domains.

Typically, in phase field simulations, a finer mesh may give a more accurate result. However, as is suggested by J.D. Hales et al. [112], the AEH method does not necessarily require a very fine mesh, which could improve the computational efficiency. In this work, we constructed a 1 × 1 μm 2-D simulation domain with 100 meshes in each direction in MOOSE. We constructed ordered lamellar δ-UZr_2 in an α-U matrix with varying Zr weight fractions. A representative microstructure model is shown in Fig. 6.1. The Zr weight fraction varies from 5.63~13.44 wt.% (corresponding to 20~45% volume fraction of δ-UZr_2). The lamellar δ-UZr_2 structures are constructed with aspect ratio ranging from 5.4 to 12.15. The width of the interphase boundary is set to be 2.5 nm for α-U/δ-UZr_2 interface. The simulation temperature ranges between 300K to 800K, which is below the phase transition temperature of δ-UZr_2 to γ.

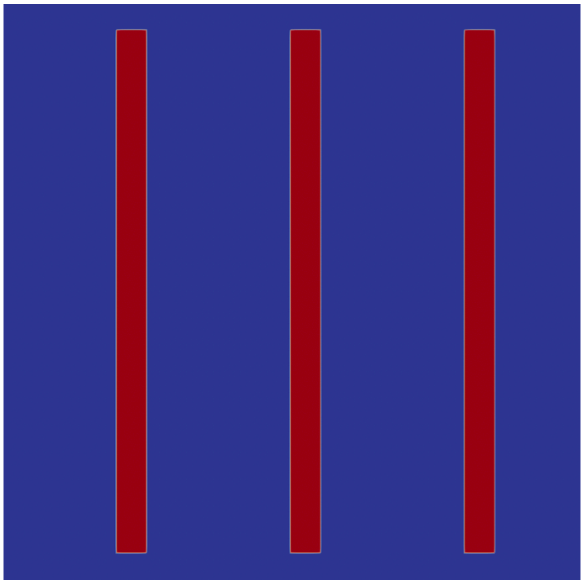

Fig. 6. 1. Constructed microstructure in MOOSE with lamellar δ-UZr₂ phase structure embedded in an α-U matrix. Red: δ-UZr₂; Blue: α-U. White: δ-UZr₂/ α-U interface

6.2.2 3D-2D thermal conductivity conversion

All the experimental data and some thermal conductivity models [85, 99] for metallic fuels are in 3D representation. However, in this work, the phase field simulations in MOOSE were performed in 2D. Therefore, the 2D thermal conductivity results calculated from MOOSE should be converted to 3D to compare with the experimental data. K. Bakker [115] has developed an analytical solution for the 2D to 3D thermal conductivity conversion for irradiated UO_2 based on finite element modeling. Recently, M.C. Teague et al. [116] using the phase field approach to calculate the 2D and 3D thermal conductivities of MOX fuels. They validated the 2D-3D conversion algorithm by comparing converted 2D-3D results through the analytical model with the 3D phase field modeling results. The analytical equation is expressed as follows:

$$(1-(1-k_d/k_m)\emptyset_d - f_{2D}) = r(1-(1-k_d/k_m)\emptyset_d - f_{3D}) \quad (k_d < k_m), \qquad (6.1)$$

$$r = 0.93 + \frac{1}{k_d/k_m + 1.03} \quad (k_d < k_m), \qquad (6.2)$$

where k_d and k_m are the thermal conductivities for the second phase and the matrix, respectively; $\emptyset_d$ is the volume fraction of the second phase; f_{2D} and f_{3D} are the fractions of the thermal conductivity with the precipitate divided by the thermal conductivity of the material without the second phase for the 2D and 3D systems, respectively. Note that Eq. (6.1) and Eq. (6.2) are valid only if $k_m > k_d$.

6.2.3 Kapitza resistance and effective thermal conductivity calculation

The calculation in MOOSE includes 3 steps. At first, we did not assign the Kapitza resistance in the calculation, only with the thermal conductivities of α-U and δ-UZr_2 being the input parameters. And we compared the effective thermal conductivities calculated by MOOSE with Maxwell model [103], Bruggeman model [104] and Hasselman-Johnson model [105]. These models are briefly discussed as follows. The Maxwell model can be described as

$$k_{eff}^{Max} = 1 + \frac{3\emptyset_d}{\left(\frac{k_d+2k_m}{k_d-k_m}\right)-\emptyset_d}, \qquad (6.3)$$

where k_m and k_d are the thermal conductivity for the α-U matrix and δ-UZr_2 phase respectively, ϕ_d is the volume fraction for δ-UZr_2. The Bruggeman model is described as follows

$$k_{eff}^{Bru} = \frac{1}{4}\left\{A + (A^2 + 8k_m k_d)^{\frac{1}{2}}\right\}, \qquad (6.4)$$

$$A = (3\phi_m - 1)k_m + (3\phi_d - 1)k_d, \qquad (6.5)$$

where ϕ_m is the volume fraction for the matrix and all the other parameters have the same meaning as Eq. (6.3).

These above models are widely used for simple composites and porous materials. However, these models neglect the interphase Kapitza resistance. Therefore, the Hasselman-Johnson (H-J) model has been developed to calculate the effective thermal conductivity by considering the effect of interphase thickness (a) and phase boundary thermal conductivity k_{int}, which can be expressed as:

$$k_{eff}^{H-J} = \frac{k_d}{\left(1-\frac{k_d}{k_m}+\frac{2k_d}{ak_{int}}\right)\phi_d+\frac{k_d}{k_m}}. \qquad (6.6)$$

Next, we used the α-U and δ-UZr_2 thermal conductivities as the input parameters, and the local phase boundary thermal conductivity as a fitting parameter in the MOOSE simulation. The interphase Kapitza resistance R can be calculated from phase boundary thermal conductivity as:

$$R = d/k_{int}, \qquad (6.7)$$

where d is the interface thickness, k_{int} is local thermal conductivity of the interphase boundary. The overall effective thermal conductivities calculated from MOOSE were fitted to the values predicted by our U-Zr thermal conductivity model [99] based on the nominal composition. Therefore, the Kapitza resistance for α-U/δ-UZr_2 phase boundary can be estimated. The fitting procedure is described as follows:

We revisited the general expression for Kapitza resistance at all temperatures derived by A. Khater and J. Szeftel [117], which has the form:

$$RT^3 = \frac{\beta^3(1+8\beta^{-1})^{-1}}{2\varepsilon Cd}\frac{1}{2\Theta_h^2+T\Theta_h\partial\Theta_h/\partial T}, \qquad (6.8)$$

where R is the Kapitza resistance, β is a statistical term, ε is the flatness of the interface, d is the atomic layer thickness, Θ_h is the Debye temperature, C is a material related parameter and $\partial\Theta_h/\partial T$ is the variation of Debye temperature as a function of temperature. It has been calculated that below the Debye temperature, $\partial\Theta_h/\partial T$ is zero and the Kapitza resistance has a clear T^3-dependence [106, 117-120]. For temperatures above Debye temperature, $\partial\Theta_h/\partial T$ is nonzero and the value of RT^3 is typically lower. However, for the U-Zr system, the $\partial\Theta_h/\partial T$ for α-U has been calculated by Ren et al. [121] at temperatures between 0-900K using the Quasi-harmonic Debye model [122] to be negligible. Therefore, for the heterogeneous U-Zr system in this work, we assumed that $\partial\Theta_h/\partial T$ is zero and Eq. (6.8) can be re-written as:

$$R_kT^3 = \frac{\beta^3(1+8\beta^{-1})^{-1}}{2\varepsilon Cd}\frac{1}{2\Theta_h^2}, \qquad (6.9)$$

In this case, the Kapitza resistance has a T^3-dependence at all temperatures in this work. Since all terms on the right-hand side of Eq. (6.9) is constant, while β is a fitting parameter, we further simplified Eq. (6.9) to as follows:

$$R_k T^3 = B, \qquad (6.10)$$

where B is also a fitting parameter. And we fitted the Kapitza resistance data estimated by MOOSE to Eq. (6.10).

At last, the Kapitza resistance model was applied in the MOOSE framework to predict effective thermal conductivities for other U-Zr heterogeneous systems with any given temperatures and microstructures, such results were compared to our U-Zr thermal conductivity model [99].

6.3 Results

6.3.1 MOOSE prediction without Kapitza resistance

At first, we used the analytical equation developed by K. Bakker [115] to transform the 3D thermal conductivities of U-Zr alloys predict by our U-Zr thermal conductivity model [99] to 2D. The comparison between the converted-2D and 3D thermal conductivity at different temperatures for U-10Zr alloy is shown in Fig. 6.2(a). Overall, the 2D thermal conductivities are slightly higher than the 3D thermal conductivities. We also compared the errors between converted-2D and 3D thermal conductivity for U-Zr alloys with δ-UZr_2 volume fraction ranging from 10% to 40% in Fig. 6.2(b). And the error is defined in Eq. (6.11):

$$E_{err} = \frac{K_{3D} - K_{2D}}{K_{3D}}, \qquad (6.11)$$

where K_{3D} is the 3D thermal conductivity predicted by our model [99], K_{2D} is the 2D converted thermal conductivity and E_{err} is the fractional difference between 2D and 3D thermal conductivity. The error gradually increases with increasing δ-UZr_2 volume fraction, which is in consistent with the result from Badry et al. [123]. The error calculated in this work is similar to Teague's results [116]. There are discrepancies in the error between our results and Badry's [123] results, which may be caused by the different morphology and distribution of the second phase. Nevertheless, we used the converted 3D-2D thermal conductivity of U-Zr alloys for further comparison and calculation.

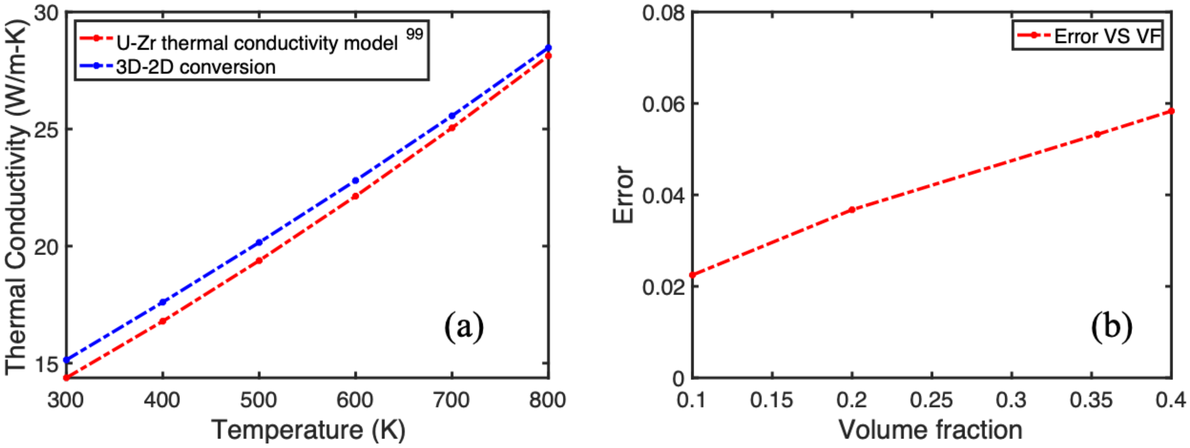

Fig. 6. 2. (a). Comparison between 3D and converted 3D-2D U-10Zr thermal conductivities as a function of temperature with a fixed δ-UZr_2 aspect ratio at 8.1 (b). The error between 3D and converted 3D-2D thermal conductivity at 300K as a function of δ-UZr_2 volume fraction.

For the first step of effective thermal conductivity calculation, the interphase Kapitza resistance was not assigned. And the aspect ratio was fixed at 8.1 for the lamellar δ-UZr_2. The thermal conductivities of both α-U and δ-UZr_2 were extrapolated from our U-Zr thermal conductivity model [99] based on their respective compositions. The effective thermal conductivities predicted by MOOSE were compared with our U-Zr thermal conductivity model [99] and other thermal conductivity models [103-105] mentioned above in Section 6.2.3. The results are shown in Fig. 6.3. Note that the phase boundary thermal conductivity k_{int} is set at 1.5*W/K-m* for Eq. (6.7). In Fig. 6.3, both the Maxwell model [103] and Bruggeman model [104] give similar thermal conductivities at the full temperature range. The MOOSE simulation, the Maxwell model [103] and the Bruggeman model [104] all overpredict thermal conductivities when compared to our U-Zr thermal conductivity model [99]. Clearly, all of these models do not accurately predict the effective thermal conductivity values. However, the Hasselman-Johnson model, which considers a fixed Kapitza resistance, shows smaller discrepancies with the U-Zr thermal conductivity model at certain temperatures, suggesting that the α-U/δ-UZr$_2$ interphase Kapitza resistance should be accounted for the effective thermal conductivity calculation. It also suggests that the Kapitza resistance may be temperature-dependent, because Hasselman-Johnson model cannot predict the accurate thermal conductivities if a fixed resistance value is used.

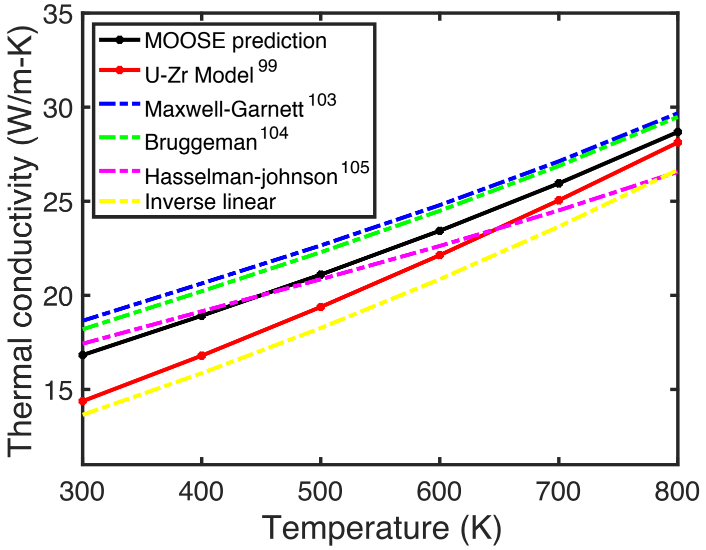

Fig. 6. 3. Thermal conductivity of U-10Zr predicted by different models. The MOOSE and our U-Zr model are denoted as black and red solid lines. The Maxwell [103]*, Bruggeman* [104] *and Hasselman-Johnson* [105] *effective conductivity model are denoted as blue, green, magenta and yellow dashed lines, respectively.*

6.3.2 Kapitza resistance model

As indicated in Section 6.2.2, for the estimation of the Kapitza resistance, the α-U/δ-UZr_2 interphase thermal conductivity is treated as a fitting parameter in the MOOSE calculation, and the thermal conductivities for α-U and δ-UZr_2 are the input parameters. The effective thermal conductivities were fitted to the U-Zr thermal conductivity model [99]. Based on the fitted value of the α-U/δ-UZr_2 interphase thermal conductivity, we calculated the Kapitza resistance for U-5.2Zr, U-8.3Zr and U-11.6Zr (with δ-UZr_2 volume fraction at 20%, 30% and 40% respectively) with a fixed δ-UZr_2 aspect ratio at 8.1 for temperatures between 300-800K, which is shown in Fig. 6.4. In Fig. 6.4(a), the fitted interphase thermal conductivity increases with the increasing temperature. We also noticed a slight increase in interphase thermal conductivity as δ-UZr_2 volume fraction increases at high temperatures. As we converted the fitted interphase thermal conductivity into Kapitza resistance in Fig. 6.4(b), the Kapitza resistance decreases with the temperature. In Fig. 6.4(b), the difference in Kapitza resistance is more pronounced at lower temperatures, which is due to the inverse mathematical conversion between Kapitza resistance and interphase thermal conductivity. As shown in Fig. 6.4(b), when the aspect ratio for δ-UZr_2 is fixed, we did not see a clear dependence of the Kapitza resistance on the volume fraction of δ-UZr_2. Overall, the Kapitza resistance is within a reasonable range between 0.1~5 m^2K/GW and it decreases with the increasing temperature.

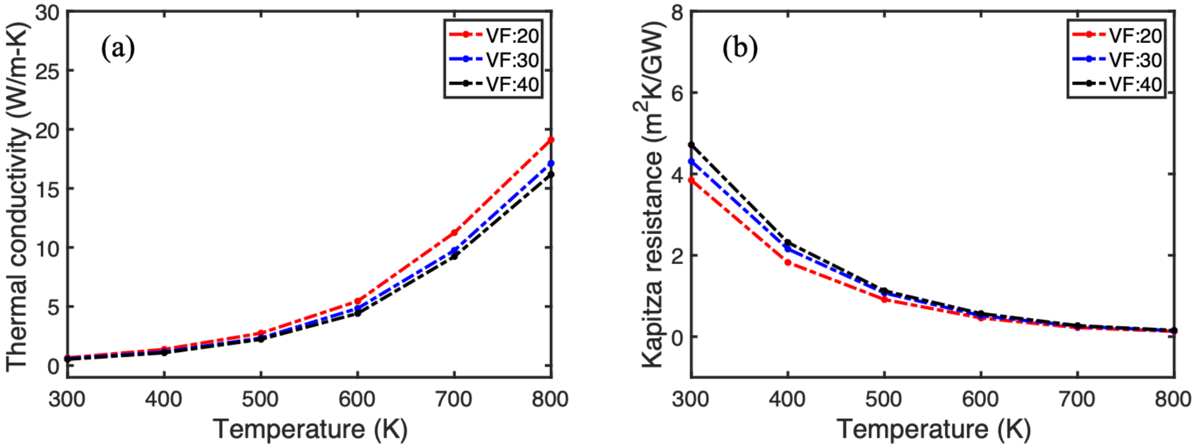

Fig. 6. 4. (a). Fitted α-U/δ-UZr$_2$ interphase thermal conductivity for U-Zr systems with δ-UZr$_2$ volume fraction at 20%, 30% and 40% (Representing U-5.2Zr, U-8.3Zr and U-11.6Zr respectively) as a function of temperature with a fixed δ-UZr$_2$ aspect ratio at 8.1. (b) Calculated Kapitza resistance from the fitted α-U/δ-UZr$_2$ interphase thermal conductivity results.

In the next step, we examined the effect of δ-UZr$_2$ aspect ratio on the Kapitza resistance. We fixed the number of δ-UZr$_2$ in the α-U matrix but changing the aspect ratio of δ-UZr$_2$ so that the volume fraction of δ-UZr$_2$ changes. And we used the same fitting procedure as discussed above. As shown in open literature [106, 117-120], the Kapitza resistance has a T^{-3}-dependence. Therefore, we calculated RT^3 as a function of temperature and aspect ratio in Fig. 6.5. The temperature ranges from 300K to 800K. The aspect ratio ranges between 5.4 to 12.15, representing the δ-UZr$_2$ volume fraction from 20% to 45%. In Fig. 6.5(a), for the aspect ratios of δ-UZr$_2$ above 8.1, RT^3 remains almost constant at the full temperature range. For smaller aspect ratios, initially RT^3 increases slightly then decreases with the increasing temperature. According to Eq. (6.8), above the Debye temperature, even though the value for $\partial\Theta_h/\partial T$ is small, it may still impact the overall value of

RT^3. Therefore, we do expect a slight decrease in RT^3 at higher temperatures. Overall, the Kapitza resistance does not change much with temperature. And RT^3 as a function of aspect ratio at different temperatures has been calculated and shown in Fig. 6.5(b). The slope for RT^3 as a function of aspect ratio is similar at temperatures between 300~600K, while the slope decreases for temperatures at 700K and 800K. This is in consistence with the conclusion that the phonon-mediated thermal transport in the metallic system becomes negligible at high temperatures, which may cause a slight decrease Kapitza resistance.

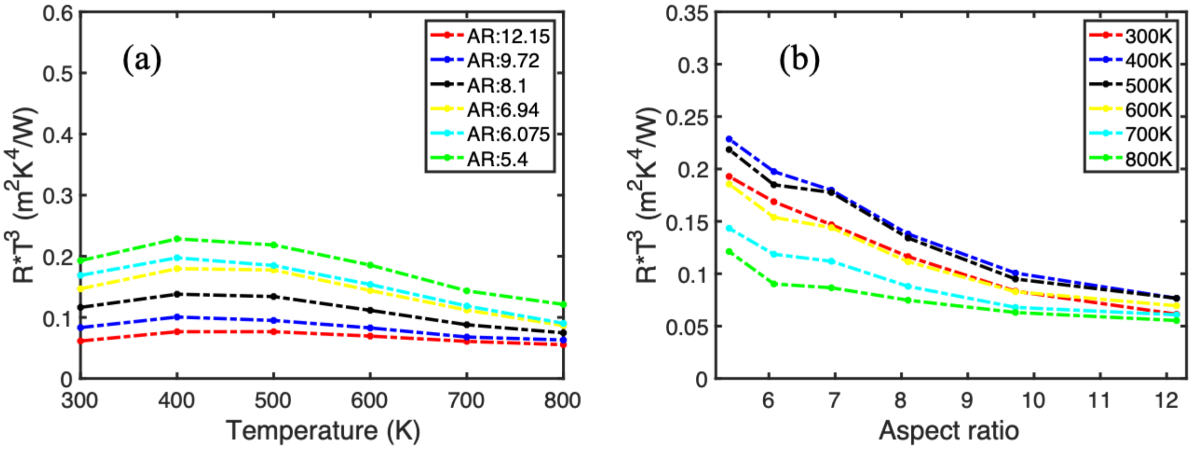

Fig. 6. 5. (a) Calculated RT^3 as a function of temperature for α-U + δ-UZr_2 laminar structure with fixed number of δ-UZr_2 phase but different δ-UZr_2 aspect ratios ranging from 5.4~12.5. (b). RT^3 as a function of aspect ratio at different temperatures.

Based on the assumption that the Kapitza resistance has a T^3 dependence, we took the average of RT^3 values at the full temperature range for each δ-UZr_2 aspect ratio. The averaged RT^3

as a function of aspect ratio is shown in Fig. 6.6, which decreases with the increasing aspect ratio, and reaches a plateau when the aspect ratio becomes large enough. Therefore, we fit the averaged RT^3 to an exponential decay function, by including the aspect ratio into Eq. (6.10). The equation is re-written as follows:

$$R_k T^3 = a * AR^b, \qquad (6.12)$$

where AR is the aspect ratio of the second phase; a and b are fitting parameters, which are determined as 1.5463 and -1.267, respectively. Eq. (6.12) is compared against the averaged RT^3 values in Fig. 6.6. Clearly, Eq. (6.12) has a good agreement with the averaged RT^3 values within the fitting range.

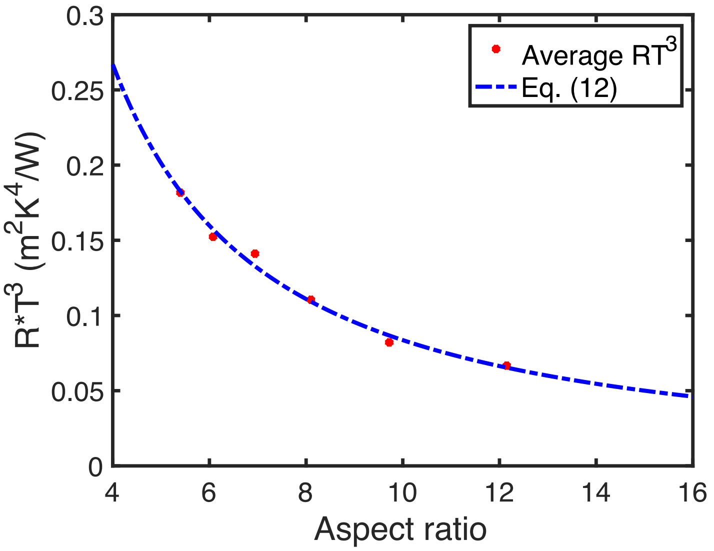

Fig. 6. 6. Comparison between the averaged RT^3 over the full temperature range and the fitted Kapitza resistance model (Eq. (6.12)) as a function of δ-UZr_2 aspect ratio.

6.3.3 Effective thermal conductivity prediction

At last, we implemented Eq. (6.12) into MOOSE (denoted as R-MOOSE model) to predict the effective thermal conductivities of heterogeneous U-Zr systems within and outside the fitting range to validate the accuracy of our developed temperature- and aspect-ratio-dependent Kapitza resistance model. In the mesoscale modeling in MOOSE, the Kapitza resistance is predicted by Eq. (6.12), and thermal conductivities for α-U and δ-UZr_2 are the input parameters. The R-MOOSE model is compared against our U-Zr thermal conductivity model [99] in Fig. 6.7 for different U-Zr microstructures. For U-Zr microstructure within the fitting range, the effective thermal conductivity for U-7.3Zr with δ-UZr_2 aspect ratio of 9 is calculated by the R-MOOSE model and compared with the U-Zr thermal conductivity model [99] in Fig. 6.7(a), and the R-MOOSE model accurately predict the thermal conductivity values at the full temperature range. Fig. 6.7(b), Fig. 6.7(c) and Fig. 6.7(d) show the comparison for U-Zr configurations outside the fitting range. In Fig. 6.7(b) and Fig. 6.7(c), only one parameter for the U-Zr microstructure lies outside the fitting range, i.e. δ-UZr_2 aspect ratio and Zr weight fraction, respectively. Here the fitting range for Zr weight fraction is 5.63%-13.44%, and that for the aspect ratio is 5.4-12.15. The two microstructures are U-9Zr with δ-UZr_2 aspect ratio at 15 and U-3.4Zr with δ-UZr_2 aspect ratio at 12. The R-MOOSE model also accurately predicts the effective thermal conductivity for both microstructures. The effective thermal conductivity for U-15.4Zr with δ-UZr_2 aspect ratio at 12.9 predicted by R-MOOSE is plotted in Fig. 6.7(d). Both δ-UZr_2 aspect ratio and Zr weight fraction are outside the fitting range. Our R-MOOSE model still gives accurate results. Overall, regardless of U-Zr microstructures within or outside the fitting range, our R-MOOSE model consistently predicts accurate effective thermal conductivity results.

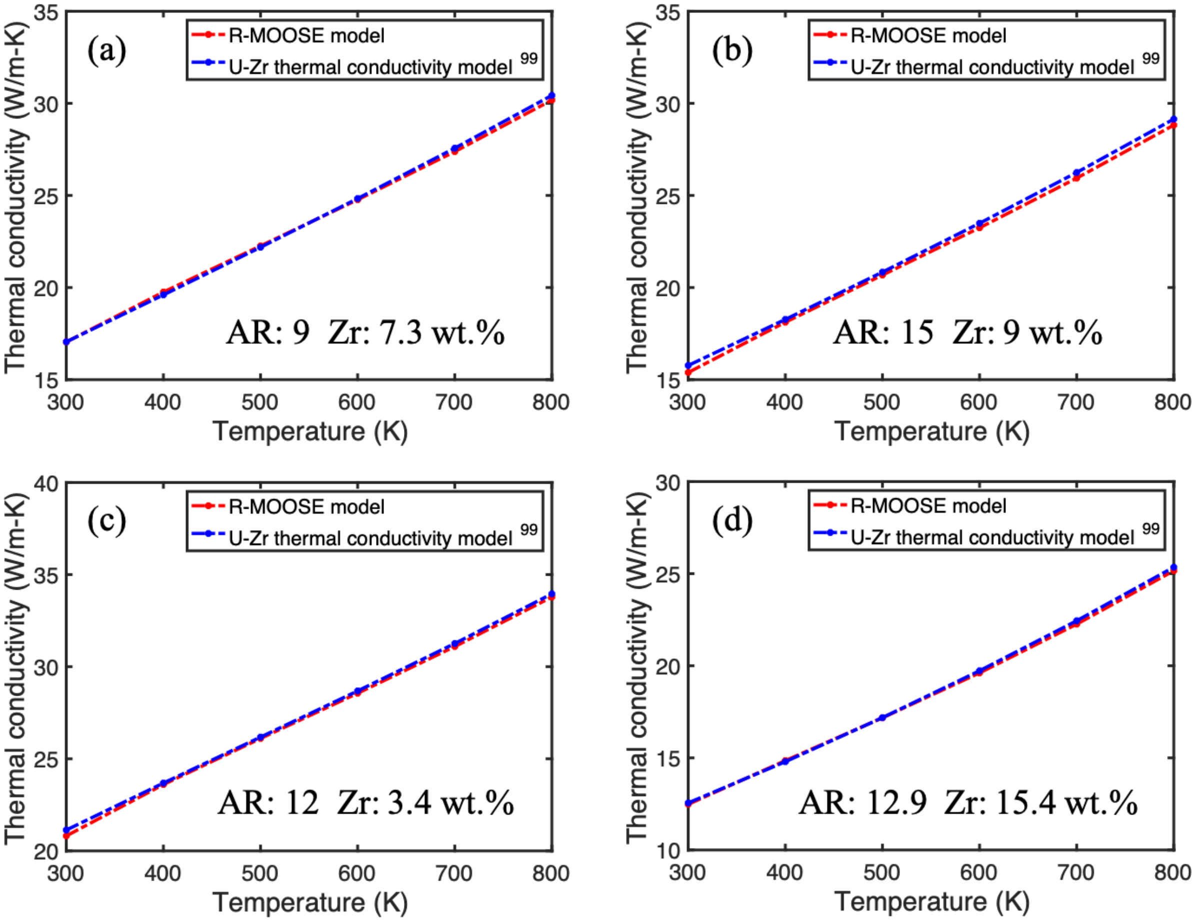

Figure 6.7. Comparison between the R-MOOSE model and our U-Zr thermal conductivity model [99] *at different aspect ratios and Zr weight fractions. (a) Within the fitting range, with δ-UZr$_2$ aspect ratio at 9 and Zr weight fraction at 7.3%. (b) Zr weight fraction within the fitting range at 9% and δ-UZr$_2$ aspect ratio outside the fitting range at 15. (c) Zr weight fraction outside the fitting range at 3.4% and δ-UZr$_2$ aspect ratio within the fitting range at 12. (d) Both Zr weight fraction and aspect ratio outside the fitting range at 15.4% and 12.9, respectively.*

6.4 Conclusions and discussion

In summary, mesoscale phase field modeling coupled with the AEH method in the MOOSE framework has been used to calculate the effective thermal conductivities of U-Zr heterogeneous microstructures. Specifically, microstructures with lamellar δ-UZr_2 phases embedded in an α-U matrix are created with two varying parameters: Zr weight fraction and δ-UZr_2 aspect ratio. Effective thermal conductivities calculated by MOOSE are compared with various analytical models for composite systems [103-105], as well as with our newly developed U-Zr thermal conductivity model [99]. However, the discrepancies are large. Therefore, our results show that the interphase boundary thermal resistance (Kapitza resistance) should be included in the effective thermal conductivity calculation.

There are a number of effective thermal conductivity models that consider the Kapitza resistance [107, 108, 110]. However, those models do not quantitatively determine the dependence of Kapitza resistance on temperatures and the morphology of the second phase. As for certain specific systems such as the U-Zr heterogeneous microstructure in this work, the Kapitza resistance determined by those models may not work. Therefore, we have examined the temperature effect as well as the effect of the morphology of the second phase on the Kapitza resistance in this work. We used MOOSE to create different U-Zr heterogeneous microstructures with varying δ-UZr_2 volume fractions, δ-UZr_2 aspect ratios and Zr weight fractions. In MOOSE effective thermal conductivity calculation, the interphase thermal conductivity is treated as the only fitting parameter, and the calculation result is fitted to our U-Zr thermal conductivity model [99]. We obtained the Kapitza resistance as a function of temperature, δ-UZr_2 volume fraction as well as the aspect ratio of δ-UZr_2. The Kapitza resistance does not change much with the δ-UZr_2 volume fraction if the aspect ratio is fixed. We found that the Kapitza resistance is showing a T^3-

dependence, which is consistent with literature results [106, 117-120]. In addition, RT^3 decreases with increasing aspect ratio of δ-UZr_2. Using the mesoscale modeling results for calibration, we have developed an analytical Kapitza resistance model to capture the effects of both temperature and aspect ratio of the second phase (δ-UZr_2).

Aftr the temperature- and aspect-ratio-dependent Kapitza resistance model is developed, we implemented it in the MOOSE (R-MOOSE) for calculating the effective thermal conductivities of heterogeneous U-Zr microstructures within and outside the fitting range to validate our Kapitza resistance model. The R-MOOSE model accurately predicts the effective thermal conductivities of several U-Zr microstructures at a wide range of temperatures. Unlike previous effective thermal conductivity models, our Kapitza resistance model is more comprehensive and directly includes the effects of temperature and second-phase geometry.

Although this R-MOOSE model is developed for U-Zr systems, the approach to determine the Kapitza resistance can be extended to other systems, as long as the thermal conductivities based on their nominal composition are known. This model is based on the assumption that the value of RT^3 does not change significantly at temperatures above Debye temperature. Therefore, this model could be applied to other metallic fuel systems such as U-Si and U-Mo. Using this R-MOOSE model, one can determine the local effective thermal conductivity of a given heterogeneous α-U + δ-UZr_2 laminar microstructure if the temperature, aspect ratio, and thermal conductivities of individual phases are known. Therefore, this R-MOOSE model could be coupled with other models such as the gas swelling model, grain growth model, and constituent redistribution model for the fuel performance calculation [41, 86].

Chapter 7: Summary

In Chapter 1, we have introduced different types of nuclear reactors and nuclear fuels. The oxide fuels are the widely used fuel type in current light water reactors, and metallic fuels are the promising fuel type for the next-generation fast reactors. Therefore, we have introduced two research topics covering both metallic fuels and oxide fuels in this report. In Chapter 2, we introduce some background knowledge of U-Zr fuels and UO_2 fuels. Such background knowledge is critical for understanding the importance of thermal transport in both metallic and oxide fuels. And we have also summarized the previous literature work that has been done regarding the thermal conductivity calculation and prediction for U-Zr and UO_2 systems. Such information provides motivation for the new research efforts described in this work.

In Chapter 3, we conducted MD simulations to examine the dispersed Xe effect on the UO_2 thermal conductivity using three different interatomic potentials (Basak, Busker, CRG). At first, we calculated the thermal conductivities of single crystal UO_2 with the three potentials. The results are in good agreement with a previous study in which different interatomic potentials predict different thermal conductivities. Next, we calculated the thermal conductivity of UO_2+Xe system with the three potentials. We noticed that as the thermal conductivities are converted to normalized values, they are quantitatively similar between the three potentials for a wide range of Xe concentrations and temperatures. Based on this unified effect, we have developed a model that combines the Xe scattering term and the Fink's empirical model using the average results from the three potentials. Finally, we use this new UO_2+Xe thermal conductivity model to evaluate the effective thermal conductivities of UO_2 consisting of multiple microstructure features (grain boundaries, Xe bubble, dispersed Xe atoms, etc), i.e. the small-grain HBS and the large-grain unrestructured fuel. Our results show that the HBS will have a higher thermal conductivity than the unrestructured fuel in UO_2, which is consistent with experimental observations. The critical Xe concentration that can offset the GB thermal resistance effect on UO_2 thermal conductivity in the HBS has also been examined and compared with the model currently implemented in MARMOT. A different Xe concentration is determined in this work.

Not only the dispersed Xe can significantly degrade the UO_2 thermal conductivity, Xe bubbles can also affect the UO_2 thermal conductivity. In Chapter 4, we have studied the Xe bubble effect on the UO_2 thermal conductivity. We found out that, at a fixed porosity, the UO_2 thermal conductivity increases with the void size, suggesting that the smaller voids cause more thermal conductivity reduction than clustering them into large defect clusters. And it will reach a saturated value at a void radius of 0.6 nm. Next, we have examined the bubble pressure effect on the UO_2 thermal conductivity. It is found that at a low Xe:V_U ratio within bubbles, there is no further reduction in UO_2 thermal conductivity if some Xe atoms are added into the bubble. However, when the Xe concentration is high in the bubble, the UO_2 thermal conductivity decreases with increasing Xe:V_U ratio (or Xe bubble pressure). The critical Xe:V_U ratio is determined at 0.75. Detailed atomistic visualization shows that the bubble surface atoms are displaced to release the increased bubble pressure, which causes additional phonon scattering at the bubble interface. This mechanism is different from helium atoms in helium bubble that helium atoms can diffuse to the surrounding UO_2 lattice to reduce the thermal conductivity.

In Chapter 5, we have developed a new semi-empirical thermal conductivity model for the whole composition range and a wide range of temperatures for U-Zr fuels. We use the thermal resistivity approach and consider only the electron contributions to the overall resistivity. At first, we determine the electrical resistivities of pure U and pure Zr from fitting the three scattering terms (electron-defect scattering, electron-phonon scattering, and electron-electron scattering) to the available experimental data. Then we use the Wiedemann-Franz law to calculate the thermal resistivity from the electrical resistivity. Next, we developed a new mixing rule for the binary alloys and used the experimental data to parameterize our model. The new model prediction shows good agreement with most of the experimental data. Compared with other models, our new model also has some improvements at certain temperature and composition ranges.

We have used mesoscale phase field modeling coupled with the AEH method in the MOOSE framework to predict the effective thermal conductivities of heterogamous microstructures in U-Zr fuels, which is described in Chapter 6. Heterogeneous α-U + δ-UZr_2 lamellar microstructures were constructed in MOOSE. The thermal conductivities for individual α-U and δ-UZr_2 phases predicted by our U-Zr thermal conductivity model (described in Chapter 5) are input parameters in the MOOSE calculation. At first, the interphase Kapitza resistance was not assigned in the MOOSE calculation. The MOOSE results overpredict thermal conductivities when compared to the U-Zr thermal conductivity model, suggesting that the interphase Kapitza resistance should be considered. In the next step, the α-U/δ-UZr_2 interface Kapitza resistance is treated as a fitting parameter, and the effective thermal conductivities predicted by MOOSE are fitted to the U-Zr thermal conductivity model. Different U-Zr microstructures were created. The simulation results indicate that the Kapitza resistance has a strong dependence on both temperature and the aspect ratio of the second phase. However, it is found that the Kapitza resistance does not depend on the volume fraction of the second phase if the aspect ratio of the second phase is fixed. Then, based on the fitted results, we developed an empirical model to quantify the effects of temperature and the aspect ratio of the second phase on the Kapitza resistance. At last, we implemented the Kapitza resistance model in the MOOSE framework as a R+MOOSE model. The new R+MOOSE model accurately predicts the effective thermal conductivities of a number of U-Zr microstructures at a wide rang of temperatures, even at conditions outside the fitting range.

List of Scientific Communications

Journal articles and conference papers:

W. Chen and X.M. Bai, “Temperature and Composition Dependent Thermal Conductivity Model for U-Zr Alloys", Journal of Nuclear Materials 507, 360-370 (2018).

W. Chen and X.M. Bai, “Development of Thermal Conductivity Models for U-Zr and U-Pu Alloys”, Transactions of the American Nuclear Society 119, 509-511 (2018).

W. Chen, Michael W.D. Cooper, Ziqi Xiao, David A. Andersson and X.M. Bai, “Effect of Xe bubble size and pressure on the thermal conductivity of UO2—A molecular dynamics study”, Journal of Materials Research 34(13): 2295-2305 (2019).

W. Chen and X.M. Bai, “Unified effect of dispersed Xe on thermal conductivity of UO2 predicted by three interatomic potentials”, JOM 72, 1710–1718 (2020).

W. Chen and X.M. Bai, “A Mesoscale modeling of Microstructure-dependent thermal conductivity for unirradiated U-Zr fuels”, being prepared for a peer-review journal.

Presentations:

W. Chen and X.M. Bai, (Apr. 2018) “A Mechanistic Thermal Conductivity Model for U-Zr Alloys”, Presented at Materials Research Society (MRS) meeting, Phoenix, AZ.

W. Chen and X.M. Bai, (2018) “A Mechanistic Thermal Conductivity Model for U-Zr Alloys”, Presented at MSE seminar, Virginia Tech.

W. Chen and X.M. Bai, (2020), "Molecular Dynamics Studies of Thermal Conductivity Degradation of UO_2 due to Dispersed Xe Atoms and Xe Bubbles", Presented TMS Annual Meeting, San Diego, CA.

W. Chen and X.M. Bai, (2020), "Molecular Dynamics Studies of Thermal Conductivity Degradation of UO_2 due to Dispersed Xe Atoms and Xe Bubbles", Presented at MSE seminar, Virginia Tech.

Bibliography

[1] S. Chu, A. Majumdar, Opportunities and challenges for a sustainable energy future, Nature 488(7411) (2012) 294-303.

[2] D. Staicu, Thermal Properties of Irradiated UO2 and MOX, Comprehensive Nuclear Materials, Elsevier, Oxford, 2012, pp. 439-464.

[3] C. Ronchi, M. Sheindlin, D. Staicu, M. Kinoshita, Effect of burn-up on the thermal conductivity of uranium dioxide up to 100.000 MWdt−1, Journal of Nuclear Materials 327(1) (2004) 58-76.

[4] D.D. Baron, L. Hallstadius, Fuel Performance of Light Water Reactors, Comprehensive Nuclear Materials, Elsevier, Oxford, 2012, pp. 481-514.

[5] J.M. Harp, P.A. Lessing, R.E. Hoggan, Uranium silicide pellet fabrication by powder metallurgy for accident tolerant fuel evaluation and irradiation, J Nucl Mater 466 (2015) 728-738.

[6] M.R. Finlay, G.L. Hofman, J.L. Snelgrove, Irradiation behaviour of uranium silicide compounds, J Nucl Mater 325(2) (2004) 118-128.

[7] J.K. Fink, Thermophysical properties of uranium dioxide, J Nucl Mater 279(1) (2000) 1-18.

[8] C.V. Sundaram, S.L. Mannan, Nuclear fuels and development of nuclear fuel elements, Sadhana 14(1) (1989) 21-57.

[9] V.V. Rondinella, T. Wiss, The high burn-up structure in nuclear fuel, Materials Today 13(12) (2010) 24-32.

[10] K. Une, K. Nogita, S. Kashibe, M. Imamura, Microstructural change and its influence on fission gas release in high burnup UO2 fuel, J Nucl Mater 188 (1992) 65-72.

[11] T. Wiss, Radiation Effects in UO2, Comprehensive Nuclear Materials, Elsevier, Oxford, 2012, pp. 465-480.

[12] H. Stehle, Performance of oxide nuclear fuel in water-cooled power reactors, J Nucl Mater 153 (1988) 3-15.

[13] X.Y. Liu, M.W.D. Cooper, K.J. McClellan, J.C. Lashley, D.D. Byler, B.D.C. Bell, R.W. Grimes, C.R. Stanek, D.A. Andersson, Molecular Dynamics Simulation of Thermal Transport in UO2 Containing Uranium, Physical Review Applied 6(4) (2016) 044015.

[14] J.M. Harp, D.L. Porter, B.D. Miller, T.L. Trowbridge, W.J. Carmack, Scanning electron microscopy examination of a Fast Flux Test Facility irradiated U-10Zr fuel cross section clad with HT-9, J Nucl Mater 494 (2017) 227-239.

[15] Y.S. Kim, G.L. Hofman, S.L. Hayes, Y.H. Sohn, Constituent redistribution in U-Pu-Zr fuel during irradiation, J Nucl Mater 327(1) (2004) 27-36.

[16] T. Ogata, 3.01 - Metal Fuel, in: R.J.M. Konings (Ed.), Comprehensive Nuclear Materials, Elsevier, Oxford, 2012, pp. 1-40.

[17] T. Sofu, A review of inherent safety characteristics of metal alloy sodium-cooled fast reactor fuel against postulated accidents, Nuclear Engineering and Technology 47(3) (2015) 227-239.

[18] G.L. Hofman, R.G. Pahl, C.E. Lahm, D.L. Porter, Swelling Behavior of U-Pu-Zr Fuel, Metall Trans A 21(3) (1990) 517-528.

[19] D.D. Keiser Jr, 3.15 - Metal Fuel-Cladding Interaction A2 - Konings, Rudy J.M, Comprehensive Nuclear Materials, Elsevier, Oxford, 2012, pp. 423-441.

[20] M.H. K. Une, K. Nogita, T. Hosokawa, Y. Suzawa, S. Shimizu, Y. Etoh, Rim structure formation and high burnup fuel behavior of large-grained UO2 fuels, J Nucl Mater 278(1) (2000) 54-63.

[21] C.T. Walker, D. Staicu, M. Sheindlin, D. Papaioannou, F.S. W. Goll, On the thermal conductivity of UO2 nuclear fuel at a high burn-up of around 100MWd/kgHM, J Nucl Mater 350(1) (2006) 19-39.

[22] X.M. Bai, M.R. Tonks, Y.F. Zhang, J.D. Hales, Multiscale modeling of thermal conductivity of high burnup structures in UO2 fuels, J Nucl Mater 470 (2016) 208-215.

[23] G.L. Hofman, S.L. Hayes, M.C. Petri, Temperature gradient driven constituent redistribution in U-Zr alloys, J Nucl Mater 227(3) (1996) 277-286.

[24] Y.S. Kim, S.L. Hayes, G.L. Hofman, A.M. Yacout, Modeling of constituent redistribution in U-Pu-Zr metallic fuel, J Nucl Mater 359(1-2) (2006) 17-28.

[25] J. Galloway, C. Unal, N. Carlson, D. Porter, S. Hayes, Modeling constituent redistribution in U-Pu-Zr metallic fuel using the advanced fuel performance code BISON, Nucl Eng Des 286 (2015) 1-17.

[26] M. Kurata, Phase Diagrams of Actinide Alloys, Comprehensive Nuclear Materials, Vol 2: Material Properties/Oxide Fuels for Light Water Reactors and Fast Neutron Reactors (2012) 139-195.

[27] B.R. Butcher, A.H. Rowe, Phase Transformation in Uranium, Nature 172(4383) (1953) 817-817.

[28] S. Nichenko, D. Staicu, Molecular Dynamics study of the effects of non-stoichiometry and oxygen Frenkel pairs on the thermal conductivity of uranium dioxide, J Nucl Mater 433(1) (2013) 297-304.

[29] S. Yamasaki, T. Arima, K. Idemitsu, Y. Inagaki, Evaluation of Thermal Conductivity of Hyperstoichiometric UO2+x by Molecular Dynamics Simulation, International Journal of Thermophysics 28(2) (2007) 661-673.

[30] X.-M. Bai, A. El-Azab, J. Yu, T.R. Allen, Migration mechanisms of oxygen interstitial clusters in UO2, Journal of Physics: Condensed Matter 25(1) (2012) 015003.

[31] X.-M. Bai, H. Ke, Y. Zhang, B.W. Spencer, J. Nucl. Mater. 495 (2017) 442.

[32] M.R. Tonks, X.-Y. Liu, D. Andersson, D. Perez, A. Chernatynskiy, G. Pastore, C.R. Stanek, R. Williamson, Development of a multiscale thermal conductivity model for fission gas in UO2, J Nucl Mater 469 (2016) 89-98.

[33] C.W. Lee, A. Chernatynskiy, P. Shukla, R.E. Stoller, S.B. Sinnott, S.R. Phillpot, Effect of pores and He bubbles on the thermal transport properties of UO2 by molecular dynamics simulation, J Nucl Mater 456 (2015) 253-259.

[34] B. Deng, A. Chernatynskiy, P. Shukla, S.B. Sinnott, S.R. Phillpot, Effects of edge dislocations on thermal transport in UO2, J Nucl Mater 434(1) (2013) 203-209.

[35] T. Chen, D. Chen, B.H. Sencer, L. Shao, Molecular dynamics simulations of grain boundary thermal resistance in UO2, J Nucl Mater 452(1) (2014) 364-369.

[36] A. Chernatynskiy, C. Flint, S.B. Sinnott, S.R. Phillpot, Critical assessment of UO2 classical potentials for thermal conductivity calculations, Journal of Materials Science 47(21) (2012) 7693-7702.

[37] R.J. White, The development of grain-face porosity in irradiated oxide fuel, J Nucl Mater 325(1) (2004) 61-77.

[38] D.A. Andersson, P. Garcia, X.Y. Liu, G. Pastore, M. Tonks, P. Millett, B. Dorado, D.R. Gaston, D. Andrs, R.L. Williamson, R.C. Martineau, B.P. Uberuaga, C.R. Stanek, Atomistic modeling of intrinsic and radiation-enhanced fission gas (Xe) diffusion in UO2±x: Implications for nuclear fuel performance modeling, J Nucl Mater 451(1) (2014) 225-242.

[39] A.D. Andersson, R.T. Perriot, G. Pastore, M.R. Tonks, M.W. Cooper, X.-Y. Liu, A. Goyal, B.P. Uberuaga, C.R. Stanek, Report on simulation of fission gas and fission product diffusion in UO2, Los Alamos National Laboratory (LA-UR-15-28086), 2016.

[40] E. Moore, L. René Corrales, T. Desai, R. Devanathan, Molecular dynamics simulation of Xe bubble nucleation in nanocrystalline UO2 nuclear fuel, J Nucl Mater 419(1) (2011) 140-144.

[41] M.R. Tonks, D. Gaston, P.C. Millett, D. Andrs, P. Talbot, An object-oriented finite element framework for multiphysics phase field simulations, Computational Materials Science 51(1) (2012) 20-29.

[42] S. Plimpton, Fast Parallel Algorithms for Short-Range Molecular Dynamics, Journal of Computational Physics 117(1) (1995) 1-19.

[43] G. Busker, A. Chroneos, R.W. Grimes, I.W. Chen, Solution Mechanisms for Dopant Oxides in Yttria, Journal of the American Ceramic Society 82(6) (1999) 1553-1559.

[44] C.B. Basak, A.K. Sengupta, H.S. Kamath, Classical molecular dynamics simulation of UO2 to predict thermophysical properties, J Alloy Compd 360(1) (2003) 210-216.

[45] M.W.D. Cooper, M.J.D. Rushton, R.W. Grimes, A many-body potential approach to modelling the thermomechanical properties of actinide oxides, Journal of Physics: Condensed Matter 26(10) (2014) 105401.

[46] M.W.D. Cooper, N. Kuganathan, P.A. Burr, M.J.D. Rushton, R.W. Grimes, C.R. Stanek, D.A. Andersson, Development of Xe and Kr empirical potentials for CeO2, ThO2, UO2 and PuO2, combining DFT with high temperature MD, Journal of Physics: Condensed Matter 28(40) (2016) 405401.

[47] R.W. Grimes, C.C. Richard, The stability of fission products in uranium dioxide, Philosophical Transactions of the Royal Society of London. Series A: Physical and Engineering Sciences 335(1639) (1991) 609-634.

[48] H.Y. Geng, Y. Chen, Y. Kaneta, M. Kinoshita, Molecular dynamics study on planar clustering of xenon in UO2, Journal of Alloys and Compounds 457(1) (2008) 465-471.

[49] K.T. Tang, J.P. Toennies, The van der Waals potentials between all the rare gas atoms from He to Rn, The Journal of Chemical Physics 118(11) (2003) 4976-4983.

[50] P.K. Schelling, S.R. Phillpot, P. Keblinski, Comparison of atomic-level simulation methods for computing thermal conductivity, Phys Rev B 65(14) (2002) 144306.

[51] K. Gofryk, S. Du, C.R. Stanek, J.C. Lashley, X.Y. Liu, R.K. Schulze, J.L. Smith, D.J. Safarik, D.D. Byler, K.J. McClellan, B.P. Uberuaga, B.L. Scott, D.A. Andersson, Anisotropic thermal conductivity in uranium dioxide, Nature Communications 5 (2014) 4551.

[52] A. Chernatynskiy, S.R. Phillpot, Evaluation of computational techniques for solving the Boltzmann transport equation for lattice thermal conductivity calculations, Phys Rev B 82(13) (2010) 134301.

[53] C.I. Maxwell, J. Pencer, Molecular dynamics modelling of the thermal conductivity of off-stoichiometric UO2±x and (UyPu1−y)O2±x using equilibrium molecular dynamics, Annals of Nuclear Energy 131 (2019) 317-324.

[54] R. Brandt, G. Neuer, J. Non-Equilib. Thermodyn., 1976, p. 3.

[55] H.-S. Yang, G.R. Bai, L.J. Thompson, J.A. Eastman, Interfacial thermal resistance in nanocrystalline yttria-stabilized zirconia, Acta Materialia 50(9) (2002) 2309-2317.

[56] K. Pietrak, T. Wiśniewski, A review of models for effective thermal conductivity of composite materials, Journal of Power Technologies 95(1) (2015) 14-24.

[57] P. Nikolopoulos, G. Ondracek, Conductivity bounds for porous nuclear fuels, J Nucl Mater 114(2) (1983) 231-233.

[58] C. Walker, Electron probe microanalysis of irradiated nuclear fuel: an overview, Journal of Analytical Atomic Spectrometry 14(3) (1999) 447-454.

[59] X.-Y. Liu, C.R. Stanek, A.D.R. Andersson, Effect of point defects on the thermal conductivity of UO2: molecular dynamics simulations, Los Alamos National Laboratory (LA-UR-15-28086), United States, 2015.

[60] P.C. Millett, M. Tonks, Meso-scale modeling of the influence of intergranular gas bubbles on effective thermal conductivity, J Nucl Mater 412(3) (2011) 281-286.

[61] R.P. Agarwala, Diffusion processes in nuclear materials, North-Holland, Amsterdam, 1992.

[62] J.C. Maxwell, A treatise on electricity and magnetism, Clarendon press1881.

[63] D.R. Olander, Fundamental aspects of nuclear reactor fuel elements, California University (TID-26711-P1), United States, 1976.

[64] F.X. Alvarez, D. Jou, A. Sellitto, Pore-size dependence of the thermal conductivity of porous silicon: A phonon hydrodynamic approach, Applied Physics Letters 97(3) (2010) 033103.

[65] S. Kashibe, K. Une, K. Nogita, Formation and growth of intragranular fission gas bubbles in UO2 fuels with burnup of 6–83 GWd/t, J Nucl Mater 206(1) (1993) 22-34.

[66] J.A. Turnbull, The distribution of intragranular fission gas bubbles in UO2 during irradiation, J Nucl Mater 38(2) (1971) 203-212.

[67] A. Chernatynskiy, J.E. Turney, A.J.H. McGaughey, C.H. Amon, S.R. Phillpot, Phonon-Mediated Thermal Conductivity in Ionic Solids by Lattice Dynamics-Based Methods, Journal of the American Ceramic Society 94(10) (2011) 3523-3531.

[68] A. Chernatynskiy, X.-M. Bai, J. Gan, Systematic investigation of the misorientation- and temperature-dependent Kapitza resistance in CeO2, International Journal of Heat and Mass Transfer 99 (2016) 461-469.

[69] Y. Lee, S. Lee, G.S. Hwang, Effects of vacancy defects on thermal conductivity in crystalline silicon: A nonequilibrium molecular dynamics study, Phys Rev B 83(12) (2011) 125202.

[70] S.-H. Choi, S. Maruyama, K.-K. Kim, J.-H. Lee, Evaluation of the phonon mean free path in thin films by using classical molecular dynamics, Journal of the Korean Physical Society 43(5) (2003) 747-753.

[71] X.Y. Liu, D.A. Andersson, Molecular dynamics study of fission gas bubble nucleation in UO2, J Nucl Mater 462 (2015) 8-14.

[72] L. Hu, B.D. Wirth, D. Maroudas, Thermal conductivity of tungsten: Effects of plasma-related structural defects from molecular-dynamics simulations, Applied Physics Letters 111(8) (2017) 081902.

[73] P. Garcia, P. Martin, G. Carlot, E. Castelier, M. Ripert, C. Sabathier, C. Valot, F. D’Acapito, J.L. Hazemann, O. Proux, V. Nassif, A study of xenon aggregates in uranium dioxide using X-ray absorption spectroscopy, J Nucl Mater 352(1) (2006) 136-143.

[74] C. Ronchi, Extrapolated equation of state for rare gases at high temperatures and densities, J Nucl Mater 96(3) (1981) 314-328.

[75] K. Nogita, K. Une, High resolution TEM observation and density estimation of Xe bubbles in high burnup UO2 fuels, Nuclear Instruments and Methods in Physics Research Section B: Beam Interactions with Materials and Atoms 141(1) (1998) 481-486.

[76] M.W.D. Cooper, M.J.D. Rushton, R.W. Grimes, Potential Model for Fission Gases in Actinide Oxides. Retrieved from http://abulafia.mt.ic.ac.uk/potentials/actinide_potentials_gases/v1.0/index.html.

[77] Y. Touloukian, P. Powell, C. Ho, P. Klemens, Thermodynamics properties of matter, Vol. 1, Plenum, New York, 1970.

[78] Y. Takahashi, M. Yamawaki, K. Yamamoto, Thermo-Physical Properties of Uranium Zirconium Alloys, J Nucl Mater 154(1) (1988) 141-144.

[79] T. Matsui, T. Natsume, K. Naito, Heat-Capacity Measurements of U0.80zr0.20 and U0.80mo0.20 Alloys from Room-Temperature to 1300-K, J Nucl Mater 167 (1989) 152-159.

[80] I.L. Argonne National Laboratory, Chemical Technology Division Annual Technical Report, 1986, 1987.

[81] S. Kaity, J. Banerjee, M. Nair, K. Ravi, S. Dash, T. Kutty, A. Kumar, R. Singh, Microstructural and thermophysical properties of U–6 wt.% Zr alloy for fast reactor application, J Nucl Mater 427(1-3) (2012) 1-11.

[82] D.E. Janney, C.A. Papesch, D.E. Burkes, J.I. Cole, R.S. Fielding, S.M. Frank, T. Hartmann, T.A. Hyde, D.D. Keiser Jr, J.R. Kennedy, Metallic Fuels Handbook, Idaho National Lab.(INL), Idaho Falls, ID (United States), 2017.

[83] T. Ogata, J. Nucl. Sci. Technol. 675 (Suppl. 3) (2002) p. 37.

[84] G.L. Hofman, L. Leibowitz, J.M. Kramer, M.C. Billone, J.F. Koenig, Metallic fuels handbook. No. ANL-IFR--29. Argonne National Laboratory (ANL), Argonne, IL (United States), ; Argonne National Lab. (ANL), Argonne, IL (United States), 1985, p. Medium: ED; Size: 181 p.

[85] Y.S. Kim, T.W. Cho, D.S. Sohn, Thermal conductivities of actinides (U, Pu, Np, Cm, Am) and uranium-alloys (U-Zr, U-Pu-Zr and U-Pu-TRU-Zr), J Nucl Mater 445(1-3) (2014) 272-280.

[86] J. Hales, R. Williamson, S. Novascone, G. Pastore, B. Spencer, D. Stafford, K. Gamble, D. Perez, W. Liu, BISON Theory Manual The Equations Behind Nuclear Fuel Analysis, Idaho National Laboratory (INL), Idaho Falls, ID (United States), 2016.

[87] T.M. Tritt, Thermal conductivity: theory, properties, and applications, Springer Science & Business Media2005.

[88] C.Y. Ho, R.W. Powell, P.E. Liley, Thermal conductivity of the elements: a comprehensive review, NATIONAL STANDARD REFERENCE DATA SYSTEM, 1974.

[89] M.C. Karamargin, P.G. Klemens, F.P. Lipschultz, C.A. Reynolds, Lattice Thermal-Conductivity and Deviations from Matthiessens Rule for Dilute Alloys of Tin with Cadmium, Phys Rev B-Solid St 6(10) (1972) 3624-3633.

[90] D.K. Wagner, R. Bowers, Radio-Frequency Size Effect - Tool for Investigation of Conduction Electron-Scattering in Metals, Adv Phys 27(5) (1978) 651-746.

[91] C.Y. Ho, M.W. Ackerman, K.Y. Wu, S.G. Oh, T.N. Havill, Thermal-Conductivity of 10 Selected Binary Alloy Systems, J Phys Chem Ref Data 7(3) (1978) 959-1177.

[92] L. Nordheim, Zur elektronentheorie der metalle. i, Annalen der Physik 401(5) (1931) 607-640.

[93] T.H. Davis, J.A. Rayne, Specific-Heat and Residual Resistivity of Binary and Ternary Noble-Metal Alloys, Phys Rev B 6(8) (1972) 2931-2942.

[94] S.U. Jen, Anisotropic Magnetoresistance of Co-Pd Alloys, Phys Rev B 45(17) (1992) 9819-9823.

[95] Y.Y. Tsiovkin, A.V. Lukoyanov, A.A. Povzner, E.S. Koneva, M.A. Korotin, A.O. Shorikov, V.I. Anisimov, A.N. Voloshinskii, V.V. Dremov, Theoretical investigation of the residual electrical resistivity concentration dependence of transuranium metal alloys, Phys Rev B 80(15) (2009).

[96] Y.Y. Tsiovkin, V.V. Dremov, E.S. Koneva, A.A. Povzner, A.N. Filanovich, A.N. Petrova, Theory of the residual electrical resistivity of binary actinide alloys, Phys Solid State+ 52(1) (2010) 1-5.

[97] Y. Zhang, A.D.R. Andersson, A thermal conductivity model for U-Si compounds. NO. LA-UR-16-27736., Los Alamos National Laboratory (LANL), 2017.

[98] J.K. Fink, L. Leibowitz, Thermal-Conductivity of Zirconium, J Nucl Mater 226(1-2) (1995) 44-50.

[99] W. Chen, X.-M. Bai, Temperature and composition dependent thermal conductivity model for U-Zr alloys, J Nucl Mater 507 (2018) 360-370.

[100] X. Ding, T. Yao, L. Fu, Z. Hua, J. Harp, C. Marianetti, M. Neupane, M.E. Manley, D. Hurley, K. Gofryk, Magnetic, transport and thermal properties of δ-phase UZr2, Philosophical Magazine Letters 101(1) (2021) 1-11.

[101] Z. Hua, T. Yao, A. Khanolkar, X. Ding, K. Gofryk, L. He, M. Benson, D. Hurley, Intragranular thermal transport in U–50Zr, J Nucl Mater 534 (2020) 152145.

[102] R.I. Sheldon, D.E. Peterson, The U-Zr (Uranium-Zirconium) system, Bulletin of Alloy Phase Diagrams 10(2) (1989) 165-171.

[103] J.C. Maxwell, A treatise on electricity and magnetism, vol. I, 3rd Ed, Oxford University Press (1904).

[104] D.A.G. Bruggeman, Berechnung verschiedener physikalischer Konstanten von heterogenen Substanzen. I. Dielektrizitätskonstanten und Leitfähigkeiten der Mischkörper aus isotropen Substanzen, Annalen der Physik 416(7) (1935) 636-664.

[105] D.P.H. Hasselman, L.F. Johnson, Effective Thermal Conductivity of Composites with Interfacial Thermal Barrier Resistance, Journal of Composite Materials 21(6) (1987) 508-515.

[106] G.L. Pollack, Kapitza Resistance, Reviews of Modern Physics 41(1) (1969) 48-81.

[107] C.-W. Nan, R. Birringer, Determining the Kapitza resistance and the thermal conductivity of polycrystals: A simple model, Phys Rev B 57(14) (1998) 8264-8268.

[108] C.-W. Nan, R. Birringer, D.R. Clarke, H. Gleiter, Effective thermal conductivity of particulate composites with interfacial thermal resistance, Journal of Applied Physics 81(10) (1997) 6692-6699.

[109] B. He, B. Mortazavi, X. Zhuang, T. Rabczuk, Modeling Kapitza resistance of two-phase composite material, Composite Structures 152 (2016) 939-946.

[110] F. Badry, K. Ahmed, A new model for the effective thermal conductivity of polycrystalline solids, AIP Advances 10(10) (2020) 105021.

[111] D. Gaston, C. Newman, G. Hansen, D. Lebrun-Grandié, MOOSE: A parallel computational framework for coupled systems of nonlinear equations, Nucl Eng Des 239(10) (2009) 1768-1778.

[112] J.D. Hales, M.R. Tonks, K. Chockalingam, D.M. Perez, S.R. Novascone, B.W. Spencer, R.L. Williamson, Asymptotic expansion homogenization for multiscale nuclear fuel analysis, Computational Materials Science 99 (2015) 290-297.

[113] P.W. Chung, K.K. Tamma, R.R. Namburu, Homogenization of Temperature-Dependent Thermal Conductivity in Composite Materials, Journal of Thermophysics and Heat Transfer 15(1) (2001) 10-17.

[114] Y.S. Song, J.R. Youn, Evaluation of effective thermal conductivity for carbon nanotube/polymer composites using control volume finite element method, Carbon 44(4) (2006) 710-717.

[115] K. Bakker, Using the finite element method to compute the influence of complex porosity and inclusion structures on the thermal and electrical conductivity, International Journal of Heat and Mass Transfer 40(15) (1997) 3503-3511.

[116] M.C. Teague, B.S. Fromm, M.R. Tonks, D.P. Field, Using Coupled Mesoscale Experiments and Simulations to Investigate High Burn-Up Oxide Fuel Thermal Conductivity, JOM 66(12) (2014) 2569-2577.

[117] A. Khater, J. Szeftel, Theory of the Kapitza resistance, Phys Rev B 35(13) (1987) 6749-6755.

[118] H. Haug, K. Weiss, A modified theory of the Kapitza resistance, Physics Letters A 40(1) (1972) 19-21.

[119] A.C. Anderson, W.L. Johnson, The Kapitza resistance between copper and3He, Journal of Low Temperature Physics 7(1) (1972) 1-21.

[120] J.-L. Barrat, F. Chiaruttini, Kapitza resistance at the liquid—solid interface, Molecular Physics 101(11) (2003) 1605-1610.

[121] Z. Ren, J. Wu, R. Ma, G. Hu, C. Luo, Thermodynamic properties of α-uranium, J Nucl Mater 480 (2016) 80-87.

[122] M.A. Blanco, E. Francisco, V. Luaña, GIBBS: isothermal-isobaric thermodynamics of solids from energy curves using a quasi-harmonic Debye model, Computer Physics Communications 158(1) (2004) 57-72.

[123] F. Badry, R. Brito, M.G. Abdoelatef, S. McDeavitt, K. Ahmed, An Experimentally Validated Mesoscale Model of Thermal Conductivity of a UO2 and BeO Composite Nuclear Fuel, JOM 71(12) (2019) 4829-4838.